UNIVERSITY OF MALAYA

ORIGINAL LITERARY WORK DECLARATION

Name of Candidate: CHEW CHEE SEAN **I.C No:** 840612-02-5332

Registration/Matric No: KGA 080081

Name of Degree: Master of Engineering Science

Title of Dissertation ("this Work"):

Performance of Ni-W Alloys as Barrier Film between Lead Free Solder and Copper Substrate

Field of Study: Electronic packaging materials

I do solemnly and sincerely declare that:

(1) I am the sole author/writer of this Work;
(2) This Work is original;
(3) Any use of any work in which copyright exists was done by way of fair dealing and for permitted purposes and any excerpt or extract from, or reference to or reproduction of any copyright work has been disclosed expressly and sufficiently and the title of the Work and its authorship have been acknowledged in this Work;
(4) I do not have any actual knowledge nor do I ought reasonably to know that the making of this work constitutes an infringement of any copyright work;
(5) I hereby assign all and every rights in the copyright to this Work to the University of Malaya ("UM"), who henceforth shall be owner of the copyright in this Work and that any reproduction or use in any form or by any means whatsoever is prohibited without the written consent of UM having been first had and obtained;
(6) I am fully aware that if in the course of making this Work I have infringed any copyright whether intentionally or otherwise, I may be subject to legal action or any other action as may be determined by UM.

Candidate's Signature: **Date:**

Subscribed and solemnly declared before,

Witness's Signature: **Date:**

Name:

Designation:

ABSTRACT

Due to environmental concerns, the electronics industry is actively shifting from lead solders to lead free solders. Sn based lead free solders are the most suitable 49is used in the under bump metallurgy (UBM) and substrate metallization for flip chip and ball grid array (BGA) applications. Interactions and interdiffusion between Sn based lead free solders and copper substrate result weak interface and serious reliability problems in electronic device. In order to limit the outward diffusion of copper atoms, a thin barrier layer has been used between lead free solder and copper substrate.

In this study, interfacial reactions between Sn-3.5Ag (SA) and Sn-3.8Ag-0.7Cu (SAC) lead free solders and Ni-W alloy films were investigated. Ni-W alloy films with tungsten contents in the range of 5.0-18.0 at.% were prepared on copper substrate by electrodeposition in ammonia-citrate bath. Solder joints were prepared on the Ni-W coated substrate at a reflow temperature of $250^{o}C$. Multiple reflow and high temperature storage were performed on a number of samples. Spreading rate and wetting angle of solders were measured. The microstructures of the solder joints interface were investigated by field emission scanning electron microscopy. Chemical compositions of the intermetallic compounds (IMC) were analyzed by energy dispersive X-ray spectroscopy. Mechanical properties of the IMC formed were performed by nanoindentation.

It was found that a Ni_3Sn_4 layer with faceted morphology formed between SA and the Ni-W alloy films after reflow. A ternary Sn-Ni-W was observed below the Ni_3Sn_4 layer. In contrast, a non-uniform $(Cu,Ni)_6Sn_5$ layer formed at interface between SAC and Ni-W alloy films. A quaternary Sn-Cu-Ni-W was found below the $(Cu,Ni)_6Sn_5$

layer. The thickness of both Ni_3Sn_4 and $(Cu,Ni)_6Sn_5$ layers were found to decrease with the increase of tungsten contents in the Ni-W film. The ternary Sn-Ni-W and quaternary Sn-Cu-Ni-W layers were found to be amorphous and are suggested to have formed through solid state amorphization caused by anomalously fast diffusion of Sn into Ni-W film.

The hardness of each phase obtained by nanoindentation testing decreases in the following order: $(Cu,Ni)_6Sn_5$ phase > Ni_3Sn_4 phase > Sn-Ni-W ternary phase > Ni-18 at.% W > copper substrate > SAC solder > SA solder. The lower hardness and soft Sn-Ni-W phase is significantly related to the amorphous structure.

ABSTRAK

Pada masa kini, industri elektronik telah bertukar dari pateri berplumbum kepada pateri tanpa plumbum demi prihatian kepada alam sekitar. Pateri tanpa plumbum yang berasas daripada stanium merupakan bahan yang paling sesuai untuk menggantikan pateri berplumbum. Pada bidang pembungkusan mikroelektronik, kuprum digunakan pada metalurgi bawah bonggol (UBM) dan substrat perlogaman untuk cip flip dan susunan bola grid (BGA) aplikasi. Interaksi dan peresapan dalaman antara pateri tanpa plumbum yang berasas daripada stanium dan substrat kuprum mengakibatkan antara muka yang lemak.dan masalah seliabiliti yang serius dalam peranti elektronik. Untuk menghadkan peresapan atom-atom kuprum, satu lapisan halangan yang nipis telah digunakan di antara pateri tanpa plumbum dan substrat kuprum.

Dalam penyelidikan ini, interaksi lapisan antara muka di antara Sn-3.5Ag (SA), pateri tanpa plumbum Sn-3.8Ag-0.7Cu (SAC) dan aloi Ni-W disiasat. Lapisan aloi Ni-W dengan kandungan tungsten dalam linkungan 5.0-18.0 at.% disediakan pada subtrat kuprum melalui elektrodeposisi dalam larutan amonia sitrat. Penyambungan pateri disediakan pada substrat yang dibalut dengan Ni-W dalam suhu reflow pada 250°C. Pelbagai reflow dan simpanan pada suhu tinggi dilakukan pada sampel-sampel yang tertentu. Kadar penyebaran dan sudut basah dikira. Struktur mikro di antara muka penyambungan pateri diselidik dengan menggunakan gelanggang pembebasan imbasan mikroskop elektron (FESEM). Komposisi kimia sebatian imtermetalik (IMC) dianalisis dengan menggunakan spektroskopi tenaga dispersi sinar-X (EDX). Analisis sifat mekanik IMC yang terbentuk dilakukan dengan menggunakan nanoindentation.

Didapati bahawa lapisan Ni_3Sn_4 dengan morfologi tersegi terbentuk di antara SA dan lapisan aloi Ni-W selepas reflow. Si-Ni-W pertiga diperhatikan di bawah lapisan Ni_3Sn_4. Di sebaliknya, lapisan $(Cu,Ni)_6Sn_5$ tidak seragam terbentuk pada muka antara SAC dan lapisan aloi Ni-W. Sn-Cu-Ni-W perempat didapati di bawah lapisan $(Cu,Ni)_6Sn_5$. Ketebalan lapisan-lapisan Ni_3Sn_4 dan $(Cu,Ni)_6Sn_5$ mengurang dengan peningkatan kandungan tungsten dalam filem Ni-W. Lapisan-lapisan Sn-Ni-W pertiga dan Sn-Cu-Ni-W perempat adalah dalam bentuk amorfus dan dijangka bahawa mereka terbentuk melalui pengamorfusan bentuk pejal disebabkan oleh Sn yang berdifusi pantas ke dalam filem Ni-W.

Kekerasan pada fasa tertentu yang diperolehi daripada kajian nanoindentation menurun dalam urutan seperti berikut: fasa $(Cu,Ni)_6Sn_5$ > fasa Ni_3Sn_4 > fasa pertiga Sn-Ni-W > Ni-18 at.% W > substrat kuprum > pateri SAC > pateri SA. Kekerasan yang rendah dan fasa Sn-Ni-W yang lembut adalah berkait dengan struktur amorfus.

ACKNOWLEDGEMENTS

First and foremost, I would like to express my sincere thanks to my supervisor of this project, Prof. A.S.M.A. Haseeb, and co-supervisor, Dr. Mohd Rafie Johan, for their valuable guidance and advice. They inspired me greatly to work in this project and willingness to motivate me contributed tremendously to this project. I am very indebted to the help throughout this study.

This research would not be successfully completed without the financial support from University of Malaya with project no. (RG 068/09AET) and Institute of Research Management and Consultancy (IPPP) with project no (PS070/2008C and PS354-2009B) for providing us with a good environment and facilities to complete this project.

Special thanks to Mr Mohd. Nazarul Zaman for FESEM, FIB and EBSD analyses and his efforts and patience during the measurements are appreciated.

Finally, grateful acknowledgement is extended to my lovely family members and my friends, especially Ms Ng Meng Nee, Ms Tay See Leng, Ms Ang Bee Chin, Ms Aemi Nadia and Mr Arafat for their supports and encouragements throughout the process. Their understanding and willingness to help have significantly improved my efficiency in this particular project. I am deeply and sincerely appreciated.

TABLE OF CONTENTS

LIST OF FIGURES

LIST OF TABLES

LIST OF SYMBOLS AND ABBREVIATIONS

θ	Angle
BSE	Back scatter electron
EDX	Energy Dispersive X-ray Spectroscopy
FESEM	Field Emission Scanning Electron Microscopy
EBSD	Electron Back Scatter Diffraction
FIB	Focus Ion Beam
EPMA	Electron Probe Microanalysis
WDS	Wavelength Dispersive Spectroscopy
AFM	Atomic Force Microscopy
TEM	Transmission Electron Microscopy
DMT	Derjaguin-Muller-Toporov
kV	Kilovolt
IMC	Intermetallic Compounds
PCB	Printed Circuit Board
UBM	Under Bump Metallization
BGA	Ball Grid Array
SA	Sn-3.5Ag
SAC	Sn-3.8Ag-0.7Cu
S_R	Spreading Rate
D	Diameter of the solder used
H	Height of spread solder
V	Volume
H	Hardness
E	Reduced Elastic Modulus

CHAPTER 1: INTRODUCTION

1.1 Background of study

Interactions and interdiffusion between solder and substrate is of vital importance in assuring the reliability of solder joints in electronic products. Morphology, growth behavior and properties of intermetallic compounds (IMC) formed at the interface between solder and substrate play a crucial role in this regard. Due to environmental concerns, the electronics industry is actively shifting from lead solders to lead free solders. Sn based lead free solders are the most suitable materials for the replacement of lead solders.

In the microelectronics packaging, copper is widely used in the under bump metallurgy (UBM) and substrate metallization for flip chip and ball grid array (BGA) applications (Sharif *et al.*, 2004a). However, copper can easily form Cu_3Sn and Cu_6Sn_5 IMC with Sn based solders during soldering. These IMC are considered detrimental to solder joint reliability due to the brittle nature of the IMC. In order to limit the outward diffusion of copper atoms, a thin nickel film layer has been used as a barrier film between lead free solder and copper substrate. The main characteristic of the barrier film is to serve as a diffusion barrier between lead free solder and copper substrate. In some cases, nickel film failed its mission to hinder the diffusion of copper (Alam, 2002).

Researchers are therefore putting much efforts in improving the stability of nickel based barrier films by adding alloying elements (Mannan *et al.*, 2005; Liang *et al.*, 2006; Chen *et al.*, 2007b; Yoon *et al.*, 2008; Yoon *et al.*, 2010). Alloying elements that have been currently under investigation in nickel based barrier films can be divided into two groups (i) metalloids, like P, B, and (ii) refractory metals like W, V and Nb.

In this study, interfacial reactions between Sn-3.5Ag (SA) and Sn-3.8Ag-0.7Cu (SAC) lead free solders and Ni-W alloy films were investigated. SA and SAC were selected as interconnection materials due to its low melting temperature and good wetting behaviour (Huang, 2005; Babaghorbani, 2008). Meanwhile, Ni-W alloy are known to possess a good thermal stability and exhibit lower diffusion rate (Haseeb, 2008a; Haseeb, 2008b). The binary phase diagram revealed relativity low solubility of W in liquid Sn and Cu. Hence, it is expected that presence of W would affect the interfacial reaction. The aim of this work is therefore to investigate the effect of tungsten on the performance of barrier film after SA and SAC soldering, respectively.

1.2 Research objectives

The objectives of this study are as follows:

- To optimize the electroplate conditions and thickness of nanocrystalline Ni-W alloy films on copper substrate
- To study the wetting characteristics of Ni-W alloy films between lead free solders
- To study the intermediate compounds (IMC) that form between Ni-W and lead free solders
- To study the effect of W content on the interfacial intermetallic layer formation
- To perform nanomechanical test to assess mechanical properties of IMC between lead free solders and Ni-W alloy films

1.3 Scope of study

Coating preparation

In order to understand the effects of tungsten at lead free solders interface, Ni-W alloy films with different tungsten content were prepared on copper substrate by electrodeposition from an ammonia-citrate bath. A series of samples were deposited with a range of deposition time. A thickness about 2.5 μm was aimed in this study.

Solder preparation, reflow and aging

After the coating, a solder paste, which is either Sn-3.5Ag (SA) or Sn-3.8Ag-0.7Cu (SAC) was placed on electrodeposited substrates by using a jig with 6.5mm opening. The samples were reflowed on a reflow oven at 250^{o}C. After first reflow, some samples were subjected to multiple reflow and high temperature storage (HTS) at 150 ^{o}C. These are the methods to accelerate the IMC growth at the interface (Zeng, 2002; Wong *et al.*, 2010b).

After cooling, the residual flux was removed by acetone and the height of solder was calculated for spreading rate, cross section samples were prepared by standard metallographic methods to examine the microstructure of the solder and the formation of IMC at the interface. The wetting angle was measured using optical light microscope.

The micrographs were examined by backscattered electron detector under a field emission scanning electron microscope (FE-SEM). The elemental analysis was carried out by energy dispersive X-ray spectroscopy (EDX). Electron back scatter diffraction (EBSD) analysis was used to identify the channeling pattern of the phase. Focus Ion Beam (FIB) was employed by milling across the interface for getting better contrast images. Electron probe microanalysis (EPMA) with wavelength dispersive spectroscopy

(WDS) was used for elemental mapping. The topographies were characterized using atomic force microscope (AFM). Mechanical properties of the intermetallic compounds (IMC) formed between lead free solders and Ni-W alloy film were performed by nanoindenter (Micro Material).

CHAPTER 2: LITERATURE STUDY

2.1 Replacement of lead solder to lead free solder alloy in electronic assemblies

In modern flip chip microelectronic assemblies, miniature high-performance with multifunction gate logic chips are placed closer to each other. Solders are widely used as interconnection of the chips and Printed Circuit Board (PCB) surface finishes in the assembly. Figure 2.1 shows the cross section of a flip chip interconnection, where the solder is placed between a die/chip and a substrate. Soldering provides electrical, thermal and mechanical continuity between the chip and the substrate; therefore, it is vital to the overall functioning of the assembly.

In recent year, the electronic packaging industries have been putting lots of efforts in replacing lead solders to lead free solders. Because the usage of lead has shown negative impact on the human body and the environment, many countries have banned the use of lead solder (Zeng, 2002). Lau *et al.* (2003) stated the negative impact of lead based solder and its compounds which can affect the health of children and damage the nervous, endocrine and cardiovascular systems. In the electronic industry, the disposal of electronic products that contained lead is a common environmental pollutant. The toxicity of lead has been found in soil, plant, and water. This is directly threatening our routine of each day. Therefore, developing of lead free solder is crucial in electronic assemblies.

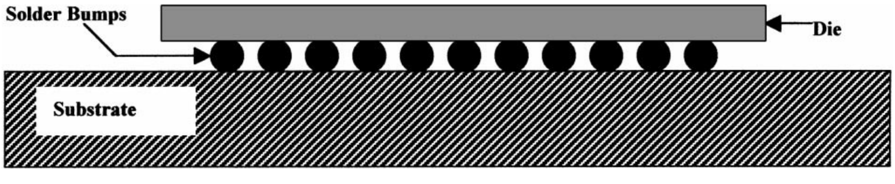

Figure 2.1: Cross section of a flip chip interconnection (Abtew, 2000).

In conjunction to replace lead solder, Sn based solders have received the most attention. Tin fulfils several requirements such as good metallurgical, environment friendly, low material cost, and acceptable melting temperature (Alam, 2002; Islam *et al.*, 2005). Researchers have been investigating on binary and ternary tin based alloys over the past few years, which included Sn-Ag, Sn-Cu, Sn-Zn, Sn-In, Sn-Sb, Sn-Ag-Cu, Sn-Ag-Bi, Sn-Zn-In, and Sn-Zn-Al (Islam *et al.*, 2005; Sun *et al.*, 2006; Sun *et al.*, 2007).

2.2 Sn-3.5Ag (SA) and Sn-3.8Ag-0.7Cu (SAC) solders

Among the Sn based solders have been developing, Sn-3.5Ag (SA) and Sn-3.8Ag-0.7Cu (SAC) solders were common used in studies. SA solder alloy was used because of its good wettability, higher strength and superior resistance to creep and thermal fatigue (Babaghorbani, 2008).

The phase diagram of SA is shown in Figure 2.2. It can be seen that there is negligible solid solubility of Ag in solid Sn. The liquidus temperature decreases from 232°C of pure Sn to 221°C at SA. However, the melting temperature of SA is considered higher than Sn-Pb solder which is 183 ^{o}C (Huang, 2005).

In order to decrease the melting temperatures of Sn-Ag based lead free solders, minor additions of Cu were added. The melting temperature of Sn-3.8Ag-0.7Cu (SAC) is 217 ^{o}C (Huang, 2005). This is in agreement with the measured ternary eutectic temperature in the Sn-Ag-Cu system of 217°C, as seen in Figure 2.3. In 2000, the National Electronics Manufacturing Initiative (NEMI) advised to replace the eutectic Sn-Pb alloy with the eutectic Sn-Ag-Cu alloy (Sun *et al.*, 2006). The eutectic alloy of tin and noble metals: Ag and Cu are used as the Sn-Ag-Cu solder because it has a single and low melting point, better creep-fatigue resistance and microstructural stability (Zeng, 2002; Erinc *et al.*, 2007).

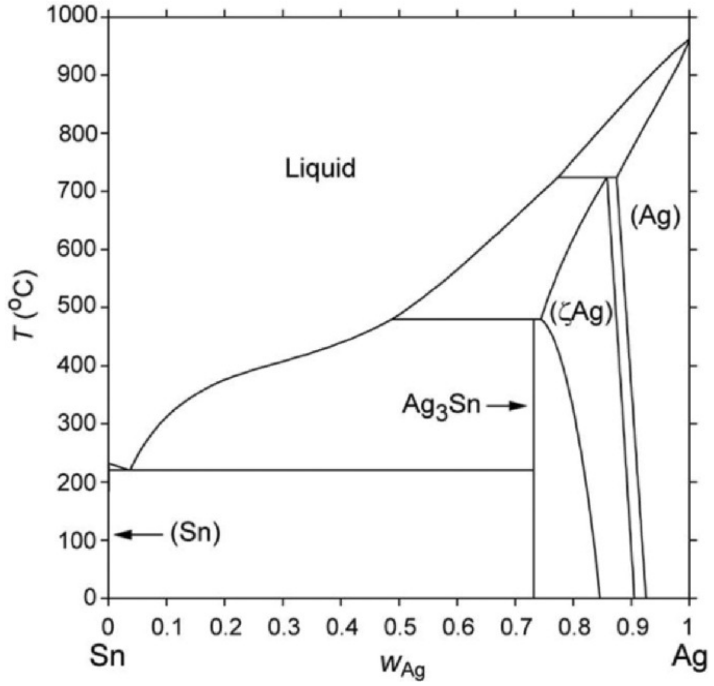

Figure 2.2: Sn-Ag phase diagram (Handwerker *et al.*, 2007).

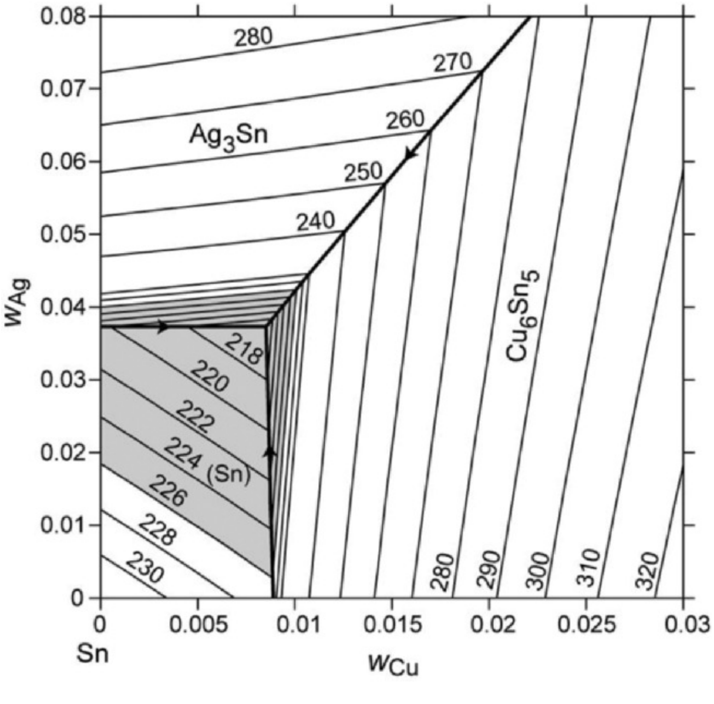

Figure 2.3: Sn-Ag-Cu phase diagram-liquidus projection (Handwerker *et al.*, 2007).

2.3 Reaction between lead free solder and copper substrate

In the microelectronics packaging, copper is widely used in the under bump metallurgy (UBM) and substrate metallization for flip chip and ball grid array (BGA) applications (Sharif *et al.*, 2004a). A typical reliability problem encountered when tin in lead free solder comes in contact with copper metallization. Because copper can easily form Cu_3Sn and Cu_6Sn_5 intermetallic compounds (IMC) with tin in lead free solder during soldering. The thickness of both Cu_3Sn and Cu_6Sn_5 layers increased linearly during thermal aging (Alam, 2002). From the Sn-Cu binary phase diagram in Figure 2.4, it can be seen that two stable Cu_3Sn and Cu_6Sn_5 intermetallic compounds are formed between Sn and Cu reactions.

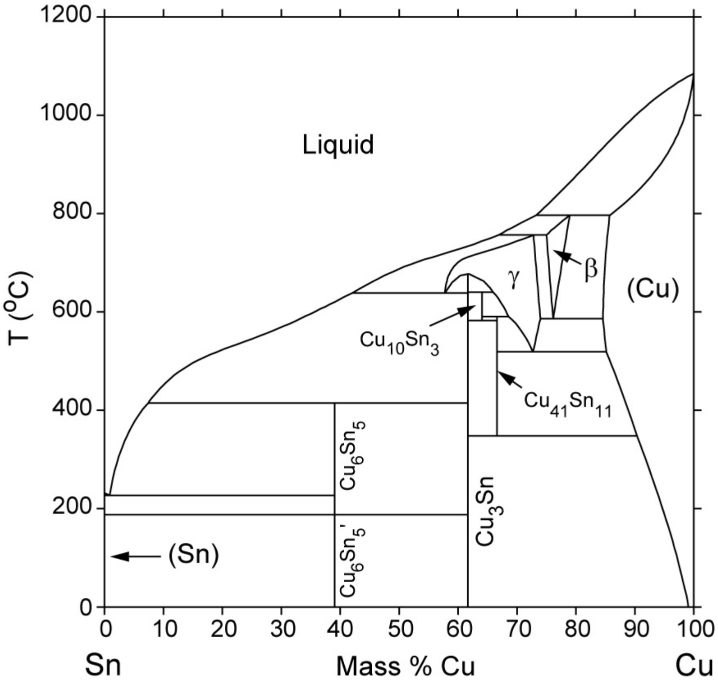

Figure 2.4: Sn-Cu binary phase diagram (Shim *et al.*, 1996).

The growth of these IMC can directly influence the reliability of solder joints due to the brittle nature of the compounds. Further reductions in solder bumps size aggravate the reliability concern. In order to overcome the problems, a good number of studies have been reported on the use of a barrier film on Cu substrate during reflow such as Ni film (He *et al.*, 2004; Sharif *et al.*, 2004b; Chang *et al.*, 2007), Ni-P (Anhock *et al.*, 1996; Yoon *et al.*, 2008, Sohn *et al.*, 2004; Sun *et al.*, 2006; Vuorinen *et al.*, 2006), Ni-B (Choi *et al.*, 2006; Yoon *et al.*, 2008; Yoon *et al.*, 2010), Ni-V (Chen, 2006a; Chen *et al.*, 2006b; Chen, 2007a; Chen *et al.*, 2007b; Wang *et al.*, 2010b), Co-P film (Magagnin *et al.*, 2005; Liang *et al.*, 2006), Co-W-P (Wu *et al.*, 2008).

2.4 Barrier film

In order to limit the outward diffusion of copper atoms, a thin barrier layer has been used between lead free solder and copper substrate. The main characteristic of the barrier film is served as a diffusion barrier for flip-chip soldering. According to Wu *et al.* (2008), the diffusion barrier is classifiable as a sacrificial barrier, a stuffed barrier, a passive-compound barrier or an amorphous barrier. The most common material used in UBM as a diffusion barrier is Ni film. There are mainly two types of processes to form the Ni diffusion barrier on top of the copper substrate, which are a wet process and a dry process. First of all, in the wet processes include electroplating and electroless deposition of Ni film. In the dry processes, physical vapor deposition (PVD) or chemical vapor decomposition (CVD) is used (Choi *et al.*, 2006).

In electroplating of Ni film, a power supply is connected to the circuit and electrodes are immersed in the electrolyte. Therefore, thickness of the film can be well controlled during deposition process. Electroplating is a good process for a small to large scale plating (Jang *et al.*, 2003). According to Sharif *et al.* (2004b), the electrolytic Ni layer on Cu substrate created good solderable surface and acted as a good barrier film.

Besides, electroless Ni deposit offers an excellent solderability, uniform thickness, low processing temperature, low cost, corrosion resistance and selective deposition (Alam, 2002). In general, the electroless Ni coatings are grouped as Ni, Ni-P, and Ni-B that based on the reducing agents (hydrazine, hypophosphite, and boronhydride, respectively) as the reducing agent (Liang *et al.*, 2006; Yoon *et al.*, 2010).

In dry process, Ni is formed by a sputtering process. A 7wt.% V is usually added into the nickel to facilitate the nickel sputtering process to overcome Ni ferromagnetism (Chen, 2006a). A dry process of Ni plating is in fact a Ni-V alloy film.

2.5 Interfacial reaction at Ni film

In order to limit the outward diffusion of copper atoms, a thin nickel film layer has been used as a barrier film between lead free solder and copper substrate. Nickel is known to possess relatively low reaction rates with most solders (Wang, 2006).

The morphologies and the growth kinetics of the thin IMC layer in tin based solders on nickel film have been investigated by researchers. From most of the reports, Ni_3Sn_4 is the only phase that found at Sn or Sn-Ag solder interface (Sharif *et al.*, 2004b; Sharif, 2005; Shen *et al.*, 2009). This is in agreement to the Ni_3Sn_4 IMC that found at Sn-Ag-Ni ternary phase diagram in Figure 2.5. According to Dybkov (2008), small grain and thin Ni_3Sn_4 layer formed between Sn based solder and Ni film. Initially, the solder is in the molten state for about 45 s and Ni_3Sn_4 IMC formed under conditions with their simultaneous dissolution of Ni solid metal in the molten solder. The thinnest Ni_3Sn_4 is due to the dissolution of Ni solid metal in the liquid phase.

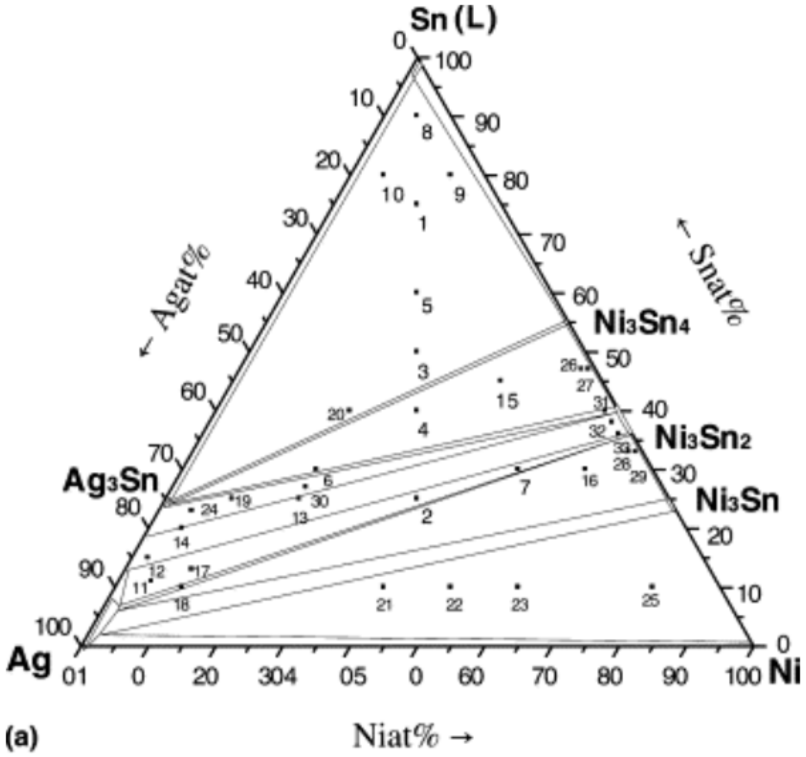

Figure 2.5: The Ag-Sn-Ni ternary system at 240^{o}C (Hsu, 2004).

In contrast, a ternary IMC, which consist of Cu, Ni and Sn are observed between Ni layer and Sn-Ag-Cu solders. The Cu concentration in the Sn-Ag-Cu solder has a very strong influent on the formation of intermetallic compounds. When copper is added to a Sn-Ag solder that lower than 0.2 wt.%, only $(Ni,Cu)_3Sn_4$ is found at the interface. At higher Cu concentration which more than 0.6 wt.%, $(Cu,Ni)_6Sn_5$ is found to have formed at Ni-alloy based substrate (Sun *et al.*, 2006). According to the diffusion path A in Figure 2.6 that superimposed with the Sn-Cu-Ni ternary phase diagram, pure Ni cannot exist in local equilibrium with $(Cu,Ni)_6Sn_{5;}$ additional layer must form between them during isothermal aging which is $(Ni,Cu)_3Sn_4$.

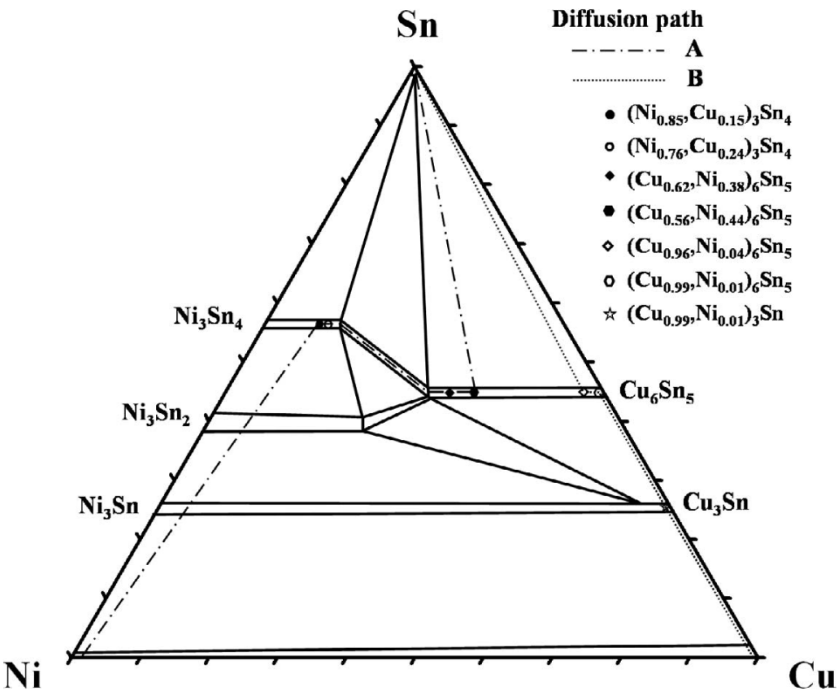

Figure 2.6: Reaction paths of (Sn,Cu/Ni) couples reacted at 240°C superimposed on the Sn-Cu-Ni isothermal section (Yao *et al.*, 2009).

2.6 Effect of alloying elements in Ni film

Alloying elements that have been currently under investigation in nickel based barrier films can be divided into two groups (i) metalloids, like P, B, and (ii) refractory metals like W, V and Nb. When metalloids like P, B are added to nickel in sufficient amount, the resulting nickel alloy becomes amorphous. When the P content is less than 5.5 wt.%, it is known as nanocrystalline; while more than 9 wt.% P in Ni-P film is became amorphous structure (Alam, 2003). The Ni-P films with 5.5–8.5 wt.% P are known to be a mixture of small crystallites and an amorphous phase (Sohn *et al.*, 2004; Yoon *et al.*, 2010). In contrast, the crystallinity decreases as increasing of B content on its film (Yoon *et al.*, 2008). It has been reported that the microstructure of Ni-P and Ni-B layer change significantly with P and B content on the films, respectively.

2.6.1 Interfacial reaction between Sn based solder and Ni-P film

During soldering, such a phosphorous containing amorphous film undergoes what has been termed as ‘solder induced crystallization’. During this event, a thin Ni_3P layer forms between the amorphous Ni-P layer and the Ni-Sn based IMC, Ni_3Sn_4 that forms during reflow. Ni_3P layer has been found to be brittle and hence can affect the solder joint reliability (Lee *et al.*, 2003; Sharif, 2005).

It has been reported that reliability degradation occurs at the interface between Ni-P layer and lead free when Ni_3P layer is formed on the interface during soldering which caused by P accumulation (Lee *et al.*, 2003; Vuorinen *et al.*, 2006). According to Kumar (2005), Ni-P layer failed to protect the Cu substrate after forty reflow cycles 200^{o}C. After 40 reflow cycles, a complete conversion of Ni-P into Cu_6Sn_5 phase was found which is shown in Figure 2.7.

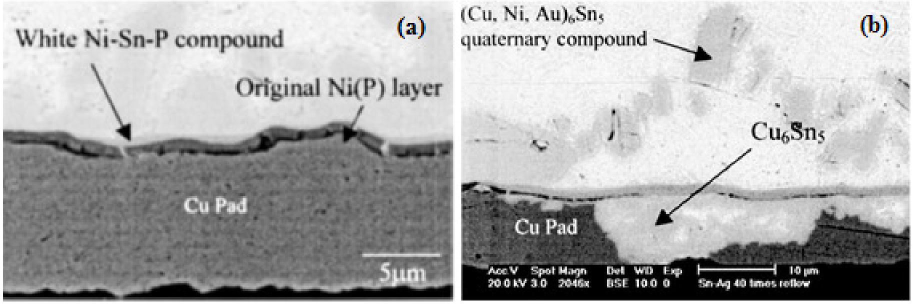

Figure 2.7: SEM micrographs showing the interface between SA and Ni-P after (a) twenty and (b) forty reflow cycles (Kumar, 2005).

Figure 2.8 shows the cross-sectional SEM images of SA/Ni-7 wt.% P and SA/Ni-10 wt.% P after aging at 150 ^{o}C for 28 days. A Ni_3Sn_4 layer formed between solder and Ni-P. The out diffusion of Ni atoms to form the Ni_3Sn_4 layer resulted in a P-rich layer, which is Ni_3P. This transformation is termed as “solder reaction-assisted crystallization’ (Yoon *et al.*, 2010). Besides, a white layer (Ni-Sn-P) is observed to have formed between Ni_3Sn_4 and Ni_3P. The thickness of Ni_3Sn_4 layer is seen to decrease at Ni-10 wt.% P film. The amount of P in the barrier film has been found to have an influence on the thickness of Ni_3Sn_4. An increase in the amount of P has been found to decrease the thickness of Ni_3Sn_4 (Yoon *et al.*, 2010).

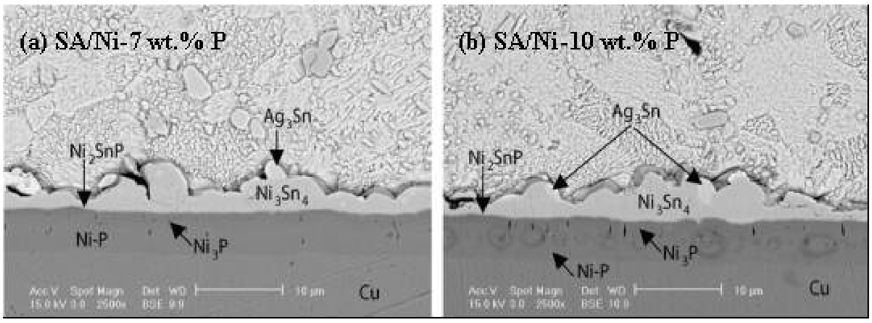

Figure 2.8: SEM images of (a) SA/Ni-7 wt.% P and (b) SA/Ni-10 wt.% P after aging at 150°C for 28 days (Yoon *et al.*, 2010).

When Sn-Ag-Cu solder was used at Ni-P interface, $(Cu,Ni)_6Sn_5$ layer was found after reflow process (Sharif *et al.*, 2004b; Vuorinen *et al.*, 2006). It is found that a thin ternary layer (Ni-Sn-P) forms between $(Cu,Ni)_6Sn_5$ layer and Ni-P film. This is similar the case at SA interface. Bright field TEM indicated that the thin ternary layer is nanocrystalline structure. However, this ternary layer consists numerous small ‘pores’ and might affect the reliability of the solder joint.

2.6.2 Interfacial Reaction between Sn based and Ni-B Film

Electroless Ni-B deposits have also received considerable attention in recent years due to its ability to act as a diffusion barrier layer to prevent the diffusion of Cu. The Ni-B coating possesses good solderability compared to the Ni-P coating because its oxide layer is thin and thus can be penetrated by the solder (Yoon *et al.*, 2008; Yoon *et al.*, 2010).

According to the reports (Yoon *et al.*, 2008; Yoon *et al.*, 2010), the XRD pattern of the Ni–1 wt.%B sample exhibited a crystalline phase, whereas that of Ni–3 wt.% B exhibited an amorphous phase. Yoon *et al.* (2008) suggested that the crystallinity decreased with increasing of B content in the Ni-B plating layer.

Amorphous films do not have any grain boundary and hence may exhibit a good barrier film (Yoon *et al.*, 2008). At SA and Ni-1 wt.% B interface, a thick Ni_3Sn_4 layer was observed (Yoon *et al.*, 2010). The Ni_3Sn_4 layer decreased in thickness with increasing of B content (Figure 2.9). In addition, a B-rich Ni (Ni_3B) layer is observed at the interface between the Ni_3Sn_4 IMC and Ni-B plating layer as by-products of the Ni-Sn reaction. According to Yoon *et al.* (2010), electroless Ni-P layer exhibited much slower IMC growth rate during aging at 150 ^oC compared to electroless Ni-B. The results demonstrated that the SA/Ni-P joint is more reliable than the SA/Ni-B joint from the viewpoints of interfacial IMC thickness and long-term mechanical reliability.

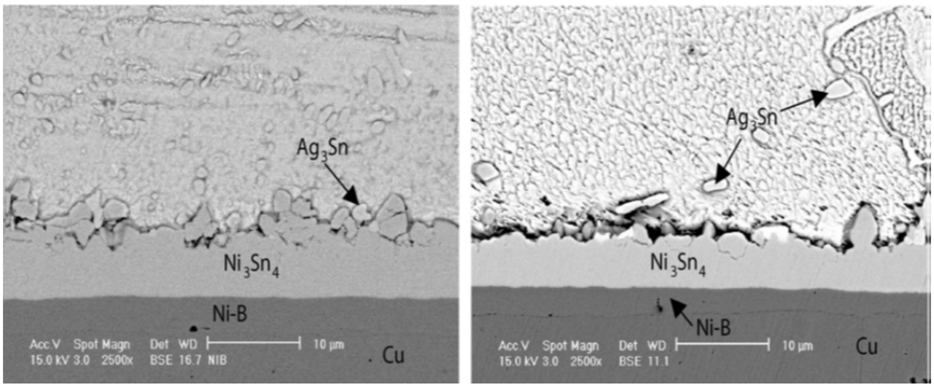

Figure 2.9: SEM images of SA/Ni-1 wt.% B and SA/Ni-3 wt.% B after aging at 150°C for 28 days (Yoon *et al.*, 2010).

2.6.3 Interfacial Reaction between Sn based and Ni-V Film

In the industrial application, nickel film is usually formed by a sputtering process. Since, nickel is known as ferromagnetic material. About 7 wt.% V is normally added into nickel target to eliminate ferromagnetism of Ni in order to facilitate the nickel sputtering process (Chen, 2006a). At the interface between SA and Ni-V, Ni_3Sn_4 IMC was formed (Chen *et al.*, 2007b). It is interesting to note that a ternary phase containing Ni, V and Sn is found to form between Ni_3Sn_4 and Ni-V film. The ternary phase (Sn-Ni-V) which appeared in bright layer is found to amorphous structure and is termed as 'T' phase (Chen, 2006a; Chen *et al.*, 2007b). Solid state amorphization reaction occurs during the reaction between Sn and Ni-7 wt.% V at 200 °C for 48 hours and shown in Figure 2.10. The TEM diffraction results indicated that 'T' phase is amorphous structure and Ni_3Sn_4 is crystalline phase. The amorphous 'T' phase lies in between Ni-V and Ni_3Sn_4 interface. The amorphous phase is a result of fast diffusion of Sn into the Ni-7 wt.% V substrate and V atoms are relatively immobile. The out diffusion of Ni atoms form the Ni_3Sn_4 phase with Sn atoms and leave the 'T' phase in more vanadium rich than Ni-7 wt.% V.

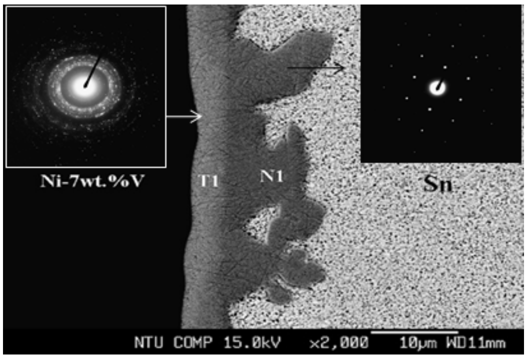

Figure 2.10: Back scattered electron micrograph of the Sn/Ni–7 wt.%V couple reacted at 200 ^{o}C for 48 h. TEM electron diffraction pattern of (T1)‘T’ and N1(Ni_3Sn_4) (Chen *et al.*, 2007b).

The vanadium content of the (Ni,V) substrates examined in the study (Chen *et al.*, 2006b) are 3 wt.%, 5 wt.%, 7 wt.%, and 12 wt.% (Figure 2.11). The samples were subjected to heating at 250^{o}C after 12 hours The interfacial reaction at Ni-3 wt.% V is different when the vanadium content are 5 wt.% and higher. The interface between SA and Ni-3 wt.% V is similar to those in the Sn/Ni couple and the phase formed is the Ni_3Sn_4 phase with a 3.8 at.% V solubility. Two phases are observed at the interface between SA and Ni-V when V content are more than 5 wt.%.

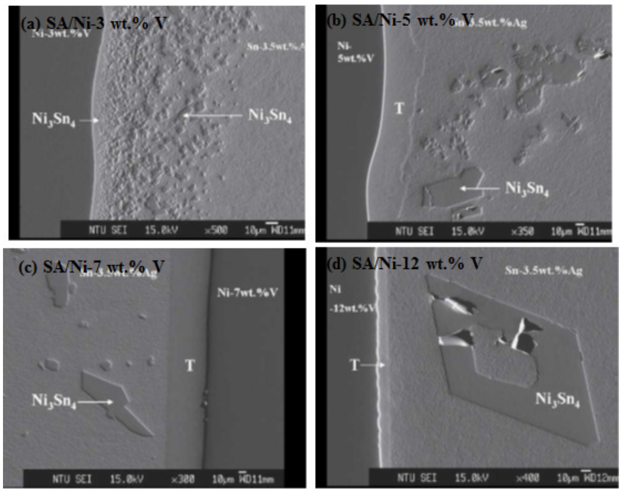

Figure 2.11: Back scattered electron micrograph at interface between SA and Ni-V films with different V content: (a) Ni-3 wt.% V, (b) Ni-5 wt.% V, (c) Ni-7 wt.% V and (d) Ni-12 wt.% V (Chen *et al.*, 2006b).

In contrast, a $(Cu,Ni)_6Sn_5$ layer is found at the interface between Sn-0.7 wt.% Cu and Ni-7 wt.% V substrate. Besides, a quaternary phase that contained of Sn, Cu, Ni and V is formed between $(Cu,Ni)_6Sn_5$ layer and Ni-7 wt.% V, as shown in Figure 2.12. The quaternary phase is termed as ‘Q’ phase (Chen, 2007a). The ‘Q’ phase is believed to have formed through solid state amorphization caused by anomalously fast diffusion of Sn and Cu into Ni-V film. The different between ‘Q’ phase and ‘T’ phase are found in quaternary and ternary system, respectively. But they may be related to solid state amorphization process.

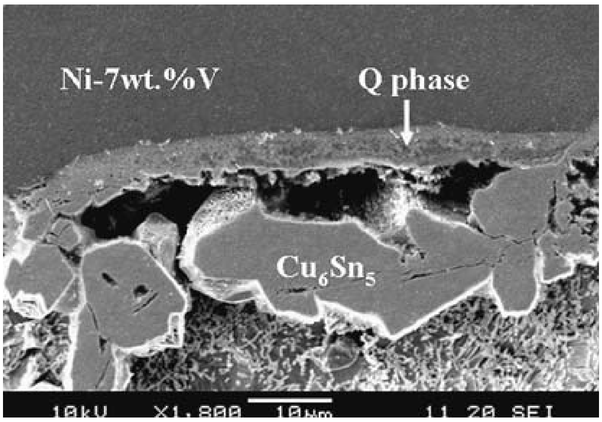

Figure 2.12: Back scattered electron micrograph of Sn-0.7 wt.% Cu /Ni–7 wt.% V couple reacted at 250 °C for 5 min (Chen, 2007a).

2.7 Solid State Amorphization

Solid state amorphization in thin film systems has been studied by many researchers (Schward, 1983; Benedictus *et al.*, 1999; Lai, 1999). This solid state amorphization is of the technological interest because of its potential to produce amorphous coating which useful as diffusion barrier (Benedictus *et al.*, 1999). It is generally believed that an amorphous film can be effective barrier as it exhibit low diffusivity.

It has been suggested that solid state amorphization between two components in thin film configuration can take place when the following conditions are satisfied: (i) the two components possess a large negative heat of mixing in the amorphous state, (ii) one component has anomalously high diffusion coefficient compared with the other, and (iii) reaction occurs at a temperature low enough to suppress the nucleation/growth of thermodynamically preferred crystalline phases.

As discussed earlier in the case at interface SA and Ni-V film, the ‘T’ phase was observed by Chen *et al.* (2006b) under TEM had an amorphous structure. The thickness of the T phase increased with the increase of reaction time. ‘T’ phase which contains of Sn, Ni and V is formed through solid state amorphization caused by anomalously fast diffusion of Sn into Ni-V film. Thermodynamic information on the V-Sn system is scarce. It is therefore not known whether a criterion (i) above is met. Condition (ii) and (iii) are believed to have been satisfied in the present case.

2.8 Electrodeposition of Ni-W Film

Electrodeposition of Ni-W film has been studied extensively due to their outstanding properties (Yamasaki *et al.*, 2000; Haseeb, 2008a). For example, electrodeposition Ni-W alloy possesses higher thermal stability compared with nickel and nickel based alloys (Haseeb, 2008a; Haseeb, 2008b).

Ni-W alloy films were prepared on copper disc substrate by electrodeposition from an ammonia-citrate bath (Haseeb, 2008a). A range of Ni-W alloy films have been successfully electroplated from a nanocrystalline to an amorphous structure. According to Yamasaki *et al.* (1998), at W content below 20 at.%, these alloys are nanocrystalline in nature. A number of studies have been done on the amorphization of electrodeposited

Ni-W alloy (Yamasaki *et al.*, 1998; Haseeb, 2008b; Wang *et al.*, 2010a). It has been found that if W content is more than 25 at.% then the resulting alloy is amorphous.

The W content on its film is significantly related to the grain size of Ni-W alloy film. A smaller grain size, which is 2.4-6.8 nm was found by Yamasaki *et al.* (2000) and the W content is 22.5-17.7 at.%. Haseeb (2008a) reported that larger grain size was found at Ni with 12.08 at.% W. For a nanocrystalline Ni-W, it can be seen that grain size decreases with increasing of W on its film.

According to Haseeb (2008a), the addition of W makes the alloys structurally stable even when exposed to elevated temperatures. The phase diagram in Figure 2.13 indicates that at lower W content which is not more than 10 wt.%, Ni-W can stand for a temperature up to 1700 K. It was suggested that low diffusion coefficient of W atoms in Ni and their segregation to nanograin boundaries make these alloys more stable compared with other nickel alloys (Choi *et al.*, 2003; Detor *et al.*, 2006). From the view point of Ni-W alloy distribution, strong segregation of Ni-W was found in grain boundaries at high concentration of W atoms (Detor *et al.*, 2006).

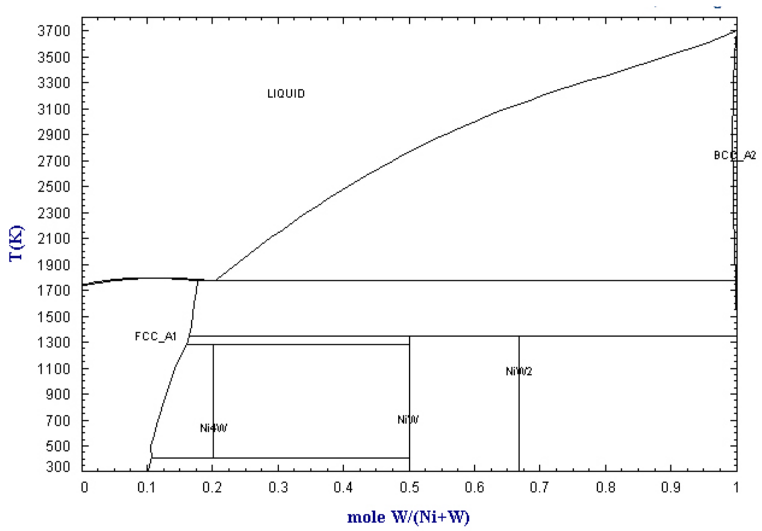

Figure 2.13: Ni-W phase diagram (*Data from FSlite*).

2.9 Presence of W in Ni film

The presence of W in transition metal based barrier film has been found to slow down the diffusion of copper (Dubin *et al.*, 1997). Use of W in barrier film between solder and copper substrate has been of interest (Zhu *et al.*, 1985; Lee *et al.*, 1994; Dubin *et al.*, 1997; Einati *et al.*, 2005). Figure 2.14 shows that only a solubility of about 0.001 at% W found at 2000 °C. No intermediate phase of Cu-W forms at 250 °C the soldering temperature. The binary Cu-W phase diagram revealed relativity low solubility of W in liquid Cu. So, it is expected that present of W would affect the interfacial reaction.

Refractory metal like tungsten and niobium have been found to have excellent barrier properties in contact with molten solder (Mannan, 2004). It has been suggested by Einati *et al.* (2005) that tungsten atoms preferentially gather at the grain boundary. Their presence at the grain boundary hinders the diffusion of copper atoms. Chen *et al.* (2006c) added W together with P to nickel barrier film and reported that the addition of W to Ni-W-P improved its high temperature resistance.

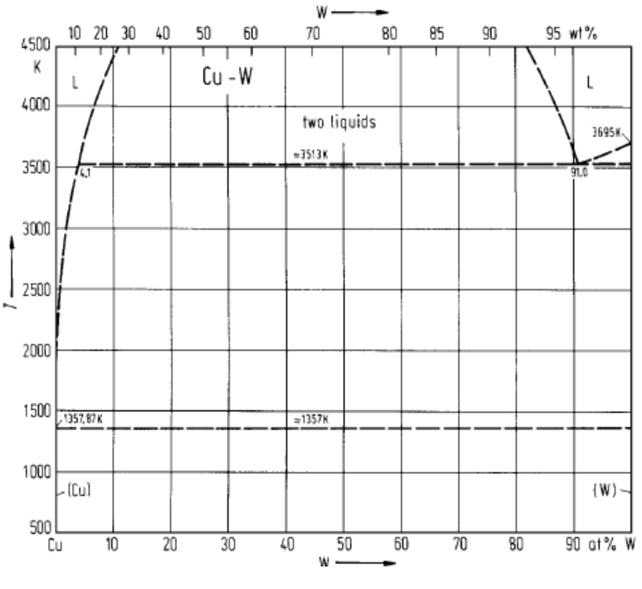

Figure 2.14: Cu-W phase diagram (Predel, *The Landolt-Börnstein Database*).

2.10 Nanoindentation

Interfacial reactions between lead free solders and substrate play an important role in the determining the reliability solders joints. The interfacial intermetallic compounds (IMC) are generally brittle and hence easily fail. The strength of solder joints decreases with the increasing of IMC thickness and these IMC acts as an initiation site for microcracks (Alam, 2003). In general, these IMC formed at the interface is several microns in thickness. Therefore, the mechanical properties across the solder joints must be carefully evaluated.

The mechanical properties of microelectronic materials at micron-scaled were performed by nanoindenter. Nanoindentation is a precise tool to examine and evaluate the mechanical properties of microelectronic materials at small-scaled without destroying the samples. The machine has a good ability in measuring the mechanical properties, specifically elastic modulus and hardness, of thin films on substrate (Huanga *et al.*, 2006). A few studies have been published for the investigated of mechanical properties on IMC by nanoindentation (Jang *et al.*, 2004; Tsai *et al.*, 2006; Xu, 2006, Marques *et al.*, 2009). The reduced modulus and hardness of the thin IMC layers were measured from the resulting force versus displacement curves. This technique is developed by Oliver (1992). The values that generated may be useful to understand the interconnection failure of solder joint.

CHAPTER 3: MATERIALS AND METHODS

3.1 Chemicals and materials

The bath constituents for electrodeposition of nickel and nickel-tungsten alloy were Nickel sulphate, $NiSO_4.6H_2O$ (Sigma-Aldrich Chemicals, purity 99 %), Sodium tungstate, $Na_2WO_4.2H_2O$ (Sigma-Aldrich Chemicals, purity 99 %), Sodium citrate, $Na_3C_6H_5O_7.2H_2O$ (Ajax Chemicals, purity 99 %), ammonium chloride, NH_4Cl (Ajax Chemicals, purity 99 %) and sodium bromide, NaBr (Ajax Chemicals, purity 99 %). The pH of the electrodeposition bath was adjusted with ammonia hydroxide, NH_4OH (Lab Chemicals, 28%) and sulfuric acid, H_2SO_4 (Merck, 65%). All materials were used without further purification.

The materials used in this study were copper sheet (purity 99.9 %, 30 mm x 30 mm x 0.3 mm), Sn-3.5Ag (SA) and Sn-3.8Ag-0.7Cu (SAC) solder paste (Indium Corporation of America, Singapore).

3.2 Electrodeposition of Ni and Ni-W alloy barrier films

In this experiment, Ni films were electrodeposited on copper substrate from Watts's bath. The bath composition and parameters used are given in Table 3.1. Copper sheet of dimension 30 mm x 30 mm x 0.3 mm was used as the substrate. Before plating, the copper substrate was cleaned with detergent (liquid dishwashing) and dipped in 10 vol. % H_2SO_4 to get rid of the oxide layer. It was rinsed with distilled water followed by drying with acetone. Electrodeposition of Ni was carried out galvanostatically at 20 mA/cm^2 at 57 $^oC \pm 2\,^oC$ with pH 3.5. The bath pH was adjusted by sulphuric acid or ammonia solution at room temperature. Ni films were coated to about 2.5 μm in thicknesses. After the deposition, coated substrates were cleaned with detergent and rinsed thoroughly in deionized water and dried with acetone.

Table 3.1: Components, concentration and operating parameters of electrodeposition of Ni in Watt's Bath.

Components	Concentration (g/L)
$NiSO_4.6H_2O$ Nickel chloride, $NiCl_2.6H_2O$ Boric acid, H_3BO_3	150 60 37.5
Operating Parameters	Tyipcal Range
pH Bath temperature Stirring Condition Current density Substrate	3.5 (adjust at room temperature) 57 °C Mild stirring (60rpm) with magnetic bath 20 mA/cm^2 0.3 mm thickness of Cu sheet

Ni-W alloy films were electrodeposited on the clean copper substrates. Figure 3.1 shows a schematic diagram of Ni-W electrodeposition bath. Table 3.2 shows the bath composition and parameters for electrodeposition. The Ni-W electrodeposition was carried out in an ammonia-citrate bath maintained at 80 °C ± 2 °C. The bath pH was adjusted to 8.5 by sulphuric acid or ammonia solution at room temperature. Deposition current density was 10 mA/cm^2 and Ni-W alloy films. Several depositions time were used in order to obtain a thickness of about 2.5 µm. Nickel and tungsten content of the bath was varied to deposit Ni-W with different W content.

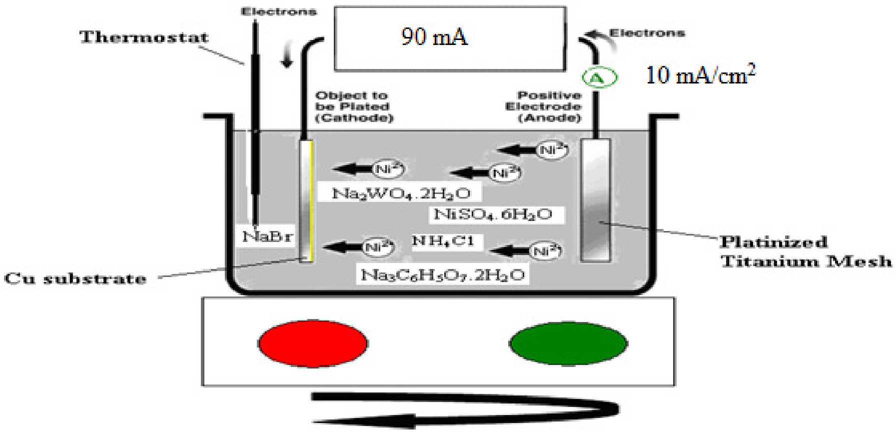

Figure 3.1: A schematic diagram of Ni-W electrodeposition bath.

Table 3.2: Components, Concentration and operating parameters of electrodeposition of Ni-W alloy via Ammonia-Citrate Bath

Components	Concentration (mol/L)
Nickel sulphate, $NiSO_4.6H_2O$	0.06-0.14
Sodium citrate, $Na_3C_6H_5O_7.2H_2O$	0.50
Sodium Tungstate, $Na_2WO_4.2H_2O$	0.14-0.28
Ammonium Chloride, NH_4Cl	0.5
Sodium Bromide, NaBr	0.15
Operating Parameters	Tyipcal Range
pH	8.5 (adjust at room temperature)
Bath temperature	85 ^{o}C
Stirring Condition	Mild stirring (60rpm) with magnetic bath
Current density	10 mA/cm^2
Substrate	0.3 mm thickness of Cu sheet

3.3 Preparation of solder on barrier films

Solder samples were prepared on Ni and Ni-W coated copper substrate. Before soldering, the substrates were cleaned with detergent and rinsed thoroughly in deionized water and dried with acetone. For the investigation of interfacial microstructural of two types of solder alloy, Sn-3.5Ag (SA) and Sn-3.8Ag-0.7Cu (SAC) solder paste were used. The solder was placed on electrodeposited substrate through a mask with 6.5 mm opening and 1.24 mm height. The solder paste was melted on the substrate at a peak temperature of 250°C. The reflow temperature profile is shown in Figure 3.2. After reflow process, the flux residue on the top of the solder was cleaned with acetone. Multiple reflow and high temperature storage were performed on a number of samples.

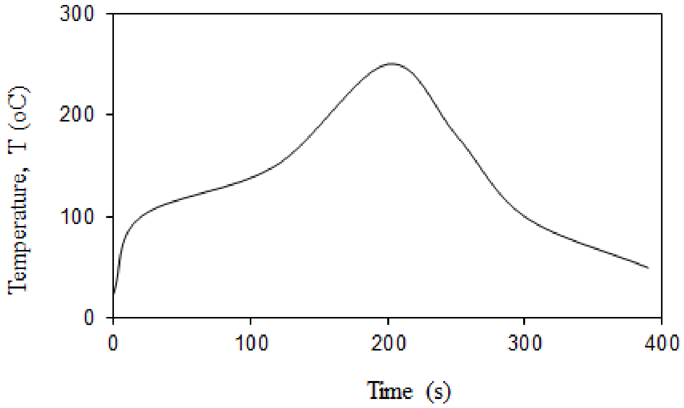

Figure 3.2: Temperature profile of reflowing process.

3.3.1 Multiple reflow

Multiple reflow process is used to enhance the interdiffusion and interaction between the solders and barrier films. It was carried out in a reflow oven (Forced convection, FT 02, Circuit Imprime Francais, France) at a peak temperature of 250 °C. Repeated reflow was conducted for up to 12 times cycles. Changes in morphology after twelve reflow cycles are compared and discussed on next chapter.

3.3.2 High temperature storage

High temperature storage was performed to accelerate the IMC growth. Samples were subjected to thermal aging at 150 ^{o}C in oven (Conventional Oven, Memmert) for 42 days.

3.4 Metallographic preparation

Samples were cut by sectioning machine and placed in 30 mm molding cup. A mixture of 15 ml epoxy resin and 2 ml hardener (EpoFit Kit, Struers) was poured into the cup. After 8 hours, epoxy resin polymerized through chemical reaction and the moulded sample was removed from the cup. Course grinding steps were employed to planarize the samples using first 400 grit SiC sand paper. This was followed by papers with 600, 800 and 1200 grit. The samples were then polished by abrasive particles (diamond suspension) on grinding cloth successively with a diamond grit size of 6 μm and 1 μm. A final oxide polishing was done by applying 0.04 μm colloidal silica particles on a polishing cloth to produce a scratch-free and deformation-free sample. The samples were cleaned and dried with hot air dryer.

3.5 Characterization method

The samples were studied by a few characterization methods. Spreading rate of the solder was calculated from Japanese Industrial Standard (JIS Z3198-3). The wetting angle was measured using optical light microscope (Meiji, MT7000). The micrographs were examined by backscattered electron detector under a field emission scanning electron microscope (Gemini FE-SEM, Zeiss). The elemental analysis was carried out by energy dispersive X-ray spectroscope (EDX, EDAX). Electron back scatter diffraction (EBSD, EDAX) analysis was used to identify the channeling pattern of the phase. Focus Ion Beam (FIB) was employed by milling across the interface for getting better contrast images. Electron probe microanalysis (EPMA, Cameca SX 100) with wavelength dispersive spectroscope (WDS) was used for elemental mapping. The topographies were characterized using atomic force microscope (AFM, Veeco, Singapore). Mechanical properties of the intermetallic compounds (IMC) formed between lead free solders and Ni-W alloy film were performed by nanoindenter (Micro Material, Wrexham, UK).

3.5.1 Spreading rate and wetting angles measurements

In this study, the Japanese Industrial Standard (JIS Z 3198-3) was used to obtain the spreading value. Spreading rate (%), S_R of the solder was calculated from equation (3.1 & 3.2).

$$D = 1.2407\, V^{1/3} \qquad 3.1$$

$$S_R = (D - H)/D \times 100 \qquad 3.2$$

D - diameter of the solder used for testing was considered as a ball shape

V - mass (g)/specific density of the SA and SAC solders

H - height of spread solder (mm)

The specific density of the SA and SAC solder was 7.08 g/cm^3 (Jang *et al.*, 2002) and 7.5 g/cm^3 (Liu *et al.*, 2008), respectively. More than six samples were calculated for each SA and SAC solders to obtain the quantitative results. Selective samples were cut and proceeded to metallographic preparation for wetting angle measurements. The optical microscope (Meiji, MT7000) was used to capture the cross-sectional images. The wetting angle was calculated via VideoTool Box Pro software (Zarbeco, USA) in the microscope.

3.5.2 Microstructural characterization

Optical Microscopy

After metallographic specimen preparation, the wetting angle was measured and the microstructure was observed under Meiji Microscope (MT7000). The optical microscope was used to capture images under light cameras (Halogen bulb 6V 30 W). The polished sample was placed in the focal plane and enlarged by lenses on optical microscope. A 10 x magnification eyepiece was used with other objectives lens (5x, 10x, 20x, 50x and 100x) that centered to the stage. The sample was viewed under the lowest to highest magnification. For getting a specific or interest areas, stage movement was controlled by x and y axis. The polarizing filter was engaged by dropping it into one filter slots to enhance the contrast of the features. The microscope was connected to a computer and images were saved via VideoTool Box Pro software. The wetting characteristic was recorded by angle measurements.

Field Emission Scanning Electron Microscopy (FE-SEM)

The cross-sectional samples were prepared according to the standard metallographic preparation. The interfacial microstructural was studied by field emission scanning electron microscope (FE-SEM) from Zeiss Gemini. The images was captured under back scattered electron (BSE) imaging at 8.5 mm working distance. All the samples were captured at this working distance; therefore, the IMC thickness can be compared and calculated. The average thickness of the interfacial IMC layer was measured by dividing the area covered by the layer by its length. The area measurements were done using Adobe Photoshop CS4 by employing the Magnetic Lesso Tools. For each experimental condition, the average thickness was calculated from at least four micrographs taken at randomly selected position on the cross sectional samples.

Electron Back Scatter Diffraction (EBSD)

Electron back scatter diffraction (EBSD, EDAX) analysis was used to identify the channeling pattern of the phase. For EBSD analysis, the sample was further polished with 1 μm colloidal silica to produce a cleaner surface for revealing better diffraction pattern. In EBSD, further sample preparation was needed to obtain better Kikuchi patterns. The microstructural crystallographic technique was used to identify the crystallographic orientation that formed between lead free solder and Ni-W barrier film. The sample was placed in the EBSD specimen stub (original titled with 45 ^{o}) and then further titled to 27^{o} to in the chamber. The detector was inserted and the pattern was collected at TSL Crystallography (OIM^{TM} Analysis Software).

Focus Ion Beam (FIB)

Focus ion beam (FIB) was employed by milling across the interface for getting better contrast images. FE-SEM was an electron beam source with ultra-high resolution, while FIB is Ga^{2+} ion beam source with high contrasting abilities. Both beams coincide at a crossover point 5mm below the objective lens of the FE-SEM.

FIB secondary electron images showed intense grain orientation contrast and grain morphology without any chemical etching. In specimen stub, mounted samples were grounded by silver paint and double-sided carbon tape. In the chamber, the sample was adjusted according to the eucentric and coincidence point, and then tilted to 52^{o} for milling normal to the sample surface. The milling parameter was started at 30KV:100 nA, 50 nA, 20 nA, 2 nA and 50 pA for 2 steps at each current ampere.

Atomic Force Microscope (AFM)

A contact mode atomic force microscope (AFM, Veeco, Singapore) was used in this study. A nano tip which attached to the end of a cantilever scanned across the polished surface and the topographies were monitored. A constant cantilever deflection and the adhesion force between the tip and sample remained constant in the contact mode. A Derjaguin-Muller-Toporov (DMT) model of adhesion forces was employed. Luo (2006) suggested that DMT model can be used in the case of rigid systems, low adhesion and small radii of curvature. Topographical height across the sample surface was displayed by DMT model.

3.5.3 Chemical analysis

Energy Dispersive X-ray Spectroscopy (EDX)

The energy dispersive X-ray spectroscope (EDX, EDAX) was used to analyze chemical composition of the IMC that formed at the interface between solders and substrate. The EDX analysis was carried out after capturing the FE-SEM images. The voltage used at this testing should be more that 10 kV and located at 8 mm working distance in order to obtain quantitative elemental analysis.

Electron Probe Microanalysis (EPMA)

Electron probe micro-analyzer (Cameca, SX100) was used to determine the chemical compositions, elemental mapping and line scanning across the IMC. The quantitative elemental analyses at micron spot were performed by wavelength-dispersive spectroscope (WDS) using a 20kV electron beam accelerating voltage and 20 nA probe current. Before testing, the polished samples were coated with gold-palladium to prevent charging for generating better images.

3.5.4 Nanoindentation Test

Nanoindentation test was done on the SA and SAC solders after six time reflows. The purpose of this test was to compare the hardness of the coarsen intermetallic and Young Modulus's values of both sample. The indentation equipment (Micro Materials, Wrexham, United Kingdom) was assembled with the Berkovich indenter to indent on the define area. The tests were carried out at 25 ^{o}C. Indentation tests were performed across the solder-substrate interface at a peak load of 0.5 mN at a load/unload rate of 0.025 mN/s. A (10 x 10) grid programmed as 100 indentations with 2 μm indent spacing and (15 x 25) angled grid as 375 indentations with 1 μm indent spacing were studied. Hardness and reduced elastic modulus were measured for different intermetallic phases.

CHAPTER 4: RESULTS AND DISCUSSION

4.1 Characterization of electrodeposited Ni-W alloy films

4.1.1 Tungsten content and morphology

EDX analyses of the Ni-W alloy films deposited from four different baths are shown in Table 4.1. Deposits with four different W contents viz., 5.0, 11.3, 16.0 and 18.0 at.% W were obtained. As expected, electrodeposition bath with lower nickel to tungsten ratio yielded deposit with higher W content. Earlier study shows that such films possess nanocrystalline structure with average grain size in the range of about 20 nm (Haseeb, 2008b; Kilmenkov *et al.*, 2009). To studying the effect of W contents, three different compositions were chosen for further investigation.

Table 4.1: Tungsten content of Ni-W alloy electrodeposits obtained from various baths.

$NiSO_4.6H_2O$ (mol/L)	$Na_2WO_4.2H_2O$ (mol/L)	Ni/W Ratio in the Bath	Deposited W content (at. %)
0.33	0.01	33.0	5.0
0.22	0.07	31.4	11.3
0.10	0.14	0.71	16.0
0.06	0.14	0.43	18.0

The surface morphology of deposits obtained at various W contents is shown in Figure 4.1. At Ni-5 at.% W, the surface morphology forms by elongated and globular structures. The morphology becomes globular at Ni- 11.3 at.% W. A smoother surface can be seen at higher tungsten content which is Ni-18 at.% W. Haseeb (2008a) revealed that larger grain size is due to lower W content of the deposit. A smaller grain size, 2.4-6.8 nm in their Ni-W alloy with 22.5-17.7 at.% W obtained by Yamasaki *et al.* (2000).

In this study, all samples were deposited at a current density of 10 mA/cm^2. The average grains size of samples deposited at10 mA/cm^2 is about 20 nm (Haseeb *et al.*, 2007).

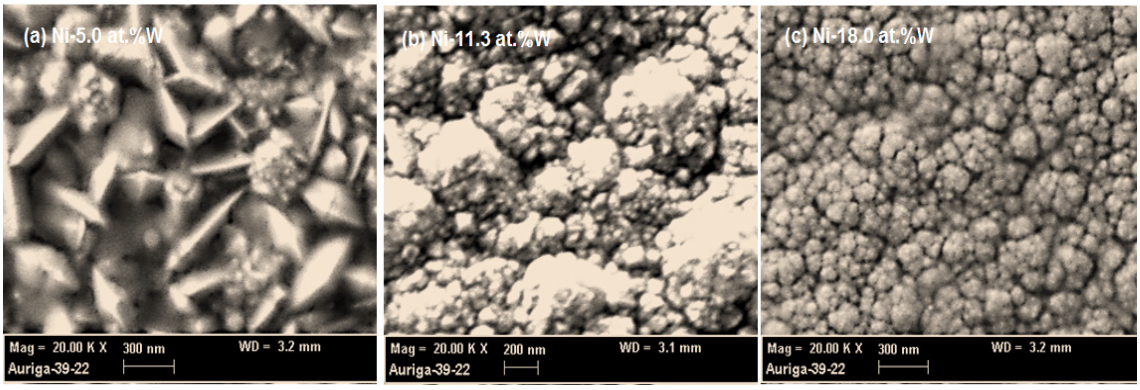

Figure 4.1: Morphology of the deposits obtained at different W content: a) Ni-5 at.% W, b) Ni-11.3 at.% W and c) Ni-18 at.% W.

4.1.2 Optimization of thickness and deposition time of Ni-W layer

In general, deposition time controlled the thickness of Ni-W barrier layer. A series of samples were deposited with a range of deposition time. The thickness of each sample with different W content was recorded and is shown in Figure 4.2 as a function of deposition time. The thickness of deposition increases with time. However, the deposition of Ni-18 at.% W shows a slightly decreasing trend at around 140 minutes. The slight change in the deposition rate is probably related to a loss of ammonia during deposition (Haseeb, 2008a). It is due to the decrease of cathodic current efficiency (Brenner, 1963; Yamasaki *et al.*, 1998). In present case, the tungsten content of deposit did not significantly change with time. A thickness about 2.5 µm was aimed in this study, horizontal line in Figure 4.2.

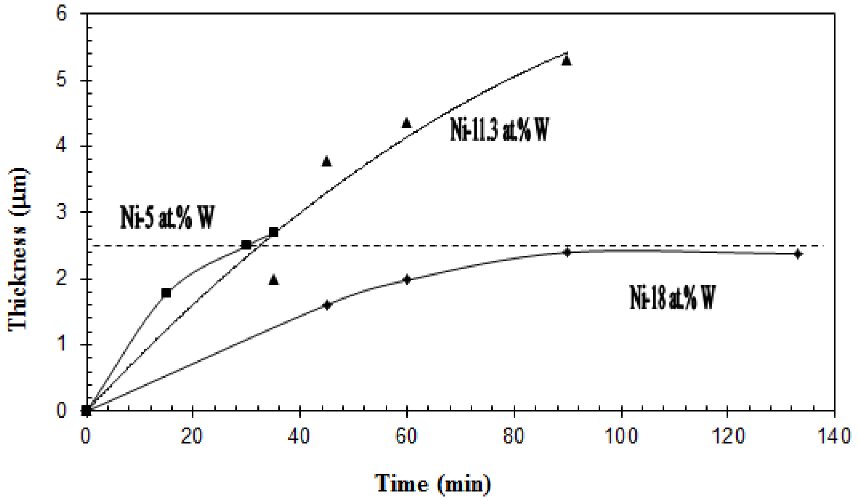

Figure 4.2: Various plating thickness in the function of time.

Table 4.2 displays the deposition time required to achieve 2.5 µm thick Ni-W alloy films with different W content. It is seen that 5 at.% W film requires shorter deposition time as compared with 18 at.% W film. Three different W content were chosen for further investigation, which are 5, 11.3 and 18 at.%. For comparison purposes, electroplated Ni films were studied. The thickness of electroplated Ni film is 2.5 µm at 15 minutes deposition time.

Table 4.2: Deposition time of W plating with 5, 11.3 and 18 at.%.

Sample	Exposing Area (cm x cm) I = 360 mA	Deposition Time (min)	Thickness (µm)
Ni-5.0 at.% W	6.0 x 6.0	30 min	2.5
Ni-11.3 at.% W	6.0 x 6.0	40 min	2.5
Ni-18.0 at.% W	6.0 x 6.0	120 min	2.5

4.2 Wetting behaviour of solder on Ni-W films

4.2.1 Wetting angle and spreading rate of Sn-3.5Ag solder (SA)

Figure 4.3 shows spreading rate Sn-3.5Ag solder on Ni and Ni-W alloy films. The box plot data shows a decreasing trend with respect to W content in Ni-W alloy. The spreading rate of solder on pure Ni is calculated as 88.94%±12.6. The quantitative results are based on 10 values. Given the accuracy of the measurements, it can be suggested that incorporation of W does significantly decrease the spreading rate of SA solder.

Figure 4.4 (a) and (b) show cross sectional view of Sn-3.5Ag solder on Ni film and SA solder on Ni-5 at.% W film, respectively. The angles are comparable in both cases. Wetting angle on pure Ni film is 13.4°±3.4 that obtained from two cross-sectional samples. The variation of wetting angle of different W content is shown Figure 4.5. The graph shows an unclear trend with respect to W content in Ni-W alloy. In view of the scatter, it may be due to only four different angle measurements were collected for each film.

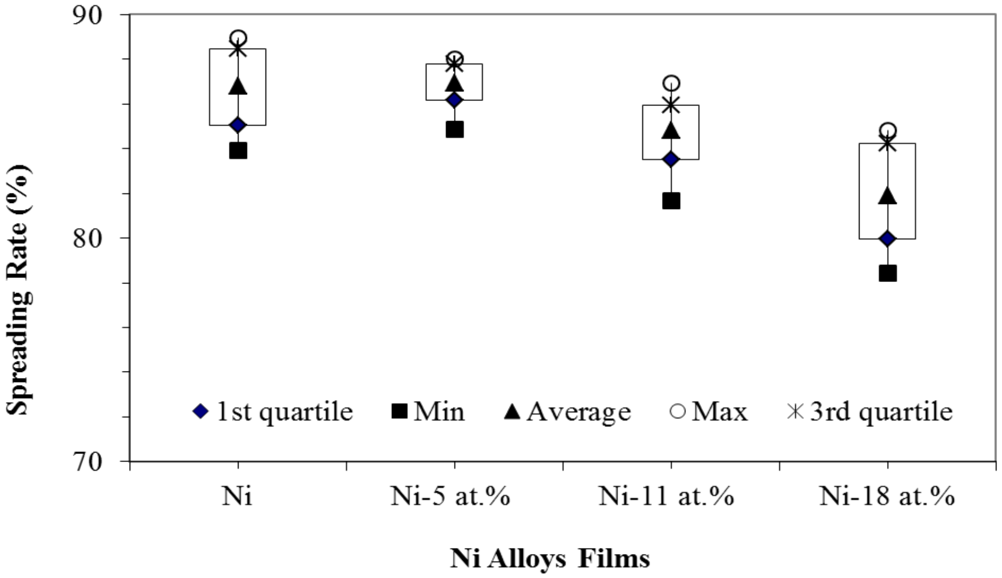

Figure 4.3: Spreading rate of SA solder on Ni and Ni-W alloy films

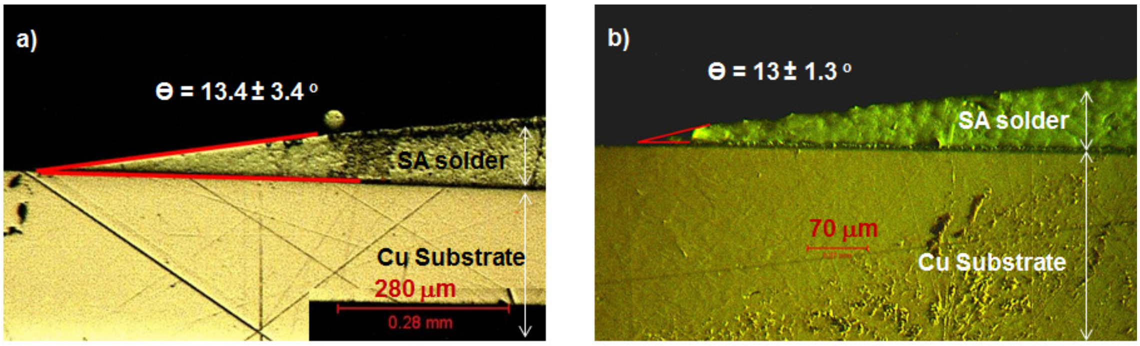

Figure 4.4: Cross sectional micrographs showing wetting angle for a) SA/ Ni and b) SA/Ni-5 at.% W.

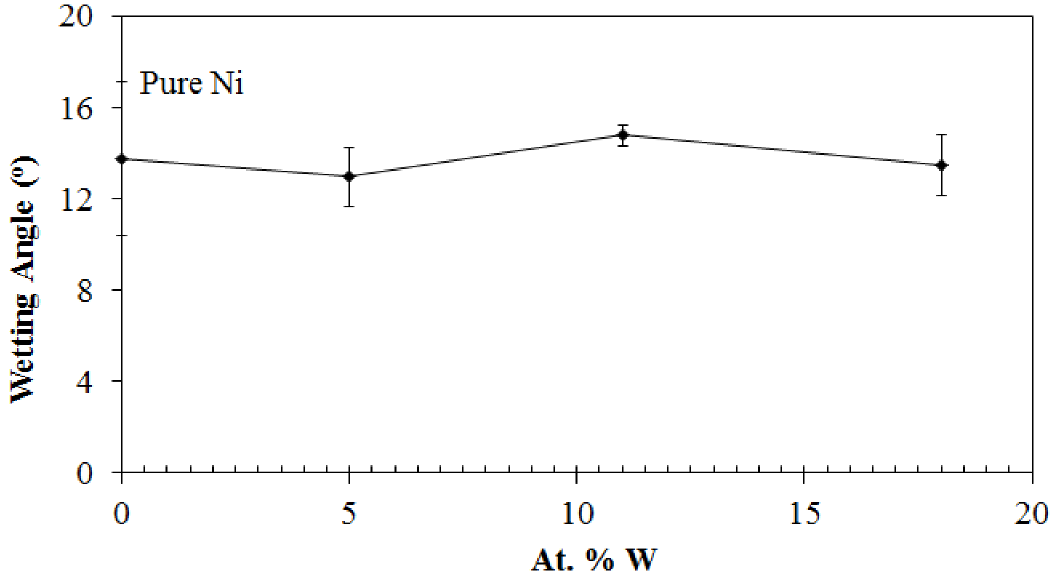

Figure 4.5: Wetting angle of SA solder on Ni and Ni-W alloy films.

4.2.2 Wetting angle and spreading rate of Sn-3.8Ag-0.7Cu solder (SAC)

Figure 4.6 shows the box plot of spreading rate of Sn-3.8Ag-0.7Cu solder on pure Ni and Ni-W alloy. It can be seen that the spreading rate decreases with increasing of W content in Ni-W alloy. Considering the experiments accuracy, it is behaved that W content does significantly influence the spreading behaviour.

Figure 4.7 shows the wetting angle of Sn-3.8Ag-0.7Cu on pure Ni film and Ni-18 at.% W film. The angles are measured to be 13.15°±5.4 and 14.20°±2.1 for pure Ni and Ni-18 at.% W film, respectively. Figure 4.8 shows the wetting angle as the function of W content in Ni-W alloy.

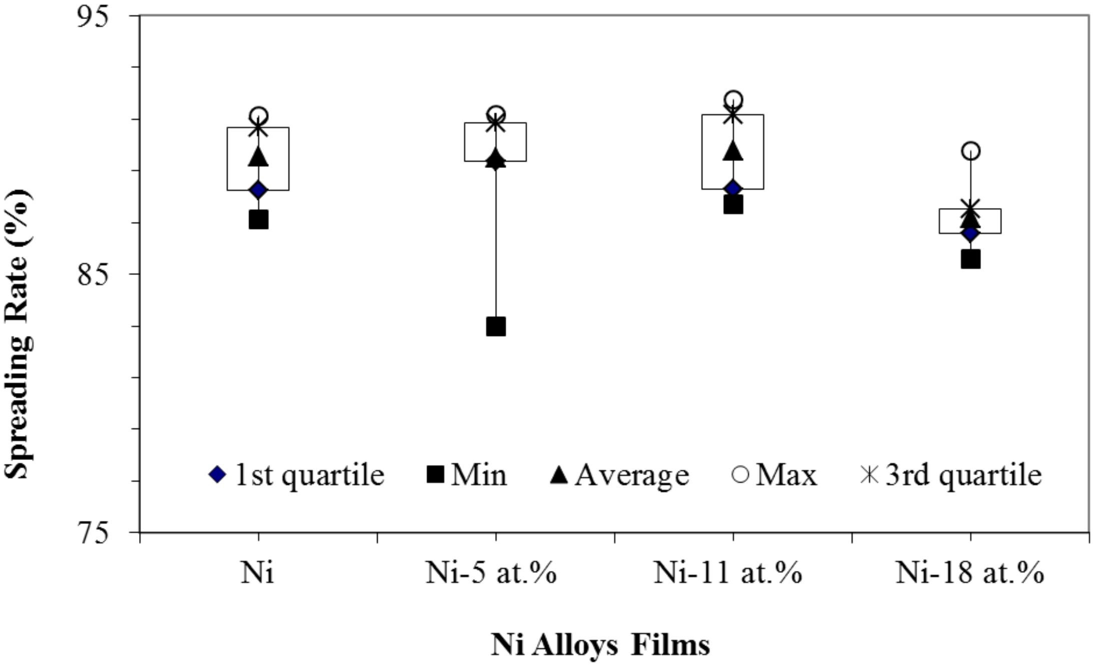

Figure 4.6: Spreading rate of SAC solder on Ni and Ni-W alloy films.

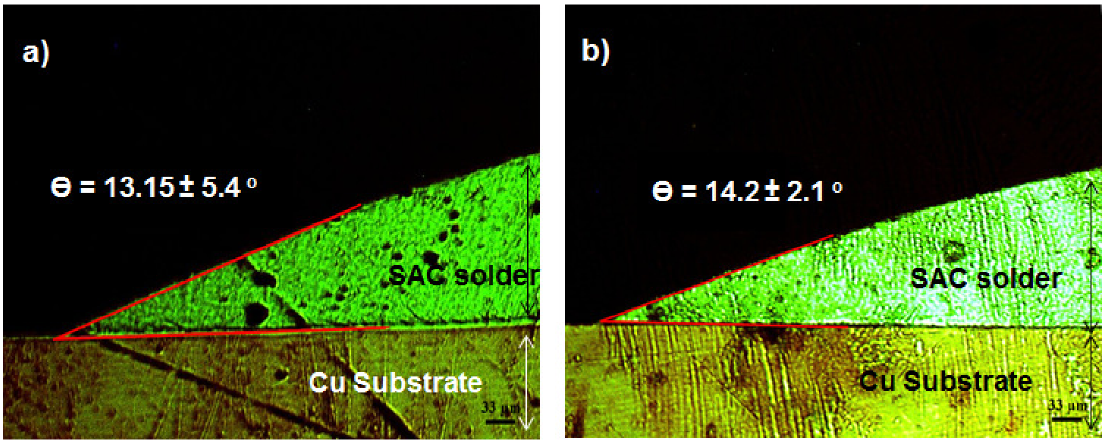

Figure 4.7: Cross sectional micrographs of wetting angle a) SAC/ Ni and b) SAC/Ni-18 at.% W.

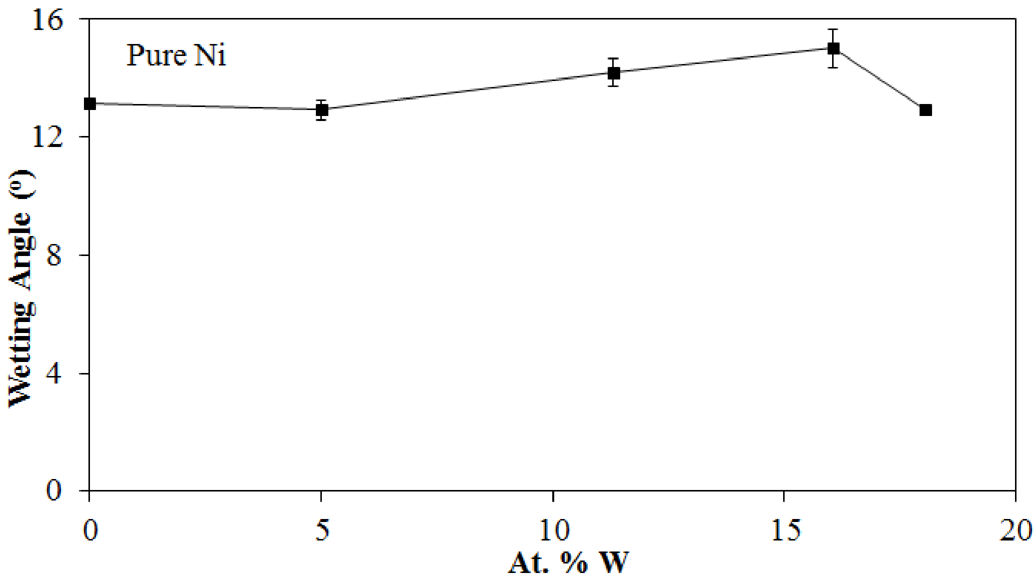

Figure 4.8: Wetting angle of SAC solder on Ni and Ni-W alloy films.

The above results show that spreading rate decreases with increasing of W content in Ni-W alloy for both SA and SAC solders. In the theoretical expectation, wetting angle increases with decreasing of spreading rate. In fact, there is some scatter values due to the few cross sectional samples were determined for wetting angle. The wetting angle of SA and SAC solder on Ni-W alloy is found to be in the range of 12.98^o ~ 14.20^o, which is well within the range of Sn based solder reported in literature review (Guo *et al.*, 2000; Kripesh *et al.*, 2001). Suganuma (2001) reported that a good and reliable interconnection requires a small wetting angle, which is between $0^o \leq \theta \leq 20^o$.

However, the changes of the spreading rate are caused by intermetallic compounds that formed between solders and substrate materials (Pandher, 2006). Interfacial reactions between the solder and barrier layer will be discussed in detail below.

4.3 Interfacial reaction during reflow soldering

4.3.1 Formation of microstructure at interface of Sn-3.5Ag

Figure 4.9 shows cross sectional FE-SEM micrographs of the interface between SA and Ni as well as Ni-W alloy barrier films after first reflow. A small and more or less uniform intermetallic compound (IMC) formed between SA solder and Ni film (Figure 4.9a). EDX analysis revealed that the IMC is Ni_3Sn_4, as tabulated in Table 4.3.

Table 4.3: Composition of Ni-Sn IMC on different barrier films after first reflow and twelve reflow cycles.

Barrier film		Average Composition of Ni-Sn IMC, at.%			Identified Phase
		Ni	Sn	Ni/Sn Ratio	
Ni	1 x	46.98	53.02	0.89	Ni_3Sn_4
	12 x	47.86	52.14	0.92	Ni_3Sn_4
Ni-5 at.% W	1 x	48.21	51.79	0.93	Ni_3Sn_4
	12 x	47.71	52.29	0.91	Ni_3Sn_4
Ni-11.3 at.% W	1 x	47.60	52.40	0.91	Ni_3Sn_4
	12 x	49.70	50.30	0.98	Ni_3Sn_4
Ni-18 at.% W	1 x	49.44	50.56	0.97	Ni_3Sn_4
	12 x	48.75	51.25	0.95	Ni_3Sn_4

In contrast, two layers form at the interface between SA and Ni-W alloy films, as shown in Figure 4.9 (b-d). The outer layer close to the solder possesses faceted grains. Elemental ratio determined by EDX on the layer showed it to be Ni_3Sn_4. Grooves can be observed in between faceted Ni_3Sn_4 grains. The thickness of the Ni_3Sn_4 layer is the largest on Ni-5 at.% W. The thickness of Ni_3Sn_4 decreases as the W content in the barrier film increases. The second layer forms below the Ni_3Sn_4 layer. It has a bright contrast. EDX analysis showed that the bright layer contains Sn, Ni and W. The bright layer thickness does not seem to vary with W content.

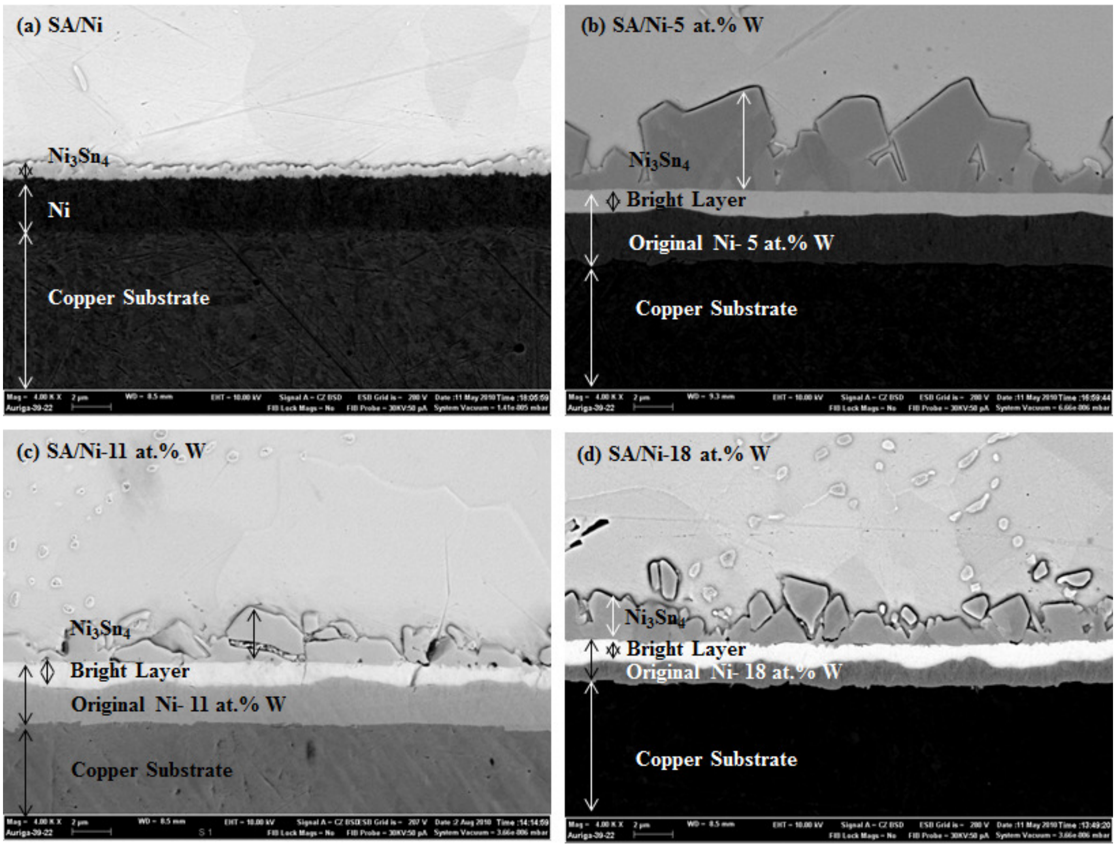

Figure 4.9: Cross-sectional back scattered electron image of interface between SA and barrier films after first reflow: (a) Ni, (b) Ni-5 at.% W, (c) Ni-11.3 at.% W, and (d) Ni-18 at.% W.

It is found that the thinnest Ni_3Sn_4 forms on the Ni film compared with that at Ni-W alloy films. According to Dybkov (2008), small grain and thin Ni_3Sn_4 IMC formed between Sn based solder and Ni film. Initially, the solder was in the molten state for about 45 s and Ni_3Sn_4 IMC was formed under conditions with their simultaneous dissolution of Ni solid metal in the molten solder. The thinnest Ni_3Sn_4 is due to the dissolution of Ni solid metal in the liquid phase.

A thicker Ni_3Sn_4 IMC formed at the interface between SA and Ni-W alloy films is related to the relative ease of Ni atoms that removed from its layer. According to Li *et al.* (2006), the result of thicker IMC formed between lead free solder and barrier layers is associated to the relative ease with which atoms can be removed from their native lattice.

The rate of loss of Ni atoms can be represented by the Arrhenius equation (Li *et al.*, 2006):

$$-\frac{dh}{dt} = k \exp\left(-\frac{E_a}{RT_s}\right) \qquad (4.1)$$

in which h is the thickness of the solid metal, t is time, k is a constant combining geometrical factors such as lattice spacing and the rate constant of the reaction, T_s is the storage temperature of the sample and E_a is activation energy per mole of loss of material for a general chemical reaction.

According to Gur *et al.* (1998), the activation energy of Ni film to react and form Ni_3Sn_4 IMC is 27.6 $kcalmo1^{-1}$. This value corresponds to the activation energy for the diffusion of Ni in liquid Sn in the temperature range of 235°C to 600°C. The activation energy for the formation of Ni_3Sn_4 at Ni-7 at.% W film was found to be 20.9 $kcalmol^{-1}$ (Harada *et al.*, 1997). This value is related to the Ni atoms that diffused out and formed Ni_3Sn_4 IMC in matrix solder region.

Based on lower activation energy found in Ni-W alloy film, the rate loss of nickel atoms is relatively fast. It could be the reason of why thicker Ni_3Sn_4 layer is observed at SA and Ni-W alloy films Figure 4.9 (b-d). On the contrary, the rate loss of nickel atoms in Ni film is relatively slow due to the higher activation energy found in Ni film. Therefore, a thinner Ni_3Sn_4 layer is observed at SA and Ni film interface Figure 4.9a.

Cross-sectional micrographs of the interface between SA and the barrier films after twelve reflow cycles are shown in Figure 4.10. Continuous, compact and large grains Ni_3Sn_4 IMC was formed at interface of SA and Ni film as shown in Figure 4.10. The morphology of Ni_3Sn_4 IMC at Ni interface was changed from small to large grains after twelve reflow cycles (Figure 4.9a & Figure 4.10a). Two layers are seen at the interface between SA and Ni-W alloy films as shown in Figure 4.10 (b-d). It can be seen that the Ni_3Sn_4 and bright layers grew thicker after twelve reflow cycles. The thickness of the Ni_3Sn_4 layer is the largest on the Ni-5 at.% W film (Figure 4.10b). The thickness of the Ni_3Sn_4 layer decreases as the W content in the barrier film increases. This observation is similar to the case of one time reflow.

The bright layer grew slightly thicker compared with the first reflow case. Figure 4.11 presents the thickness of Ni_3Sn_4 IMC and bright layer after the first and twelve reflow cycles. This figure clearly reveals the trend in the variation of both layer thicknesses as a function of W content in the barrier films.

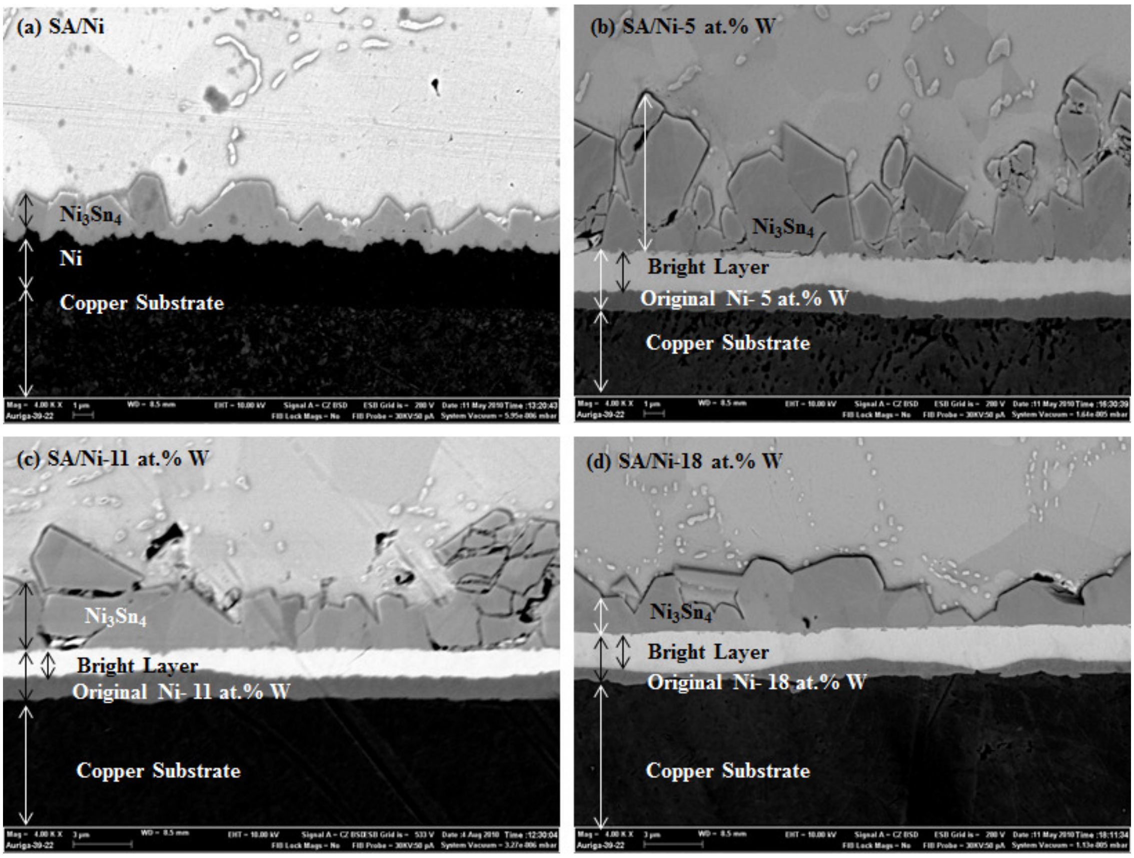

Figure 4.10: Cross-sectional back scattered electron image of interface between SA and Ni film and Ni-W alloy barrier films after twelve reflow cycles: a) Ni, b) Ni-5 at.% W, c) Ni-11.3 at.% W, and d) Ni-18 at.% W.

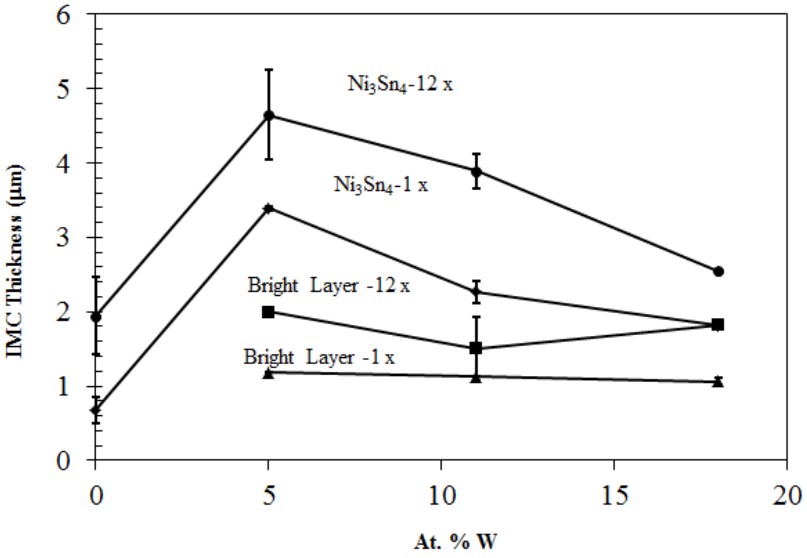

Figure 4.11: Growth of Ni_3Sn_4 IMC thickness and bright layer on Ni, Ni-5.0 at % W, Ni-11.3 at % W and Ni-18.0 at % W films for first reflow and twelve reflow cycles.

As discussed already, the thickness of Ni_3Sn_4 first increases as the W content in the barrier film increases. The thickness then decreases upon further addition of W. Maximum Ni_3Sn_4 thickness is observed at 5 at.% W. The thicknesses of both Ni_3Sn_4 and the bright layers show an increasing after twelve reflows. The bright layer thickness, on the other hand, remains insensitive to W content of Ni-W films. The decrease of Ni_3Sn_4 thickness with the increase in W content in the barrier layer is similar to the case for Ni-P and Ni-B barrier films, where the thickness of Ni_3Sn_4 was found to decrease with the increase of P and B content (Yoon *et al.*, 2008; Yoon *et al.*, 2010).

A number of studies have been done on the amorphization of electrodeposited Ni-W alloy (Yamasaki *et al.*, 1998; Haseeb, 2008b; Wang *et al.*, 2010a). It has been found that if W content is more than 25 at.% then the resulting alloy is amorphous. In the present case all the alloy used as barrier film have less than this threshold W content and hence are nanocrystalline (Haseeb, 2008a; Kilmenkov *et al.*, 2009).

From the above results, the Ni_3Sn_4 layer decreases in following order after first reflow and twelve reflow cycles: Ni-5 at.% W > Ni-11.3 at.% W > Ni-18 at.% W. The phenomenon is significantly related to the W content in electrodeposited films. It can be seen that with highest W content which is Ni-18 at.% W, the lowest Ni_3Sn_4 layer was formed. The decrease of Ni_3Sn_4 layer at Ni-18 at.% W interface might due to decreasing of crystallinity of this film. From the view point of Ni-W alloy distribution, strong segregation of Ni-W was found in grain boundaries at high concentration of W atoms (Detor *et al.*, 2006). Tungsten atoms are thought to act as 'pinning agent' at grain boundaries and have reduced the growth of Ni_3Sn_4 IMC between SA and Ni-18 at.% W.

EDX line scan recorded across SA/Ni-18 at.% W interface after first reflow is shown in Figure 4.12. Approaching the interface from the substrate side, nickel profile shows a decrease in nickel content in the bright layer. The Ni content then increases at the Ni_3Sn_4 layer. Tin content is seen to increase as the bright layer is approached from the substrate side. Tin content keeps on increasing in Ni_3Sn_4 and then in the solder matrix. Tungsten content is high in areas between the substrate and Ni_3Sn_4. No tungsten is found in copper substrate and Ni_3Sn_4.

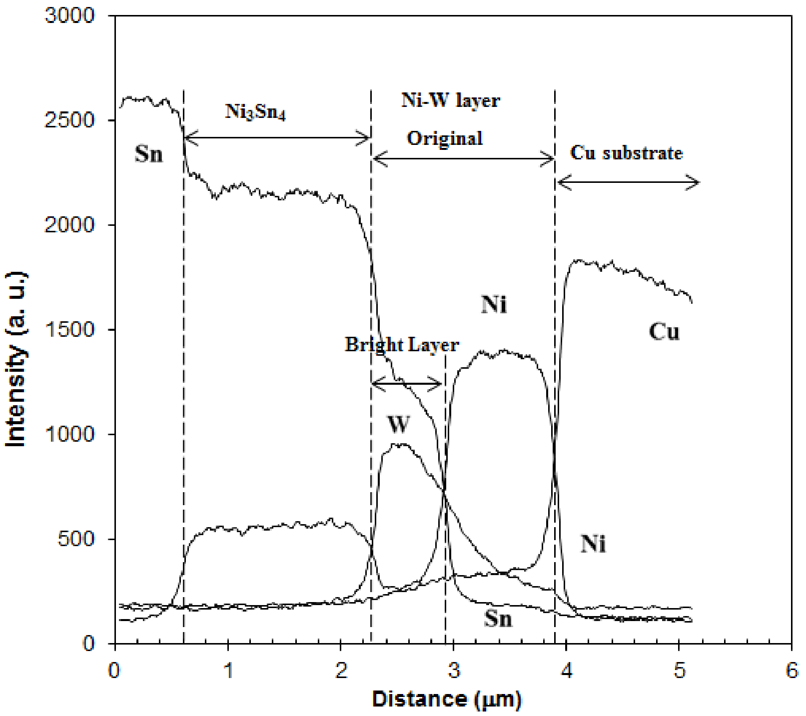

Figure 4.12: EDX line profiles across the interface of SA/Ni-18 at.% W couple after first reflow.

Table 4.4 shows the average composition of the bright layer that formed after twelve reflow cycles on different Ni-W films. It is seen that tin is the major constituent in the bright layer accounting for half of its content. The amount of nickel in the bright layer is far smaller compared with the original nickel content of the Ni-W film. This bright layer is contained of Sn, Ni and W and is written as Sn-Ni-W layer.

Table 4.4: Composition of bright layer on different Ni-W barrier film after twelve reflow cycles.

Barrier film	Composition of Bright layer, at.%		
	Ni	W	Sn
Ni-5 at.% W	28.55	21.55	49.90
Ni-18 at.% W	19.29	30.24	50.47

Figure 4.13 shows the EBSD pattern recorded on different phases at the interface after twelve reflow cycles. The channeling pattern taken on Ni_3Sn_4 shows well-formed Kikuchi lines representative of a crystalline structure. Indexing revealed that the pattern corresponds to Ni_3Sn_4. Channeling pattern coming out of Ni-W layer shows Kikuchi line corresponding to a fcc phase. It may be noted that electrodeposited Ni-W alloy with W content used in the study possess the fcc lattice of host nickel (Haseeb *et al.*, 2008; Kilmenkov *et al.*, 2009). The pattern for Ni-W film is less pronounced. Small *et al.* (2002) reported the effect of grain size on the quality of EBSD pattern. They observed that the pattern quality becomes poorer when the grain size is in the nanometer range. Therefore, the poor pattern quality for Ni-W alloy film is attributed to the nanocrystalline nature of Ni-W layer. For Sn-Ni-W layer, no discernable pattern is visible. This suggests lack of long range order and hence amorphous nature of the Sn-Ni-W layer (Cadneya *et al.*, 2009).

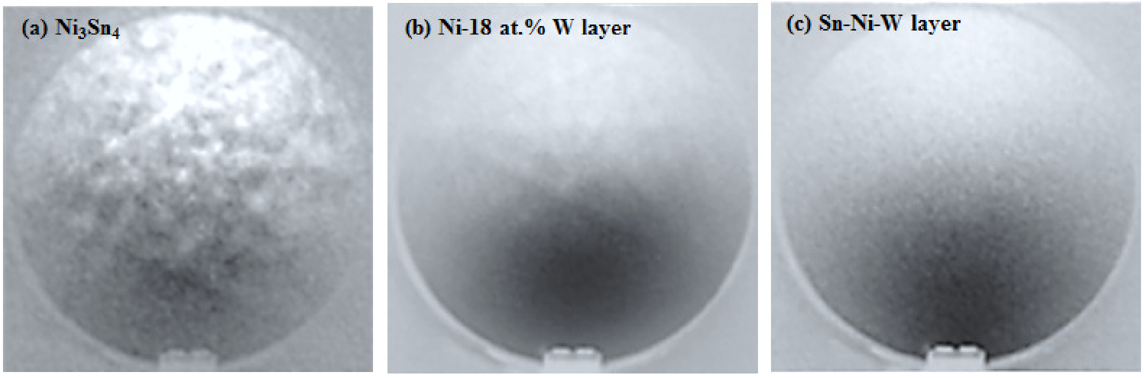

Figure 4.13: EBSD patterns recorded on different phases after 12 reflow cycles a) Ni_3Sn_4, b) Ni-18 at.% W layer and c) Sn-Ni-W layer.

The above results show the Sn-Ni-W layer forms on the outer side (close to solder) of the Ni-W alloy barrier films after reflow (Figure 4.9 and Figure 4.10). The Sn-Ni-W layer tends to consume the Ni-W layer after repeated reflow. EDX line scan shows that Sn entered into the Sn-Ni-W layer, whereas nickel diffused out to form Ni_3Sn_4. EDX further shows that W did not diffuse out to the solder or to the substrate. Preliminary EBSD pattern suggests that the Sn-Ni-W layer is amorphous.

As mentioned earlier, the Ni-W alloy films that were deposited in this study belong to nanocrystalline structure. It is impossible for these nanocrystalline alloy films to turn into amorphous structure simply by heating at 250°C. The amorphous structure of Sn-Ni-W is therefore mainly related to the influx of tin atoms into it.

In the case of SA on Ni-P film, the out diffusion of Ni atoms to form Ni_3Sn_4 IMC enhanced the transformation of Ni-P film into P rich, nanocrystalline Ni_3P layer (He *et al.*, 2004a; Yoon *et al.*, 2010). This transformation is termed as “solder reaction-assisted crystallization (Jang *et al.*, 1999).

In contrast, the Sn-Ni-W layer that formed between Ni_3Sn_4 layer and Ni-W alloy film is related to solid state amorphization. Solid state amorphization in thin film systems has been studied by many researchers (Schward, 1983; Benedictus *et al.*, 1999; Lai, 1999). There are three main criteria to meet for this amorphization process to take place between two components in thin film: (i) the two components possess a large negative heat of mixing in the amorphous state, (ii) one component has anomalously high diffusion coefficient compared with the other, and (iii) reaction occurs at a temperature low enough to suppress the nucleation/growth of thermodynamically preferred crystalline phases.

In the present case, it is not certain if the first criterion is met because the thermodynamic information on the W-Sn system is scarce. Criterions (ii) and (iii) are believed to have been met in the present case. Shen *et al.* (2009) studied interfacial between tin and nickel. They found that tin atoms diffuse much faster than nickel atoms. As a result, the mechanism of formation of Ni_3Sn_4 at the interface is characterized by inward diffusion of Sn atoms. According to Table 4.4, the ternary Sn-Ni-W layer contain tin as its major constituent (≈ 50 at.%) and is can be seen that higher tin atoms diffuse inward Ni-W film. It is evident from EDX data (Table 4.4) that tin atoms have moved into barrier film, whereas W atoms do not move out at all. Therefore, it is believed that the anomalously fast diffusion of tin atoms into Ni-W film has contributed to the solid state amorphization leading to the formation of the amorphous ternary Sn-Ni-W phase.

Solid state amorphization is observed between two crystalline metals at temperature below the glass transition temperature (Huh, 2000). In present case, the electrodeposition Ni-W alloy film is found to be nanocrystalline structure. Chen (2006a) revealed that Ni_3Sn_4 grains is also a crystalline structure by TEM analysis. A bright (Sn-Ni-W) layer is seen to form between Ni-W crystalline film and Ni_3Sn_4 crystalline structure. It may be noted that amorphous layer formation was also observed by Chen (2006a) for Ni-V barrier film. They found that a bright layer formed when vanadium content of the Ni-V layer was more than 5 at.% (Chen *et al.*, 2006b). Analysis showed that the bright layer contains Sn, Ni and V. They termed this ternary phase as ‘T’ phase. TEM revealed the bright layer to be amorphous (Chen *et al.*, 2007b). They also reported that ‘T’ phase is formed through solid state amorphization.

4.3.2 Formation of microstructure at interface of Sn-3.8Ag-0.7Cu

Figure 4.14 reveals the interfacial microstructure between Sn-3.8Ag-0.7Cu (SAC) and Ni and as well as Ni-W alloy barrier films after first reflow. The interface of SAC and Ni film shows a continuous and compact IMC, as shown in Figure 4.14a. EDX analysis identified that the IMC is $(Cu,Ni)_6Sn_5$ as listed in Table 4.5.

Two layers form at the interface between SAC and Ni-W alloy films as shown in Figure 4.14 (b-d). The outer layer, darker in appearance, is uniform and chunky type formed at the interface between SAC and Ni-5 at.% W. Elemental ratio obtained from EDX result suggested that darker layer is $(Cu,Ni)_6Sn_5$ IMC. The second layer which is much thinner and brighten in appearance formed below $(Cu,Ni)_6Sn_5$ layer. EDX analysis showed that the bright layer contains Sn, Cu, Ni and W.

Table 4.5: Composition of Ni-Cu-Sn IMC on different barrier films after first reflow and twelve reflow cycles.

Barrier film		Average Composition of Ni-Cu-Sn IMC, at.%			Identified Phase
		Ni	Cu	Sn	
Ni	1 x	13.36	52.11	34.54	$(Cu,Ni)_6Sn_5$
	12 x	15.82	38.60	45.58	$(Cu,Ni)_6Sn_5$
Ni-5 at.% W	1 x	12.16	50.90	36.94	$(Cu,Ni)_6Sn_5$
	12 x	28.66	33.44	37.91	$(Cu,Ni)_6Sn_5$
Ni-11.3 at.% W	1 x	13.17	52.48	34.35	$(Cu,Ni)_6Sn_5$
	12 x	22.18	33.32	44.50	$(Cu,Ni)_6Sn_5$
Ni-18 at.% W	1 x	13.54	50.72	35.42	$(Cu,Ni)_6Sn_5$
	12 x	20.07	36.82	43.11	$(Cu,Ni)_6Sn_5$

It can be seen that a continuous and compact $(Cu,Ni)_6Sn_5$ layer form at the interface between SAC and Ni-11.3 at.% W. In contrast, a non-uniform and discontinuous $(Cu,Ni)_6Sn_5$ layer forms on Ni-18 at.% W interface. The thickness of $(Cu,Ni)_6Sn_5$ layer decreases with increasing of W content. This is similar to the case of Ni_3Sn_4 layer thickness that found to decrease with the increase of W content at SA interface. The thickness of the bright layer remains insensitive to W content.

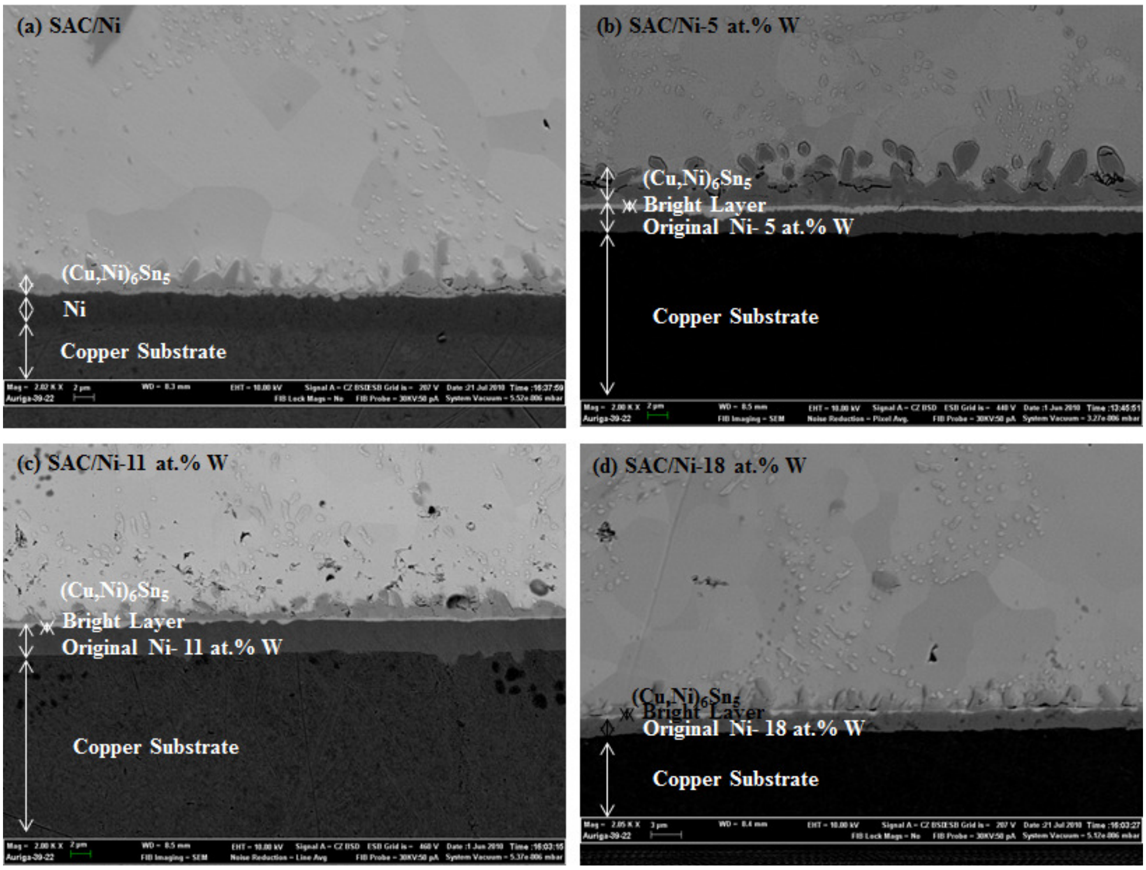

Figure 4.14: Cross sectional back scattered electron images of interface between SAC and barrier films after first reflow: a) Ni, b) Ni- 5 at.% W, c) Ni-11.3 at.% W and d) Ni-18.% W.

Cross-sectional micrographs of the interface between SAC and barrier films after twelve reflow cycles are shown in Figure 4.15. The thickness of $(Cu,Ni)_6Sn_5$ layer increases after twelve reflow cycles. The $(Cu,Ni)_6Sn_5$ layer on Ni film becomes needle-like and chunky type after twelve reflow cycles, as shown in Figure 4.15a. This result corresponds with several researches who have found needle-like $(Cu,Ni)_6Sn_5$ IMC during the reaction with Sn-Ag-Cu solder and Ni film (Pang *et al.*, 2004; Ho *et al.*, 2006; Chen *et al.*, 2010).

Two layers forms at the interface between SAC and Ni-W alloy films after twelve reflow cycles, as shown in Figure 4.15 (b-d). An agglomerated chunky type of $(Cu,Ni)_6Sn_5$ layer is observed at Ni-5 at.% W and Ni-11.3 at.% W interface. A bright layer forms below the $(Cu,Ni)_6Sn_5$ layer. A non-uniform and discontinuous $(Cu,Ni)_6Sn_5$ can be seen at Ni-18 at.% W interface after twelve reflow cycles, as shown in Figure 4.15 (d). A slightly thicker bright layer is observed at the interface between SAC and Ni-18 at.% W. The thickness of $(Cu,Ni)_6Sn_5$ layer decreases with increasing of W content in the film. This observation of is similar to the case of first reflow.

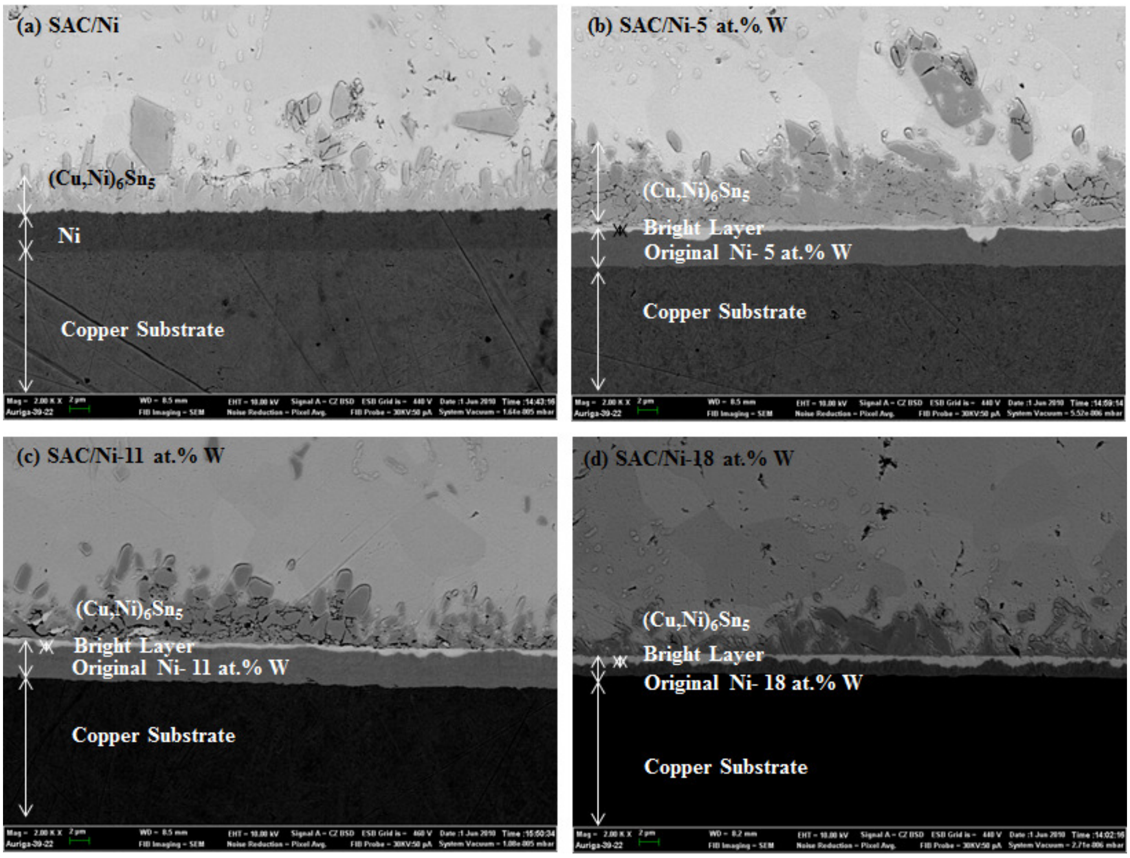

Figure 4.15: Cross sectional back scattered electron images of interface between SAC and barrier films after twelve reflow cycles: a) Ni, b) Ni- 5 at.% W, c) Ni-11.3 at.% W and d) Ni-18.% W.

The thickness of $(Cu,Ni)_6Sn_5$ and bright layers after first and twelve reflow cycles is presented in Figure 4.16. The thicknesses of both $(Cu,Ni)_6Sn_5$ and bright layers show an increasing after twelve reflow cycles. A steady decrease of $(Cu,Ni)_6Sn_5$ layer thickness is observed with the increase of W content in the barrier film. The bright layer, on the other hand, remains insensitive to W content of Ni-W films. This trend is similar to the case obtained between SA solder and barrier films presented in Figure 4.11.

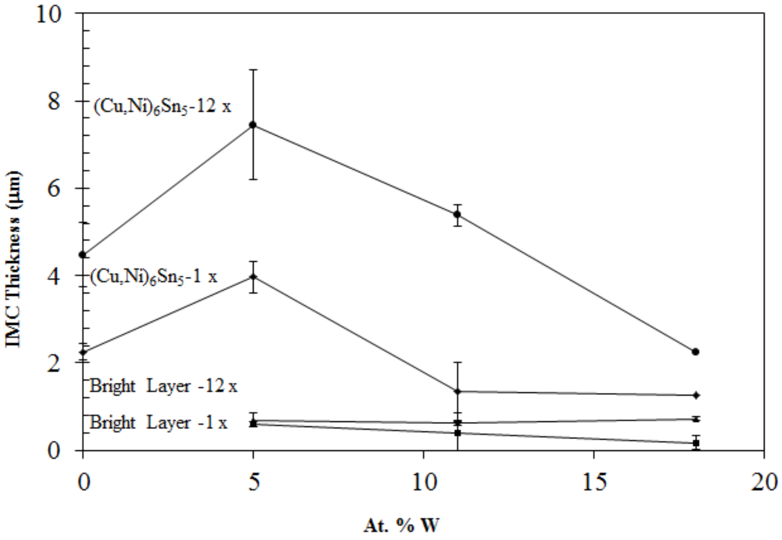

Figure 4.16: The thickness of $(Cu,Ni)_6Sn_5$ IMC and bright layer as a function of tungsten content of Ni-W film for first reflow and twelve reflow cycles.

From the results, $(Cu,Ni)_6Sn_5$ layer thickness decreases in the following order after 12 time reflows: Ni-5 at.% W > Ni-11.3 at.% W > Ni > Ni-18 at.% W. The result shows that incorporated W is significantly impacted the growth of $(Cu,Ni)_6Sn_5$ layer. The higher thickness of $(Cu,Ni)_6Sn_5$ layer observed at Ni-5 at.% W and Ni-11.3 at.% W interface is due to the ease of Ni atoms diffuse out from these films.

It is seen that thinner thickness of $(Cu,Ni)_6Sn_5$ layer forms at Ni interface. It suggests that dissolution of Ni metal in SAC molten forms a thin $(Cu,Ni)_6Sn_5$ layer.

This observation of thin IMC is in agreement with the results obtained by Dybkov (2008) at SA and Ni film.

The lowest thickness of $(Cu,Ni)_6Sn_5$ layer observed on Ni-18 at.% W film is due to decreasing of crystallinity of its film and high W content thought to act as ‘pinning agent’ at the grain boundaries then reduced the growth of $(Cu,Ni)_6Sn_5$ layer. In other words, the W content must be strictly controlled in order to obtain the desired thickness of IMC.

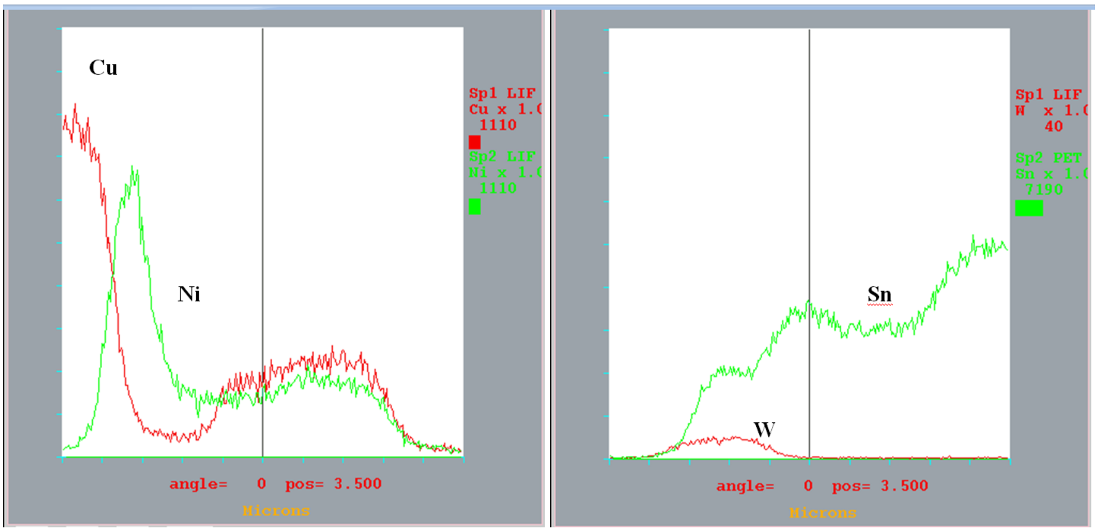

Figure 4.17: EPMA line profiles across the interface of SAC/Ni-11.3 at.% W couple after six reflow cycles.

EPMA line scan recorded across the interface between SAC and Ni-11.3 at.% W after six time reflows is shown in Figure 4.17. From left side, which is copper substrate, copper content is seen to decrease in Ni-W layer and increase in tin matrix. The nickel profile shows a decrease in nickel content at W rich position and a slight increase approaching tin matrix to form $(Cu,Ni)_6Sn_5$. Tin content is seen to increase through Ni-W layer and the highest content in the tin matrix. No tungsten is found in copper substrate and in $(Cu,Ni)_6Sn_5$.

Table 4.6: Composition of bright layer on different Ni-W barrier film after twelve reflow cycles.

Barrier film	Composition of Bright layer, at.%			
	Ni	Cu	W	Sn
Ni-5 at.% W	30.95	18.33	9.60	41.13
Ni-11.3 at.% W	26.31	4.84	23.89	44.97
Ni-18 at.% W	23.06	6.59	24.46	45.89

Table 4.6 shows the average composition of the bright layer that formed after twelve reflow cycles on different Ni-W films. It is seen that tin is the major constituent in the bright layer accounting for about half of its content. The amount of nickel in the bright layer is far smaller compared with the original nickel content of the Ni-W film. Since the quaternary phase contains of Ni, Cu, Sn and W. This new quaternary phase is written as Sn-Cu-Ni-W.

Figure 4.18 shows the EBSD pattern recorded on different phases at the interface between SAC and Ni-5 at.% W after twelve reflow cycles. The channeling pattern taken on $(Cu,Ni)_6Sn_5$ shows well-formed Kikuchi lines representative of a crystalline structure. Channeling pattern coming out of Ni-5 at.% W layer shows Kikuchi line corresponding to a fcc phase. It may be noted that electrodeposited Ni-W alloy with W content used in the study possess the fcc lattice of host nickel (Haseeb, 2008a; Kilmenkov *et al.*, 2009). For Sn-Cu-Ni-W layer, no discernable pattern is visible. This suggests lack of long range order and hence amorphous nature of the Sn-Cu-Ni-W layer (Cadneya *et al.*, 2009). This observation is similar to the case at SA interface.

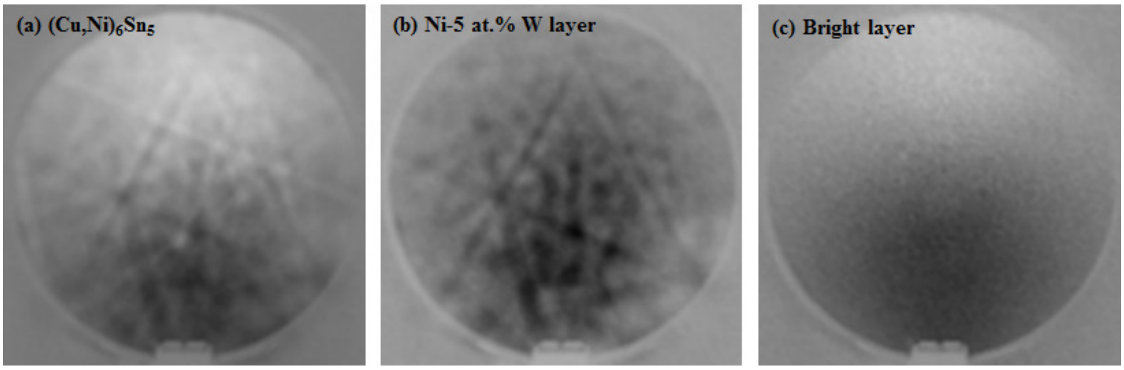

Figure 4.18: EBSD patterns recorded on different phases after 12 reflow cycles a) $(Cu,Ni)_6Sn_5$, b) Ni-5 at.% W layer and c) bright layer.

The above results show that reaction between SAC and Ni-W films produce two layers: $(Cu,Ni)_6Sn_5$ and a bright layer (Sn-Cu-Ni-W). $(Cu,Ni)_6Sn_5$ is a typical IMC that forms when tin reacts with nickel under conditions encountered during soldering. The Sn-Cu-Ni-W is related to the present of Sn, Cu, Ni and W atoms. It is seen that the Sn-Cu-Ni-W layer forms on the outer side (close to solder) of the Ni-W alloy barrier films after reflow. The thinner Sn-Cu-Ni-W layer tends to consume the Ni-W layer after repeated reflow. EPMA (Figure 4.17) further shows that W did not diffuse out to the solder or to the substrate.

The Sn-Cu-Ni-W layer is believed have formed through a similar reaction as that between SA solder and Ni-W alloy films. The anomalously fast diffusion of tin and copper atoms into Ni-W film has contributed to solid state amorphization. The bright layer, Sn-Cu-Ni-W is formed through solid state amorphization. It may be noted that amorphous layer formation was also observed by Chen (2007a) between Sn-0.7Cu and Ni-V barrier film. They found that the bright layer formed when vanadium content of the Sn-Cu solder and Ni-V layer (Chen, 2007a). Analysis showed that this bright layer contains Sn, Cu, Ni and V. They termed this quaternary phase as ‘Q’ phase. As discussed earlier, a similar unknown phase denoted ‘T’ phase has been found between

Sn and Ni-V barrier film. The different between 'Q' and 'T' phase is that the two phases are found in quaternary and ternary systems, respectively. This observation of the quaternary and ternary system is related to the Sn-Ni-W and Sn-Cu-Ni-W layers obtained in this study.

Figure 4.19 shows the schematic drawing of different IMCs formed in SA/Ni-18 at.% W and SAC/Ni-18 at.% W reaction couples. A continuous and compact Ni_3Sn_4 layer formed in SA/Ni-18 at.% W and a ternary layer (Sn-Ni-W) formed below Ni_3Sn_4 (Figure 4.19a). A discontinues $(Cu,Ni)_6Sn_5$ layer formed in SAC/Ni-18 at.% W and a quaternary (Sn-Cu-Ni-W) formed below $(Cu,Ni)_6Sn_5$ layer. The thickness of Ni_3Sn_4 formed between SA and Ni-18 at.% W is (2.55 ± 0.23) µm and Sn-Ni-W IMC layer is (1.82 ± 0.04) µm. However, the thickness of $(Cu,Ni)_6Sn_5$ IMC that formed between SAC and Ni-18 at.% W is (2.25 ± 0.24) µm and Sn-Cu-Ni-W layer is (0.72 ± 0.04) µm.

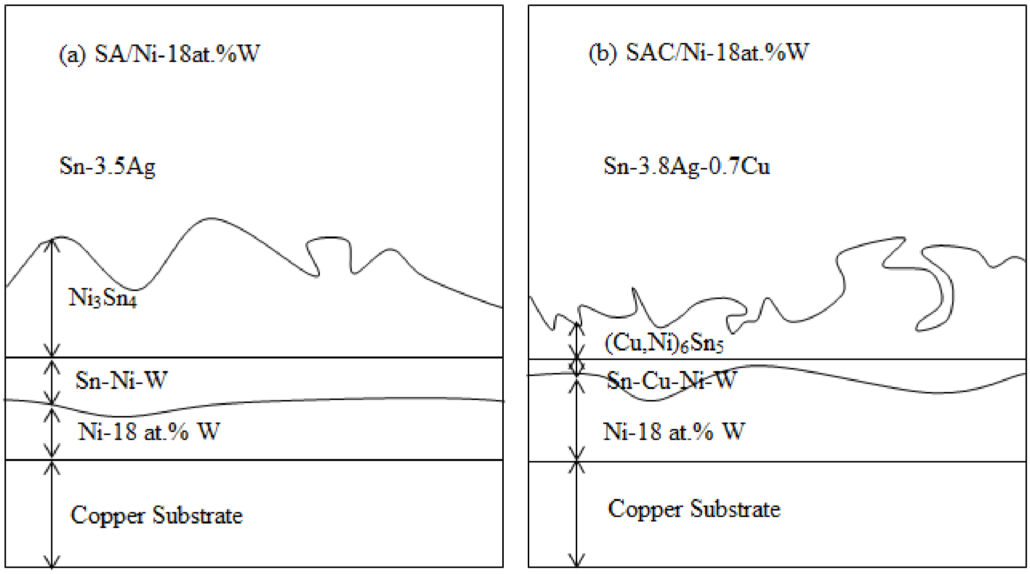

Figure 4.19: Schematic drawing of the interface of (a) SA and Ni-18 at.% , (b) SAC and Ni-18 at.% W.

Lower IMC thickness that was found between SAC and Ni-18 at.% W may be related to the standard Gibbs energies of the formation of $(Cu,Ni)_6Sn_5$ IMC, which is -16 kJ/mol of atoms (Yao *et al.*, 2009). The Gibbs energy of Ni_3Sn_4 IMC is - 24.1 kJ/mol of atoms (Yao *et al.*, 2009). The continuous and larger thickness of IMC is observed at SA interface, because Ni_3Sn_4 phase is easier to form and more stable. While, the discontinuous and slight low thickness of $(Cu,Ni)_6Sn_5$ is observed at SAC interface. The first reason could be lower Gibbs free energies of the formation of $(Cu,Ni)_6Sn_5$ IMC was found and suggests to have less thickness of $(Cu,Ni)_6Sn_5$. Secondly, the lower thickness of $(Cu,Ni)_6Sn_5$ might due to the fast dissolution rate of ternary IMC during liquid and solid reaction. These results are consistent with other researchers who found that $(Cu,Ni)_6Sn_5$ ternary IMC phase has faster dissolution rate during Sn-Ag-Cu molten solder and Ni-V solid metal reaction. Further detailed structural characteristics and properties of the ternary and quaternary phase are necessary to understand the implication on the long term reliability of solder joint.

4.4 Evolution of IMC in SA/Ni and SA/Ni-18 at.% W interfaces during thermal aging

Figure 4.20 reveals the microstructure between SA/Ni and SA/Ni-W alloy interface after high temperature storage at 150°C for 1008 hours (42 days). In Figure 4.20 (a), a continuous and well-faceted intermetallic compound (IMC) was formed between SA solder and Ni film. EDX analysis revealed that the IMC is Ni_3Sn_4, as tabulated in Table 4.7. Two layers are observed between SA and Ni-W alloy films after aging. A uniform and faceted layer formed above a bright layer. EDX results suggest that the faceted layer IMC is Ni_3Sn_4 phase. A bright layer that formed below the Ni_3Sn_4 IMC is continuous and uniform. EDX revealed that the bright layer contained Ni, Sn and W elements. This is similar to IMC that form between SA and Ni-W alloy films after first reflow. Among the three Ni-W alloy films, Ni-18at.% W shows the most interesting results in terms of IMC thickness and another IMC can be seen beneath the bright layer.

Figure 4.21 shows higher magnification of interface between SA and Ni-18 at.% W after aging at 150^{o}C for 1008 hours. It can be seen that another layer formed beneath and along the bright layer. The composition of the new layer is Sn- 30.27 at.% Ni -29.55 at.% W as determined by EDX. The main component belongs to Sn atoms. This new ternary phase is different from the Sn-Ni-W that formed between SA and Ni-18 at.% W after first reflow in terms of structural appearance. FIB imaging was used to further study this layer.

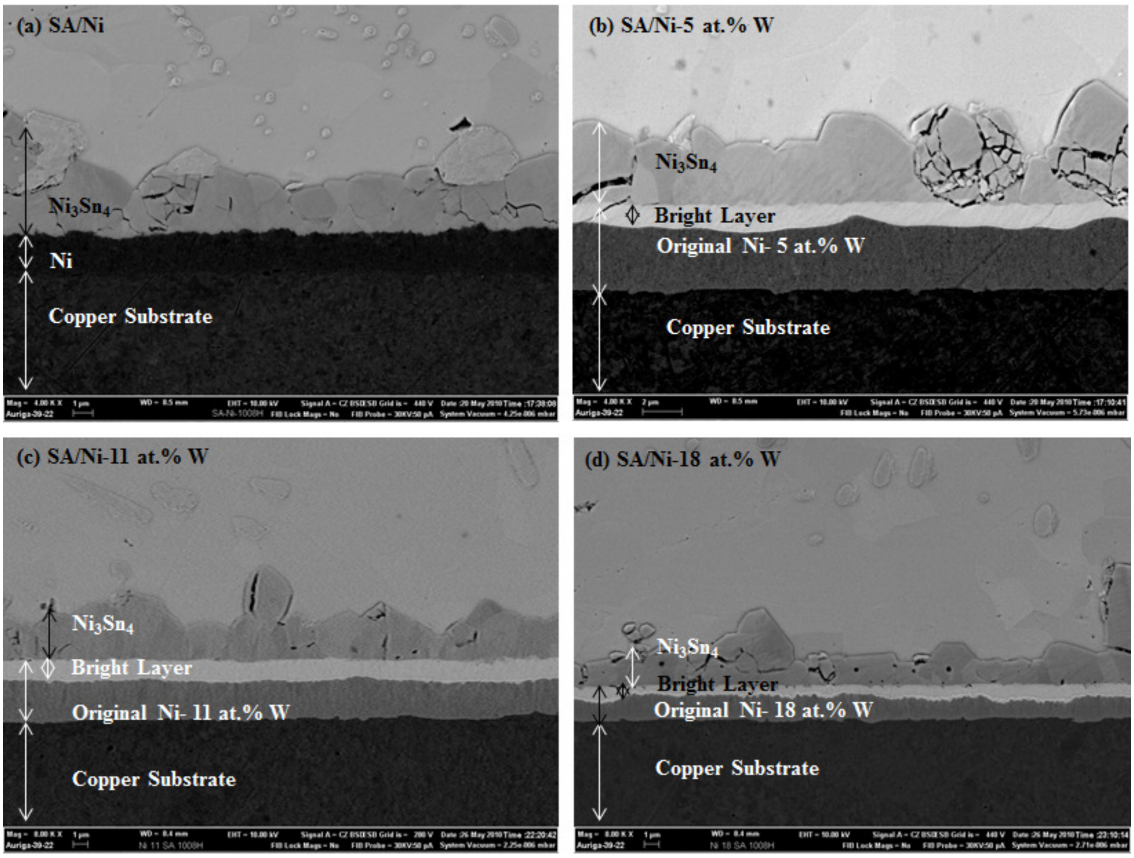

Figure 4.20: Cross sectional back scattered electron images of interface between SA and Ni and Ni-W alloy films after aging at 150^{o}C for 1008 hours: a) Ni, b) Ni- 5 at.% W, c) Ni-11.3 at.% W and d) Ni-18.% W

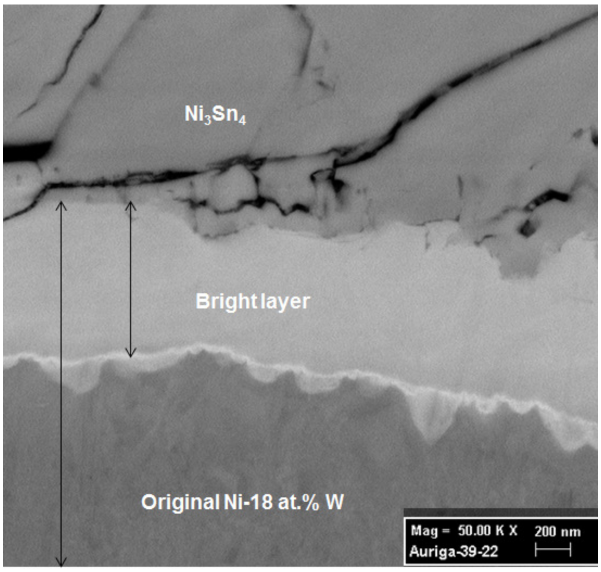

Figure 4.21: Higher magnification FESEM micrograph of interface between SA and Ni- 18 at.% W film after aging at 150°C for 1008 hours.

Table 4.7: Composition of Ni-Sn IMC on different barrier films after aging at 150°C for 1008 hours.

Barrier film	Composition of Ni-Sn, at.%			Identified Phase
	Ni	Sn	Ni/Sn Ratio	
Ni	49.03	50.97	0.96	Ni_3Sn_4
Ni-5 at.% W	48.64	51.36	0.95	Ni_3Sn_4
Ni-11.3 at.% W	48.45	51.55	0.93	Ni_3Sn_4
Ni-18 at.% W	49.01	50.99	0.96	Ni_3Sn_4

Figure 4.22 shows the FIB image across SA and Ni-18 at.% W interface after first reflow and after aging at 150°C for 1008 hours. It can be seen that two layers of IMC formed between SA and Ni-18 at.% W interface after first reflow, as shown in Figure 4.22 (a). An interesting contrast between SA and Ni-18 at.% W after aging at 150°C for 1008 hours can be seen in Figure 4.22 (b). Another new layer is formed towards the Ni-18 at.% W film. Further investigations are needed for better structural determinations of this new layer.

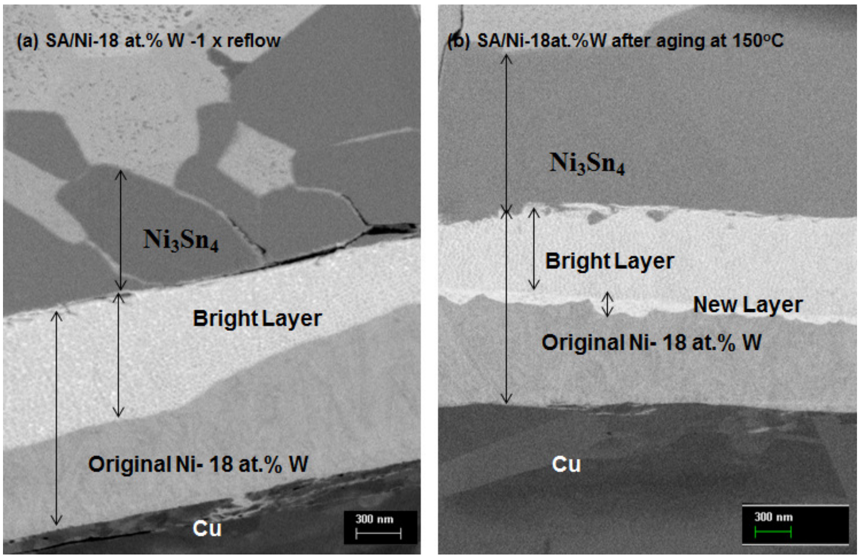

Figure 4.22: FIB image across SA and Ni-18 at.% W interface after first reflow and after aging at 150°C for 1008 hours.

Figure 4.23 shows the thickness of Ni_3Sn_4 at SA/Ni and SA/Ni-W alloy films. As compared to first reflow. The thickness of Ni_3Sn_4 IMC increases after aging at 150°C for 1008 hours. The Ni_3Sn_4 IMC thickness on the interface of SA and Ni-W alloy films is found that grew slower when compared to that on SA/Ni interface.

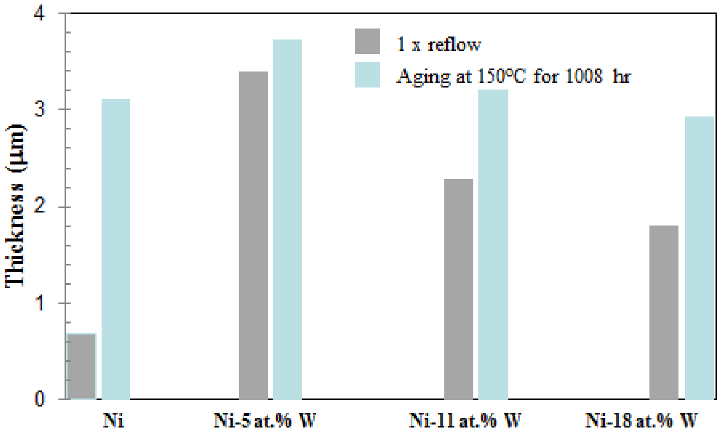

Figure 4.23: Comparison of Ni_3Sn_4 thickness after aging at 150 °C for each barrier layer.

Elemental mapping in Figure 4.24 shows the distribution of Cu, Ni and Sn elements across SA and Ni film. Highest copper content were found in copper substrate and nil in Ni film and solder area. Some Ni atoms diffuse to solder and formed Ni_3Sn_4 with Sn atoms.

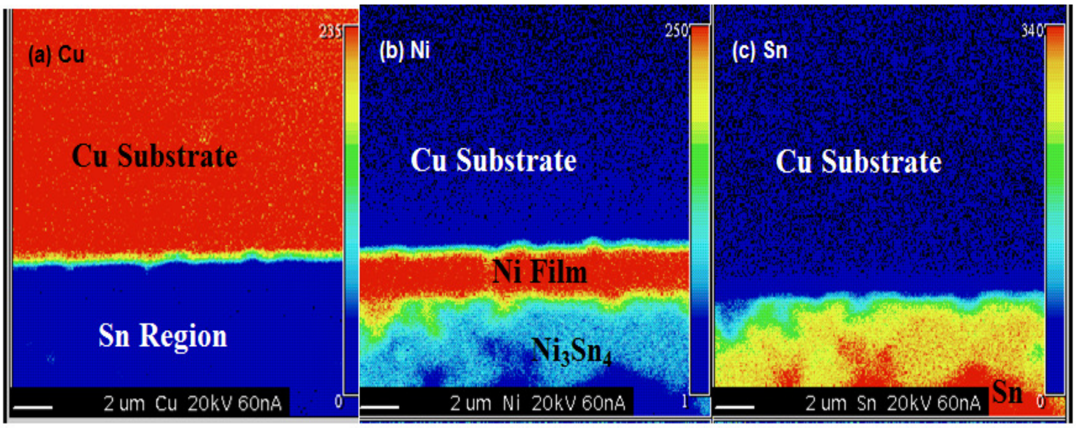

Figure 4.24: Elemental mapping at interface between SA and Ni film after aging at 150°C at 1008 hours: (a) Cu, (b) Ni and (c) Sn by EMPA.

Figure 4.25 shows the EMPA elemental mapping at interface between SA and Ni-18at.% W couple after aging at 150°C at 1008 hours. No copper atoms were found beyond copper substrate. It can be seen that tungsten atoms remain in Ni-W film and no tungsten is found in copper substrate. Nickel content diffused to solder area to form Ni_3Sn_4 IMC.

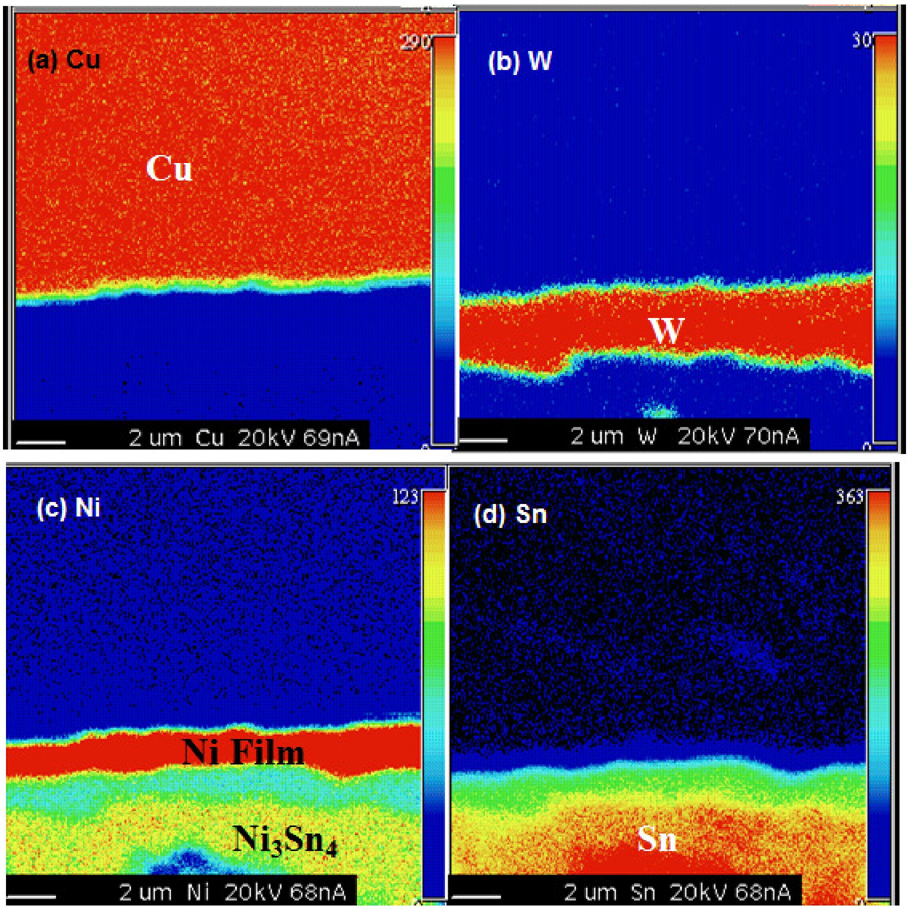

Figure 4.25: Elemental mapping at interface between SA and Ni-18 at.% W barrier film after aging at 150°C for 1008 hours: (a) Cu, (b) W, (c) Ni and (d) Sn by EMPA.

The above results show that reaction between SA and Ni-W film produce two layers: Ni_3Sn_4 and a bright layer after first reflows and after aging at 150°C for1008 hours. The bright layer tends to consume the Ni-18 at.% W layer after high temperature storage. A new layer is observed below the bright layer. EPMA mapping shows that Sn entered into the bright layer, whereas nickel diffused out to form Ni_3Sn_4. EPMA further shows that W did not diffuse out to the solder or to the substrate. Copper atoms do not diffuse out from copper substrate. This observation is quite similar to the case between SA and Ni-W alloy films after multiple reflows.

It is generally believed that the amorphous film can be effective barrier as it exhibits low diffusivity. As-deposited amorphous Ni-P film, however, is unstable and crystallizes during processing. Ni-W and Ni-V films, on the other hand, become amorphous during processing. Such films, therefore, have the potential to provide long term barrier properties.

It has been identified that the interfacial reaction between Ni alloy films and two types of Sn based solders after multiple reflows and high temperature storage. Characterizations of mechanical properties of the IMC that formed at the interface are therefore attracted great interests. The mechanical properties of those IMC will be discussed below.

4.5 Mechanical properties of interfacial layers by nanoindentation

4.5.1 Hardness and elastic modulus across SA and Ni-18 at.% W interface

Figure 4.26 (a) shows AFM topography image of the interface between SA and Ni-18 at. % W. Topographical height across the sample surface is displayed in Figure 4.26 (b). In the copper region, the topographical height remains more or less constant until it reaches the Sn-Ni-W layer. A drop in height is observed in Sn-Ni-W layer; while, a slight rise is seen in Ni_3Sn_4 layer. A sudden fall in height is found in SA solder region. Lower topological height in Sn-Ni-W qualitatively suggests that Sn-Ni-W phase was softer compared with Ni_3Sn_4. During metallographic polishing, Sn-Ni-W layer worn out at a faster rate while led to the formation of a depression at Sn-Ni-W.

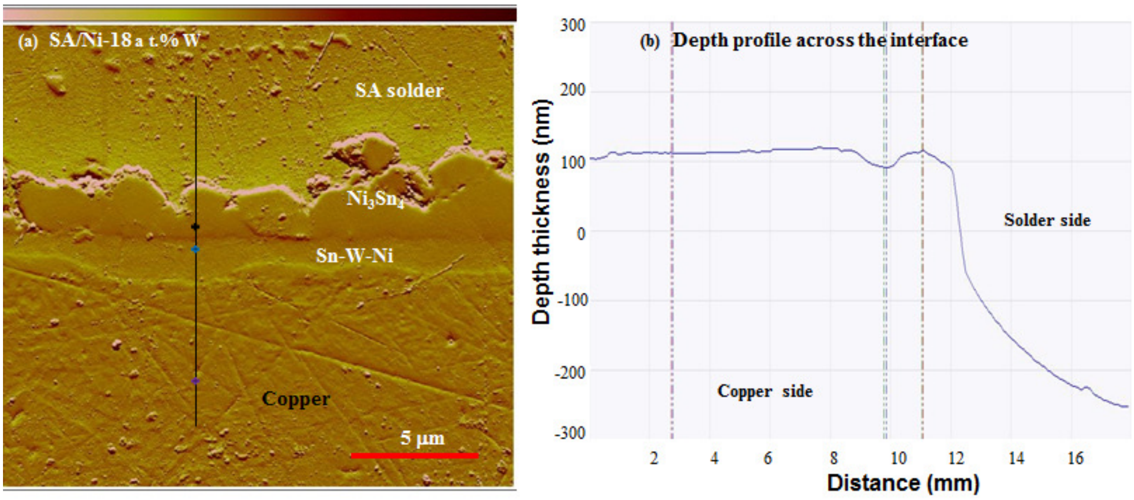

Figure 4.26: (a) AFM topography image at interface between SA and Ni-18 at.% W after six reflow cycles; (b) Depth profile across the interface of IMC as a function of distance across the sample surface.

In order to measure the mechanical properties of the layers at the interfacial region, nanoindentation was performed covering all the interfacial phases. Figure 4.27 shows FESEM micrograph of the indents at interface between SA and Ni-18 at.% W. It can be seen that the indents are the largest at the solder matrix. Much smaller indents are observed on both Ni_3Sn_4 and Sn-Ni-W layers. The indents on the Sn-Ni-W layer appear larger compared with that on Ni_3Sn_4. Table 4.8 shows the hardness (H) and reduced elastic modulus (E) of the phases across the interface. The Ni_3Sn_4 IMC has an average hardness and modulus of 6.79 GPa and 134.24 GPa, respectively.

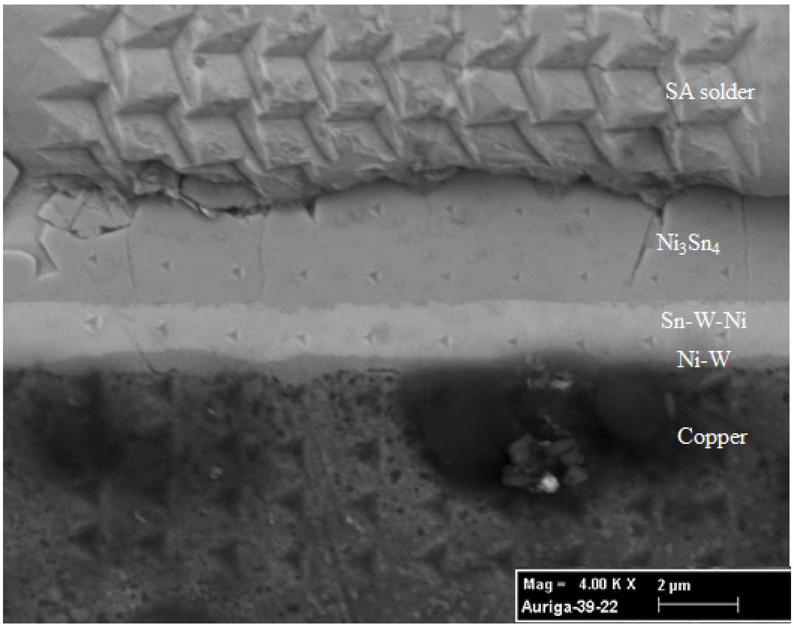

Figure 4.27: SEM image of 100 indents across the interface between SA and Ni-18 at.% W after six reflow cycles.

Table 4.9 composes the literature data on mechanical properties of Ni_3Sn_4. The bright layer, Sn-Ni-W is softer and has a hardness and modulus of H = 4.10 GPa and E = 128.834 GPa, respectively. Hardness of the Sn-Ni-W can be seen slightly higher than copper substrate and lower than that of Ni_3Sn_4. Figure 4.28 shows the ascending order of hardness across SA and Ni-18 at.% W after 100 indents. It can be seen that Ni_3Sn_4 IMC is the highest in hardness.

Table 4.8: Hardness and elastic modulus of intermetallic phases at SA interface after six reflow cycles.

Intermetallic phase	Elastic Modulus (GPa)	Hardness (GPa)
SA	76.29 ± 2.90	0.29 ± 0.02
Ni_3Sn_4	134.24 ± 13.60	6.79 ± 0.60
Sn-Ni-W	128.834 ± 28.68	4.10 ± 1.67
Cu	152.16 ± 11.69	1.70 ± 0.03

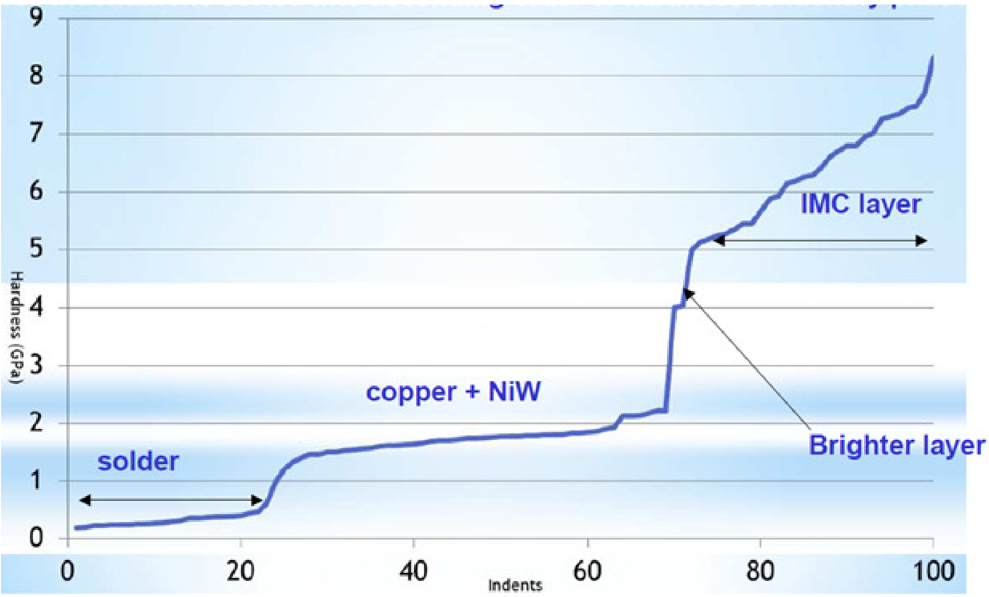

Figure 4.28: 100 indents sorted into ascending order of hardness to identify phases at the interface between SA and Ni-18 at.% W after six reflow cycles.

Table 4.9: Data obtained in literature value the hardness and elastic modulus of Ni_3Sn_4 intermetallic phase.

Intermetallic phase	Hardness (GPa)	Elastic Modulus (GPa)	Reference
Ni_3Sn_4	6.79 ± 0.598	134.24 ± 13.602	Current Study
		133	(Fields *et al.*, 1992)
	4.8	152	(Albrecht *et al.*, 2003)
	8.12 ± 0.62	140.4 ± 7.9	(Jang *et al.*, 2004)
	6.1 to 7.0	119.4 to 134.0	(Chen *et al.*, 2006d)
		152	(Tsai *et al.*, 2006)
		130-150	(Xu, 2006)
	6.31 ± 0.16	141.12 ± 3.85	(Yang *et al.*, 2008)
	6.33		(Yang *et al.*, 2009)

Figure 4.29 displays the 2D maps of (a) hardness and (b) elastic modulus at the interface between SA and Ni-18 at.% W. It is clearly indicated across the SA and copper substrate region showing various hardness and elastic modulus at each intermetallic phase. Some variations of hardness in Ni_3Sn_4 region is observed in Figure 4.29a. According to Marques *et al.* (2009), the different of hardness and elastic modulus in Ni-Sn region related to inherent elastic anisotropy of the Ni_3Sn_4 structure. In elastic modulus map, copper region shows the highest elastic modulus.

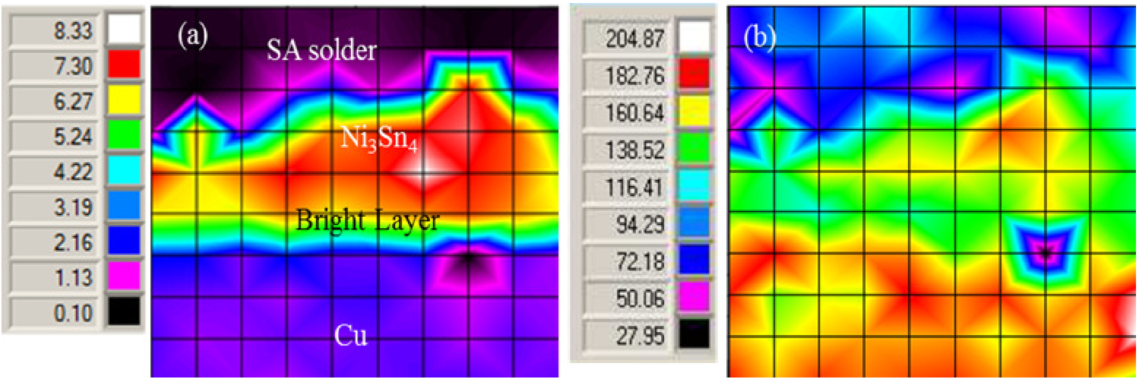

Figure 4.29: The region of (a) hardness and (b) elastic modulus into 2D maps at SA interface after six reflow cycles.

From the above results, it can be seen that Ni_3Sn_4 is harder than Sn-Ni-W ternary layer. A slight drop in topographical height indicated that Sn-Ni-W layer is softer than

Ni_3Sn_4 phase. FESEM image further shows smaller indents on Ni_3Sn_4 compared with than on Sn-Ni-W layer. The result of hardness and elastic modulus on Ni_3Sn_4 phase is comparable within the range that reported in literature.

In general, brittle fracture occurs at solder and Ni_3Sn_4 interface for most solder joints on Ni-B and Ni-P films after prolonged aging treatment (Yoon *et al.*, 2010). However in the case on Ni-P film, Ni-Sn-P ternary layer and Ni_3P IMC that formed at the interface is also associated to the brittle failure (Alam, 2003; Liu *et al.*, 2008b). Liu *et al.* (2008b) indicated that the hardness on Ni-Sn-P and Ni_3P IMC is 11.6 GPa and 12.1 GPa, respectively. They found that Ni_3P IMC and Ni-Sn-P have a greater tendency to encounter the brittle fracture compared with other constitutional phases (Liu *et al.*, 2008b).

In the present case, a bright layer Sn-Ni-W that observed below the Ni_3Sn_4 phase possesses lower hardness than Ni_3Sn_4. The hardness of Sn-Ni-W is found to be 4.10 GPa, which is almost one third of hardness on Ni-Sn-P. It is thus believed that Sn-Ni-W is less sensitive to brittle fracture compared with Ni-Sn-P. This phenomenon is closely related to the formation of Sn-Ni-W. Previous studies suggested that the bright layer, Sn-Ni-W is amorphous structure. It has formed through solid state amorphization caused by anomalously fast diffusion of tins atoms into Ni-W film.

The present experimental results also show that the hardness of Sn-Ni-W is lower that Ni_3Sn_4 IMC and Ni-Sn-P layer. It may be noted that Ni-Sn-P is a nanocrystalline layer (Kim, 2010). The hardness on Sn-Ni-W is related to the amorphous structure. Generally, nanocrystalline layer has higher hardness that amorphous layer (Cavaleiro, 2002). The lower hardness on amorphous Sn-Ni-W is suggested to possess lower tendency to encounter the brittle fracture.

4.5.2 Hardness and elastic modulus at interface between SAC and Ni-18 at.% W

Figure 4.30 (a) shows AFM topography image of the interface between SAC and Ni-18 at.% W. Topographical height across the sample surface is displayed in Figure 4.30 (b). In the copper region, topographical height does not change much and remain constant until it reaches Ni-18 at.%. A slight rise of height is observed in Ni-18 at.% W. A drop in height is then observed in Sn-Cu-Ni-W layer; while, slightly rise in height is seen in $(Cu,Ni)_6Sn_5$ phase. A sudden fall in height is found in SAC solder region. Lower topographical height in Sn-Cu-Ni-W qualitatively suggests that Sn-Cu-Ni-W layer is softer compared with $(Cu,Ni)_6Sn_5$. During metallographic polishing, Sn-Cu-Ni-W worn out at a faster rate while led to the formation of a depression at Sn-Ni-W-Cu.

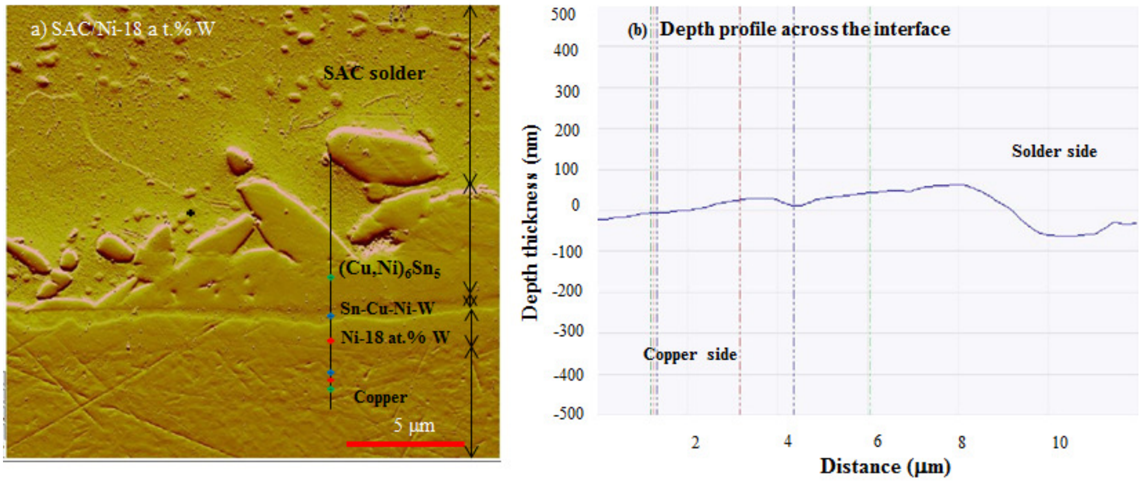

Figure 4.30: (a) AFM topography image at interface between SAC and Ni-18 at.% W after six reflow cycles; (b) Depth profile across the interface of IMC as a function of distance across the sample surface.

The 100 indents were performed across SAC and Ni-18 at.% W in order to measure the mechanical properties and the results are listed in Table 4.10. The $(Cu,Ni)_6Sn_5$ shows an average of hardness and modulus of 7.03 GPa and 161.98 GPa, respectively.

Table 4.10: Hardness and elastic modulus of intermetallic phases at SAC interface after six reflow cycles.

Intermetallic phase	Elastic Modulus (GPa)	Hardness (GPa)
SAC	85.13 ± 4.67	0.57 ± 0.38
$(Cu,Ni)_6Sn_5$	161.98 ± 28.9	7.03 ± 1.18
Ni-W	166.37 ± 53.8	2.23 ± 0.40
Cu	143.82 ± 45.0	1.97 ± 0.11

Table 4.11 displays the literature data of $(Cu,Ni)_6Sn_5$. The Ni-W layer is softer and has an average hardness and modulus of 2.23 GPa and 166.37 GPa, respectively. Hardness of the Ni-W can be seen slightly higher than copper substrate. The $(Cu,Ni)_6Sn_5$ phase has an average hardness and modulus of 7.03 GPa and 162 GPa, respectively.

Table 4.11: Literature value of the hardness and elastic modulus of $(Cu,Ni)_6Sn_5$ intermetallic phase.

Intermetallic phase	Hardness (GPa)	Elastic Modulus (GPa)	Reference
$(Cu,Ni)_6Sn_5$	7.03 ± 1.18	161.98 ± 28.9	Current Study
	-	164.9 to 206.8	(Xu, 2006)
	7.2 ± 0.4	157.8 ± 5.7	(Liu *et al.*, 2008)
	7.31 to 10.07	145.8 to 206.8	(Yang *et al.*, 2008)
	7.77 to 8.21	131.58 to 133.80	(Tsukamoto *et al.*, 2009)

Figure 4.31 displays the 2D maps at SAC solder substrate interface of (a) hardness and (b) elastic modulus. It is clearly indicated that across the SAC and copper substrate region show various hardness and elastic modulus at each intermetallic phase. The

hardness of each layer decreased in the following order: $(Cu,Ni)_6Sn_5$ phase > Sn-Cu-Ni-W layer > Ni-W > Cu substrate > SAC solder.

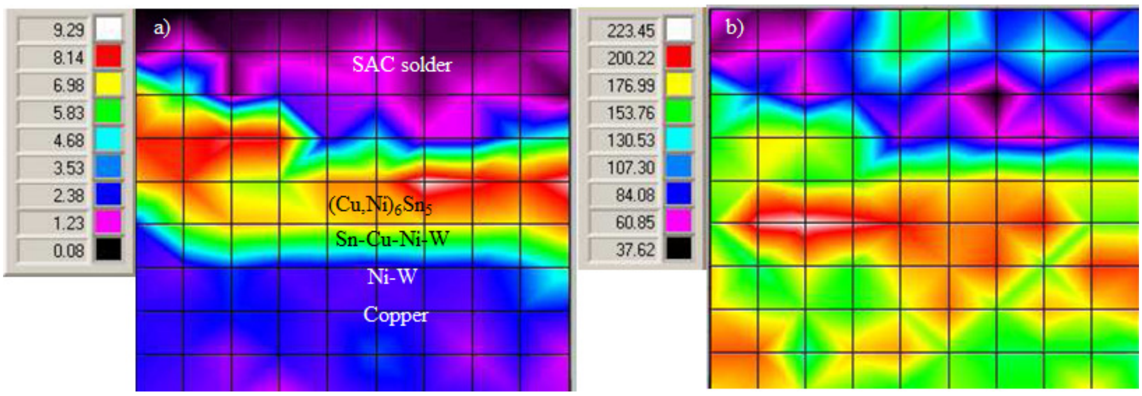

Figure 4.31: The region of (a) hardness and (b) elastic modulus into 2D maps at SAC interface.

The lower hardness observed at Sn-Cu-Ni-W layer from the 2D maps at SAC interface is related to the structure of Sn-Cu-Ni-W layer. As discussed earlier, Sn-Cu-Ni-W is an amorphous structure and has formed through solid state amorphization. This observation is similar to the Sn-Ni-W layer at SA interface. It is clearly indicated across the SAC and copper substrate region showing various hardness and elastic modulus at each intermetallic phase. The hardness of each layer decreased in the following order: $(Cu,Ni)_6Sn_5$ phase > Sn-Cu-Ni-W phase > Ni-W > Cu substrate > SAC solder.

CHAPTER 5: CONCLUSION AND RECOMMENDATIONS

5.1 Conclusion

The following conclusion can be drawn from the above results:

- Ni-W alloy films with tungsten content in the range of 5.0 - 18.0 at.% are successfully prepared on copper substrate by electrodeposition in ammonia-citrate bath.
- The spreading rate decreases with increasing of W content in Ni-W alloy films for both Sn-3.5Ag (SA) and Sn-3.8Ag-0.7Cu (SAC) solders.
- During reflow, two types of interfacial reaction layers formed at the interface between SA and Ni-W alloy films: (i) a Ni_3Sn_4 layer with faceted morphology formed on the solder side, and (ii) a ternary Sn-Ni-W layer formed below the Ni_3Sn_4 layer.
- The thickness of the Ni_3Sn_4 layer is found to decrease with the increase of W content in the Ni-W film. The Sn-Ni-W layer remains insensitive to W content in the barrier film.
- The ternary Sn-Ni-W layer contains tin as its major constituent ($\approx$ 50 at.%) and is found to be amorphous in nature. It is suggested that solid state amorphization caused by anomalously fast diffusion of Sn into Ni-W led to the formation of the amorphous Sn-Ni-W layer.
- During reflow, two types of interfacial reaction layers formed at the interface between SAC and Ni-W alloy films: (i) a non-uniform $(Cu,Ni)_6Sn_5$ layer formed on the solder side, and (ii) a quaternary Sn-Cu-Ni-W layer formed below the $(Cu,Ni)_6Sn_5$ layer.

- The thickness of the $(Cu,Ni)_6Sn_5$ layer is found to decrease with the increase of W content in the Ni-W film. The Sn-Cu-Ni-W layer remains insensitive to W content in the barrier film.
- The quaternary Sn-Cu-Ni-W layer is found to be amorphous in nature. It is suggested that solid state amorphization caused by anomalously fast diffusion of Sn and Cu into Ni-W led to the formation of the amorphous Sn-Cu-Ni-W layer.
- The hardness of each phase obtained by nanoindentation testing decreases in the following order: $(Cu,Ni)_6Sn_5$ phase > Ni_3Sn_4 phase > Sn-Ni-W ternary phase > Ni-18 at.% W > copper substrate > SAC solder > SA solder.

5.2 Recommendations

The following investigations are suggested for future studies:

- It is interesting to electroplate the Ni-W alloy films on BGA dummy substrate and study the reaction between standard ball size solder and Ni-W substrate. This process is more similar to current industries practice.
- Some samples can be subjected to the thermal cycling test. This will provide data more relevant to reliability of the joints.
- The thickness of Ni-W alloy films needs to control precisely in order to calculate the rate loss of Ni atoms in the Ni-W alloy films.
- Transmission electron microscopy (TEM) is suggested to be carried out at the ternary and quaternary layers (these are the layers that found in this study) in order to obtain more quantitative results of theirs structure.
- Besides drop test, ball pull and ball shear test are suggested for further study to determine the strength at the interface and the reliability of the solder joints.

REFERENCES

Abtew, M., & Selvaduray, G. (2000). Lead free solders in microelectronics. *Journal of Materials Science and Engineering, 27*(5), 95-141.

Alam, M. O., Chan, Y. C., & Hung, K. (2002). Interfacial reaction of Pb-Sn solder and Sn-Ag solder with electroless Ni deposit during reflow. *Journal of Electronic Materials., 31*(10), 1117-1121.

Alam, M. O., & Chan, Y. C. (2003). Effect of reaction time and P content on mechanical strength of the interface formed between eutectic Sn-Ag solder and Au/electroless Ni(P)/Cu bond pad. *Journal of Applied Physics*, *94*(6), 4108-4115.

Albrecht, H. J., Juritza, A., M¨uller, K., M¨uller, W. H., Sterthaus, J., Villain, J., & Vogliano, A. (2003). *Interface reactions in microelectronic solder joints and associated intermetallic compounds: an investigation of their mechanical properties using nanoindentation.* Paper presented at the 5th Electronics Packaging Technology Conference, Singapore.

Anhock, S., Ostamann, A., Oppermann, H., Aschenbrenner, R., & Reichl, H. (1996). *Reliability of electroless nickel for high temperature application.* Paper presented at the International Symposium on Advanced Packaging Materials.

Babaghorbani, P., & Gupta, M. (2008). Enhancing the mechanical response of a lead-free solder using an energy-efficient microwave sintering route. *Journal of Electronic Materials*, *37*(6), 860-866.

Benedictus, R., Traeholt, C., Bottger, A., & Mittemeijer. (1999). Solid state amorphization in the Co-Ti system. *Thin Solid Films*, *345* 319-329.

Brenner, A. (1963). *Electrodeposition of Alloys*. New York: Academic.

Cadneya, S., Goodalla, G., Kimb, G., Moranc, A., & Brochua, M. (2009). The transformation of an Al-based crystalline electrode material to an amorphous deposit via the electrospark welding process. *Journal of Alloys and Compounds*, *476*, 147–151.

Cavaleiro, A., & Louro, C. (2002). Nanocrystalline structure and hardness of thin films. *Surface Engineering, Surface Instrumentation and Vacuum Technology, 64*, 211-218.

Chang, S. C., Lin, S. C., & Hsieh, K. C. (2007). Phase reaction in Sn-9Zn solder with Ni/Au surface finish bond-pad at 175^{o}C ageing. *Journal of Alloys and Compounds*, *428*, 179-184.

Chen, C. C., & Chen, S. W. (2006a). The Sn/Ni-7wt.% V Interfacial Reactions. *Journal of Electronic Materials*, *35*(9), 1701-1707.

Chen, C. C., Chen, S. W., & Kao, C. Y. (2006b). Interfacial reactions in the Sn-(Ag)/(Ni,V) couples and phase equilibria of the Sn-Ni-V system at the Sn-Rich corner. *Journal of Electronic Materials*, *35*(512), 922-928.

Chen, K., Liu, C., Whalley, D. C., & Hutt, D. A. (2006c). *Electroless Ni-W-P Alloys as Barrier Coatings for Liquid Solder Interconnects.* Paper presented at the Electronics Systemintegration Technology Conference, Dresden, Germany.

Chen, S. W., & Chen, C. C. (2007a). Interfacial reations in Sn-0.7wt.% Cu/Ni-V couples at 250°C. *Journal of Electronic Materials*, *36*(9), 1121-1128.

Chen, S. W., Chen, C. C., & Chang, C. H. (2007b). Interfacial reactions in Sn/Ni–7 wt.%V Couple. *Journal of Scripta Materialia*, *56*, 453-456.

Chen, W. M., Yang, S. C., Tsai, M. H., & Kao, C. R. (2010). Uncovering the driving force for massive spalling in the Sn-Cu/Ni system. *Scripta Materialia*, *63*, 47-49.

Chen, Z., He, M., Balakrisnan, B., & Chum, C. C. (2006c). Elasticity modulus, hardness and fracture toughness of Ni_3Sn_4 intermetallic thin films. *Materials Science and Engineering A*, *423*, 107-110.

Choi, P., Al-Kassab, T., Gartner, F., Kreye, H., & Kirchheim, R. (2003). Thermal stability of nanocrystalline nickel-18 at.% W alloy investigated with the tomographic atom probe. *Journal of Materials Science Engineering A*, *353*, 74-79.

Choi, J. W., Hwang, G. H., Han, W. K., & Kang, S. G. (2006). Phase transformation of Ni-B, Ni-P diffusion barrier deposited electrolessly on Cu interconnect. *Applied Surface Science*, *253*, 2171-2178.

Data from FSlite, *FactSage light metal alloy database*. Retrieved 23 June 2010, from http://www.crct.polymtl.ca/fact/documentation/FSlite/Ni-W.jpg.

Detor, A. J., Michael K, M., & Schuh, C. A. (2006). *Solute Distribution in Nanocrystalline Ni-W Alloys*. Paper presented at the IEEE.

Dubin, V. M., Yosi, S., Zhao, B., Vasudev, P. K., & Ting, C. H. (1997).

Dybkov, V. I. (2008). Effect of Dissolution on the Ni_3Sn_4 growth kinetics at the interface of Ni and liquid Sn-Base solders. *Solid State Phenomeno*, *138*, 153-158.

Einati, H., Bogush, V., Sverdlov, Y., Rosenberg, Y., & Diamand, Y. S. (2005). The effect of tungsten and boron on the Cu barrier and oxidation properties of thin electroless cobalt-tungsten-boron films. *Microelectronic Engineering*, *82*(3-4), 623-628.

Erinc, M., Schreurs, P. J. G., & Geers, M. G. D. (2007). Integrated numerical-experimental analysis of interfacial fatigue fracture in SnAgCu solder joints. *International Journal of Solids and Structures*, *44*(17), 5680-5694.

Fields, R. J., Low, S. R., & Lucey, G. K. (1992). The metal science of joining. *The Minerals, Metals & Materials Society, Warrendale (PA)*, 165-173.

Guo, F., Choi, S., Lucas, J. P., & Subramanian, K. N. (2000). Effects of reflow on wettability, microstructure and mechanical properties in lead-free solders. *Journal of Electronic Materials*, *29*(10), 1241-1248.

Gur, D., & Bamberger, M. (1998). Reactive isothermal solidification in the Ni-Sn system *Acta Materialia*, *46*(14), 4917-4923.

Handwerker, C., Kattner, U., & Moon, K.-W. (Eds.). (2007). *Fundamental properties of Pb-free solder alloys*. USA: Springer.

Harada, M., Satoh, R., Yamada, O., Yabushita, A., Itoh, M., Netsu, T., & Terouchi, T. (1997). *A New Ni-W Thin Film Metallization for Solder Interconnections and Design Method of Metallization Thickness.* Paper presented at the 47th Electronic Components and Technology Conference.

Haseeb, A. S. M. A., Albers, U., & Bade, K. (2007). Friction and wear characteristics of electrodeposited nanocrystalline nickel-tungsten alloy films. *Wear*, *264*, 106-112.

Haseeb, A. S. M. A., & Bade, K. (2008a). LIGA Fabrication of nanocrystalline Ni-W alloy micro specimens from ammonia-citrate bath. *Microsyst Technol, 14*, 379-388.

Haseeb, A. S. M. A., & Bade, K. (2008b). *Structure and Hardness Evolution in Nanocrystalline LIGA Fabricated Ni-12at%W Alloy at 873 K.* Paper presented at the Nanomaterials -- Fabrication, Properties, and Applications, The Mineral, Metals and Materials Society (TMS), New Orleans, LA, USA.

He, M., Chen, Z., & Qi, G. (2004a). Solid state interfacial reaction of Sn-37Pb and Sn-3.5Ag solders with Ni-P under bump metallization. *Acta Materialia*, *52*, 2047-2056.

He, M., Lau, W. H., Gi, G. J., & Chen, Z. (2004b). Intermetallic compounds formation between Sn-3.5Ag solder and Ni-based metallization during liquid state reaction. . *Thin Solid Films*, *462-463*, 376-383.

Ho, C. H., Yang, S. C., & Kao, C. R. (2006). Interfacial reaction issues for lead-free electrronic solders. *Journal of Materials Science: Materials in Electronics*, *18*, 155-174.

Hsu, H. f., & Chen, S. W. (2004). Phase equilibria of the Sn-Ag-Ni ternary system and interfacial reactions at the Sn-Ag/Ni joints. *Acta Materialia*, *52*, 2541–2547.

Huang, M. L., & Wang, L. (2005). Effects of Cu, Bi and In on microstructure and tensile properties of Sn-Ag-X (Cu, Bi, In) solders. *Journal of Metallurgical and Materials Transactions A*, *36*(6), 1439-1446.

Huanga, H., Winchesterb, K. J., Suvorovac, A., Lawne, B. R., Liud, Y., Hud, X. Z., . . . Faraoneb, L. (2006). Effect of deposition conditions on mechanical properties of low-temperature PECVD silicon nitride films *Materials Science and Engineering A*, *435-436*, 453-459.

Huh, J. Y., & Moon, S. J. (2000). Effect of elastic stresses on solid state amorphization of Zr/Co multilayers. *Thin Solid Films*, *377-378*, 611-616.

Islam, M. N., Chan, Y. C., Rizvi, M. J., & Jillek, W. (2005). Investigations of interfacial reactions of Sn-Zn based and Sn-Ag-Cu lead-free solder alloys as replacement for Sn-Pb solder. *Journal of Alloys and Compounds*, *400*, 136-144.

Jang, J. W., Kim, P. G., Tu, K. N., Frear, D. R., & Thompson, P. (1999). Solder reaction-assisted crystallization of electroless Ni-P under bump metallization in low-cost flip-chip technology. *Journal of Applied Physics*, *85*(12), 8456-8463.

Jang, S.-Y., Wolf, J., Kwon, W. S., & Paik, K. W. (2002). *UBM (Under Bump Metallization) study for Pb-free electroplating bumping: interface reaction and electromigration*. Paper presented at the 2002 Electronic Components and Technology Conference, IEEE.

Jang, S. Y., Wolf, J., Ehrmann, O., Gloor, H., Schreiber, T., Reichl, H., & Paik, K. W. (2003). *CrCu based UBM (Under Bump Metallization) study with electroplated Pb/63Sn solder bumps - interfacial reaction and bump shear strength*. Paper presented at the IEEE Transactions on Components and Packaging Technologies.

Jang, G. Y., Lee, J. W., & Duh, J. G. (2004). The nanoindentation characteristics of Cu_6Sn_5, Cu_3Sn, and Ni_3Sn_4 intermetallic compounds in the solder bump. *Journal of Electronic Materials*, *33*(10), 1103-1110.

Kilmenkov, M., Haseeb, A. S. M. A., & Bade, K. (2009). Structural investigations on nanocrystalline Ni-W alloy films by trasmission electron microscopy. *Thin Solid Films*, *517*, 6593-6598.

Kim, D., & Pak, J. J. (2010). Micro void growth in NiSnP layer between $(Cu,Ni)_6Sn_5$ intermetallic compound and Ni_3P by higher reflow temperature and multiple reflow. *Journal of Materials Science: Materials in Electronics*, *21*(12), 1337-1345.

Kripesh, V., Teo, P. S., Chong, C. T., & Vishwanadam, G. (2001). *Development of a lead free chip scale package for wireless applications*. Paper presented at the Proceedings of the 51st Electronic Components and Technology Conference 2001.

Kumar, A., He, M., & Chen, Z. (2005). Barrier properties of thin Au/Ni-P under bump metallization for Sn-3.5Ag solder. *Journal of surface & Coatings Technology*, *198*, 283-286.

Lai, W. S., & Liu, B. X. (1999). Solid-state amorphization of Ni/Zr bilayer through diffusion-limited-reaction observed by molecular-dynamics simulation. *Computational Materials Science*, *14*, 163-168.

Lau, J. H., Wong, C. P., Lee, N. C., & Lee, R. S. W. (Eds.). (2003). *Electronics manufacturing with lead-free, halogen-free, and conductive adhesive materials*. New York: McGraw-Hill.

Lee, C. B., Yoon, J. W., Suh, S. J., & Jung, S. B. (2003). Intermetallic compounds layer formation between Sn-3.5Ag BGA solder ball and (Cu, immersion Au/electroless Ni-P/Cu) substrate. *Journal of Materials Science: Materials in Electronics*, *14*, 487-493.

Lee, C. H., Tai, K. L., Bacon, D. D., Doherty, C., Katz, A., Wong, Y. M., & Lane, E. (1994). Bonding of InP laser diodes by Au-Sn solder and tungsten-based barrier metallization Schemes *Semiconductor Science and Technology*, *9*(4), 379-386.

Li, J. F., Mannan, S. H., & Clode, M. P. (2006). Lifetime of solid metals in contact with liquid solders for high temperature liquid solder assemblies. *Scripta Materialia*, *54*, 1773-1778.

Liang, M. W., Yen, H. T., & Hsieh, T. E. (2006). Investigation of electroless cobalt-phosphorous layer and its diffusion barrier properties of Pb-Sn solder. *Journal of Electronic Materials*, *35*(7), 1593-1599.

Lin, Y. C., & Duh, J. G. (2006). Optimal phosphorous content selection for the soldering reaction of Ni-P bump metallization with Sn-Ag-Cu solder. *Journal of Electronic Materials*, *35*(8), 1665-1671.

Liu, P., Yao, P., & Liu, J. (2008a). Effect of SiC nanoparticle additions on microstructure and microhardness of Sn-Ag-Cu solder alloy. *Journal of Electronic Materials*, *37*(6), 874-879.

Liu, Y. R., Song, J.-M., Lai, Y. S., Chiu, Y. T., & Chen, W. T. (2008b). *Effect of transition metals on the interfacial reactions in electroless Ni(P)-solder interconnections*. Paper presented at the Electronic Materials and Packaging, EMAP, Taipei.

Luo, Q. and Xiao, J. (2006, October 9-15). *Haptic Simulation for Micro/Nano-Scale Optical Fiber Assembly.* Paper presented at the International Conference on Intelligent Robots and Systems, Beijing, China.

Magagnin, L., Sirtori, V., Seregni, S., Origo, A., & Cavallotti, P. L. (2005). Electroless cobalt-phosphorous for diffusion barrier properties in Pb-free soldering. *Journal of Electrochimica Acta*, *50*, 4621-4625.

Mannan, S. H., & Clode, M. P. (2004). Materials and processes for implementing high-temperature liquid interconnects. *Journal of Advanced Packaging, IEEE 27*(3), 508-514.

Mannan, S. H., Clode, M. P., & M. Dagher. (2005). Study of intermetallic crystal growth between Nb and molten 52In-48Sn solder. *Journal of Electronic Materials*, *34*(2), 125-131.

Marques, V., Johnston, C., & Grant, P. S. (2009). Two-dimensional mapping of the mechanical properties of Pb-free solder for reliability optimisation. *Journal of Microelectronic & Electronics Packaging*, *6*, 182-185.

Oliver, W. C., & Pharr, G. M. (1992). An improved technique for determining hardness and elastic modulus using load and displacement sensing indentation experiments. *Journal of Materials Research*, *7*(6), 1564-1583.

Pandher, R. (2006). *Reflow Profile Optimization for Lead-free (SAC) Alloys in BGA Applications*. Paper presented at the Electronics Packaging Technology Conference.

Pang, J. H. L., Xu, L. H., Shi, X. Q., Zhou, W., & Ngoh, S. L. (2004). Intermetallic growth studies on Sn-Ag-Cu lead free solder joints. *Journal of Electronic Materials*, *33*(10), 1219-1226.

Predel, B. *Copper-Tungsten. The Landolt-Börnstein Database*. Retrieved 23 June 2010, from http://www.springermaterials.com/docs/info/10086090_1131.html.

Schward, R. B., & Johnson, W. L. (1983). Formation of an amorphous alloy by solid-state reaction of the pure polycrystalline metals. *Physical Review Letters*, *51*(5), 415-418.

Sharif, A., Chan, Y. C., & Islam, R. A. (2004a). Effect of volume in interfacial reaction between eutectic Sn-Pb solder and Cu metallization in microelectronic packaging. *Journal of Materials Science and Engineering B*, *106*, 120-125.

Sharif, A., Islam, M. N., & Chan, Y. C. (2004b). Interfacial reactions of BGA Sn-3.5Ag-0.5Cu and Sn-3.5Ag solders during high temperature aging with Ni/Au metallization. *Journal of Materials Science and Engineering B*, *113*, 184-189.

Sharif, A., & Chan, Y. C. (2005). Interfacial Reactions of Sn-3.5% Ag and Sn-3.5% Ag-0.5% Cu Solder with electroless Ni/Au metallization during multiple reflow cycles. *Journal of Materials Science: Materials in Electronics*, *16*(3), 153-158.

Shen, J., Chan, Y. C., & Liu, S. Y. (2009). Growth mechanism of Ni3Sn4 in a Sn/Ni liquid/solid interfacial reaction. *Acta Materialia*, *57*, 5196-5206.

Shim, J. H., Oh, C. S., Lee, B. J., Lee, D. N. & Metallkde, Z. (1996). *Full thermodynamic assessment*, 87, 205-212. Retrieved 23 June 2010, from http://www.metallurgy.nist.gov/phase/solder/cusn.html.

Small, J. A., Michael, J. R., & Bright, D. S. (2002). Improving the quality of electron backscatter diffraction (EBSD) patterns from nanoparticles. *Journal of Microscopy*, *206*(2), 170-178.

Sohn, Y. C., Yu, J., Kang, S. K., Shih, D. Y., & Choi, W. K. (2004). Effects of phosphorus content on the reaction of electroless Ni-P with Sn and crystallization of Ni-P. *Journal of Electronic Materials*, *33*(7), 790-795.

Suganuma, K. (2001). Advances in lead-free electronics soldering. *Solid State and Materials Science*, *5*(1), 55-64.

Sun, P., Andersson, C., Wei, X., Cheng, Z., Lai, Z., Shangguan, D., & Liu, J. (2006). *High Temperature Aging Study of Intermetallic Compound Formation of Sn-*

3.5Ag and Sn-0.4Ag-0.5Cu Solders on Electroless Ni(P) Metallization. Paper presented at the Electronic Components and Technology Conference.

Sun, P., Andersson, C., Wei, X., Cheng, Z., Shangguan, D., & Liu, J. (2007). Intermetallic compound formation in Sn-Co-Cu, Sn-Ag-Cu and eutectic Sn-Cu solder joints on electroless Ni(P) immersion Au surface finish after reflow soldering. *Journal of Materials Science and Engineering B*, *135*, 134-140.

Tsai, I., Wu, E., Yen, S. F., & Chuang, T. H. (2006). Mechanical properties of intermetallic compounds on lead free solder by Moire techniques. *Journal of Electronic Materials*, *35*(5), 1059-1006.

Tsukamoto, H., Dong, Z., Huang, H., Nishimura, T., & Nogita, K. (2009). Nanoindentation characterization of intermetallic compounds formed between Sn-Cu(-Ni) ball grid arrays and Cu substrates *Materials Science and Engineering: B*, *164*(1), 44-50.

Vuorinen, V., Yu, H., Laurila, T., & Kivilahti, J. K. (2006). Phase formation between lead free Sn-Ag-Cu solder and Ni(P)/Au finishes. *Journal of Applied Physics*, *99*(2), 023530-023531-023530-023536.

Wang, C. H., & Chen, S.W. (2006). Sn-0.7 wt.%Cu/Ni interfacial reactions at 250^{o}C. *Acta Materialia*, *54*, 247-253.

Wang, H., Liu, R., Cheng, F., Cao, Y., Ding, G., & Zhao, X. (2010a). Electrodepositing amorphous Ni-W alloys for MEMS *Microelectronic Engineering*, *87*(10), 1901-1906.

Wang, K.-J., Duh, J.-G., Sykes, B., & Schade, D. (2010b). Impact testing of Sn-3.0Ag-0.5Cu solder with Ti/Ni(V)/Cu under bump metallization after aging at 150 ^{o}C. *Journal of Electronic Materials*, *39*, 2558.

Wu, W. C., Hsieh, T. E., & Pan, H. C. (2008). Investigation of electroless Co(W,P) thin film as the diffusion barrier of underbump metallurgy. *Journal of Electronic Materials*, *155*(5), D369-D376.

Xu, L., & Pang, J. H. L. (2006). Nanoindentation on SnAgCu lead-free solder joints and analysis. *Journal of electronic materials*, *35*(12), 2107-2115.

Yamasaki, T., SchloBmacher, P., Ehrlich, K., & Ogino, Y. (1998). Formation of amorphous electrodeposited Ni-W alloys and their nanocrystallization. *Nanostructured Materials*, *10*(3), 375-388.

Yamasaki, T., Timohira, R., Ogino, Y., Schloßmacher, P., & Ehrlich, K. (2000). Formation of ductile and amorphous nanocrytalline Ni-W alloys by electrodeposition. *Plating Surf Finish*, *87*, 148-152.

Yang, P. F., Lai, Y. S., Jian, S. R., Chen, J., & Chen, R. S. (2008). Nanoindentation indentifications of mechanical properties of Cu_6Sn_5, Cu_3Sn, and Ni_3Sn_4 intermetallic compounds derived by diffusion couples. *Materials Science and Engineering A*, *485*, 305-310.

Yang, P. F., Jian, S. R., Lai, Y. S., & Chen, R. S. (2009). Nanotribological characteristics of Cu_6Sn_5, Cu_3Sn, and Ni_3Sn_4 intermetallic compounds. *Journal of Electronic Materials*, *38*(6), 810-814.

Yao, P., Liu, P., & Liu, J. (2009). Interfacial reaction and shear strength of SnAgCu-xNi/Ni solder joints duting aging at 150°C. *Microelectronic Engineering, 86*(10), 1967-1974.

Yoon, J. W., Koo, J. M., Kim, J. W., Ha, S. S., Noh, B. I., Lee, C. Y., . . . Jung, S. B. (2008). Effect of boron content in electroless Ni-B layer on plating layer properties and soldering characteristics with Sn-Ag solder. *Journal of Alloys and Compounds*, *466*, 73-79.

Yoon, J. W., Noh, B. I., & Jung, S. B. (2010). Mechanical reliability of Sn-Ag BGA solder joints with various electroless Ni-P and Ni-B plating layer. *Journal of IEEE Transactions on Components, Packaging and Manufacturing Technology-Part C*, *33*(1).

Zeng, K., & Tu, K. N. (2002). Six cases of reliability study of Pb-free solder joints in electronic packaging technology. *Materials Science and Engineering R*, *38*, 55-105.

Zhu, M. F., So, F. C. T., & Nicolet, M. A. (1985). Amorphous Ni-N-W Film as a Diffusion Barrier between Aluminum and Silicon. *Thin Solid Films*, *130*(3-4), 245-251.

LIST OF PUBLICATIONS

C. S. Chew, A. S. M. A. Haseeb and M. R. Johan, ‘Wetting behavior of Lead Free Solder on Electroplated Ni and Ni-W Alloy Barrier Film’, International Conference on Electronic Packaging Technology & High Density Packaging (ICEPT-HDP 2009), 10-13 August 2009, Beijing, China, Paper ID: E-036.

C. S. Chew, A. S. M. A. Haseeb and M. R. Johan, ‘Performance of Nanocrystalline Ni-18.0 at.% W Alloy As Barrier Film between Sn-3.8Ag-0.7Cu Solder and Copper Substrate’, 3rd IEEE International Conference on Nanoelectronics, 2010, Hong Kong, China, Paper ID: T-051.

A. S. M. A. Haseeb, **C. S. Chew** and M. R. Johan (2011), Interfacial Reactions between Sn-3.5 Ag Solder and Ni-W Alloy Films.

C. S. Chew, A.S.M.A. Haseeb and B. Beake (2011). Mechanical Properties of Interfacial Phases between Sn-3.5 Ag Solder and Ni- 18 at. % W Barrier Film by Nanoindentation. (In progress).

APPENDIX

Electrodeposition of Ni film

	Total Volume, 600ml
Nickel sulfate 150g/l	200ml = 30 g
Nickel chloride 60g/l	200ml = 12 g
Borid acid 37.5 g/l	200ml = 7.5 g
pH	3.5
Bath temperature	57°C
Stirring condition	Mild stirring (60rpm) with magnetic bath
Current density	20 mA/cm^2
Substrate	30 mm x 60 mm x 0.3 mm Cu sheet

Sample	Exposing Area (cm x cm) I = 360 mA	Deposition Time (min s)
Ni	3.0 x 6.0	15 min

Electrodeposition of Ni-W alloy films

Ni- 5.0 at. % W film

	Total Volume, 1500ml
Nickel sulphate, $NiSO_4.6H_2O$ **(0.33 M)**	300ml = 26.0222 g
Sodium tungstate, $Na_2WO_4.2H_2O$ **(0.01M)**	300ml = 0.9896 g
Sodium citrate, $Na_3C_6H_5O_7.2H_2O$ (0.5 M)	300ml = 44.115 g
Ammonium chloride, NH_4Cl (0.5 M)	300ml = 8.0235 g
Sodium bromide, NaBr (0.15 M)	300ml = 4.63005 g
pH	8.5
Bath temperature	80°C
Stirring condition	Mild stirring (60rpm) with magnetic bath
Current density	10 mA/cm^2
Substrate	60 mm x 60 mm x 0.3 Cu sheet

Sample	Exposing Area (cm x cm) I = 360 mA	Deposition Time (min)
Ni-5.0 at.% W	6.0 x 6.0	30 min

Ni- 11.3 at.% W film

	Total Volume, 1500ml
Nickel sulphate, $NiSO_4.6H_2O$ **(0.22 M)**	300ml = 17.3481 g
Sodium tungstate, $Na_2WO_4.2H_2O$ **(0.07 M)**	300ml = 6.92706 g
Sodium citrate, $Na_3C_6H_5O_7.2H_2O$ (0.5 M)	300ml = 44.115 g
Ammonium chloride, NH_4Cl (0.5 M)	300ml = 8.0235 g
Sodium bromide, NaBr (0.15 M)	300ml = 4.63005 g
pH	8.5
Bath temperature	80°C
Stirring condition	Mild stirring.(60rpm) with magnetic bath
Current density	10 mA/cm^2
Substrate	60 mm x 60 mm x 0.3 Cu sheet

Sample	Exposing Area (cm x cm) *I* = 360 mA	Deposition Time (min)
Ni-11.3 at.% W	6.0 x 6.0	40 min

Ni- 18.0 at.% W film

	Total Volume, 1500ml
Nickel sulphate, $NiSO_4.6H_2O$ **(0.06 M)**	300ml = 4.7313 g
Sodium tungstate, $Na_2WO_4.2H_2O$ **(0.14 M)**	300ml = 13.854 g
Sodium citrate, $Na_3C_6H_5O_7.2H_2O$ (0.5 M)	300ml = 44.115 g
Ammonium chloride, NH_4Cl (0.5 M)	300ml = 8.0235 g
Sodium bromide, NaBr (0.15 M)	300ml = 4.63005 g
pH	8.5
Bath temperature	80 °C
Stirring condition	Mild stirring (60rpm) with magnetic bath
Current density	10 mA/cm^2
Substrate	60 mm x 60 mm x 0.3 Cu sheet

Sample	Exposing Area (cm x cm) *I* = 360 mA	Deposition Time (min)
Ni-18.0 at. % W	6.0 x 6.0	120 min

Figure 4.9

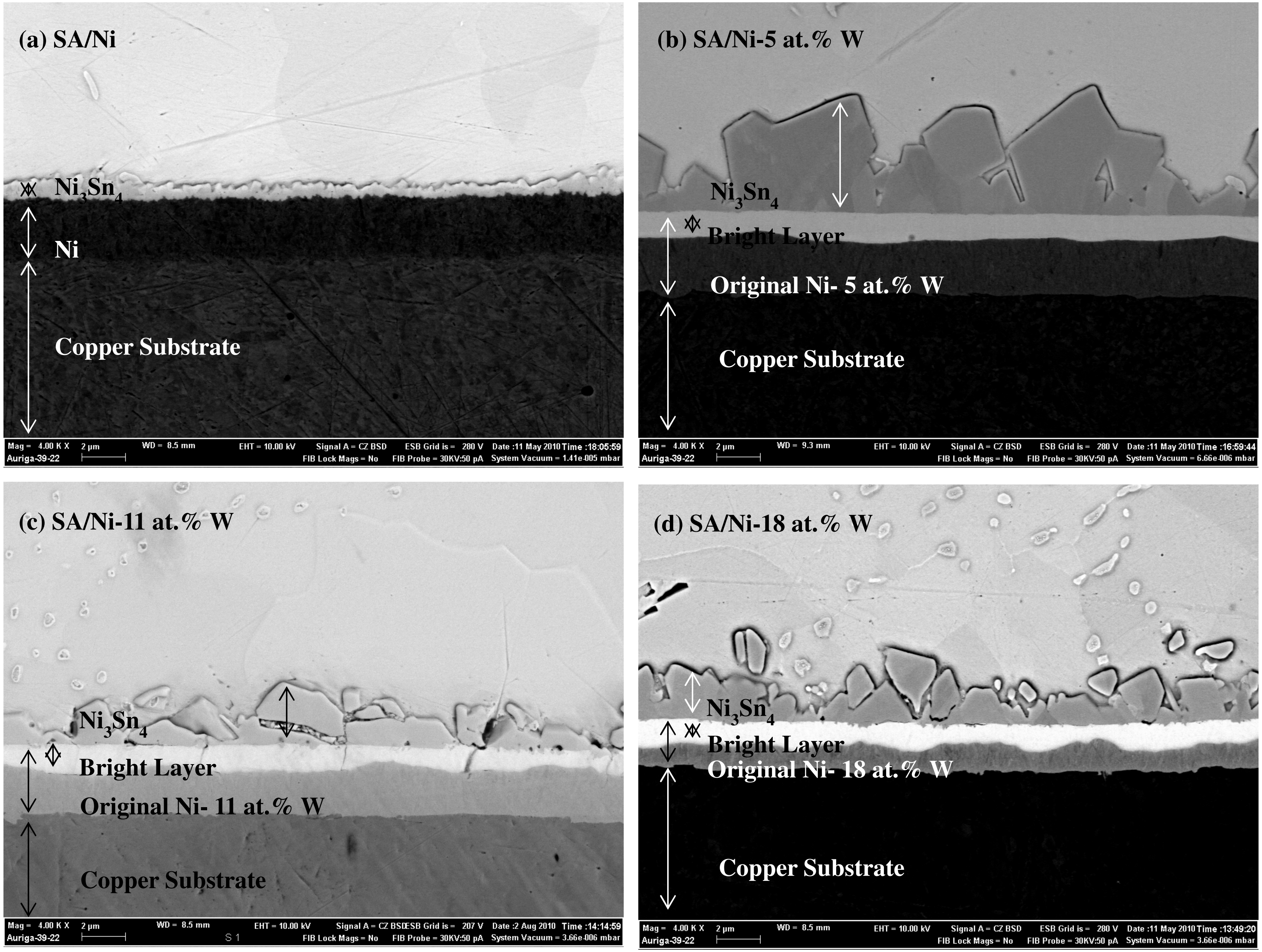
(a) SA/Ni
Ni3Sn4
Ni
Copper Substrate
(b) SA/Ni-5 at.% W
Ni3Sn4
Bright Layer
Original Ni- 5 at.% W
Copper Substrate
(c) SA/Ni-11 at.% W
Ni3Sn4
Bright Layer
Original Ni- 11 at.% W
Copper Substrate
(d) SA/Ni-18 at.% W
Ni3Sn4
Bright Layer
Original Ni- 18 at.% W
Copper Substrate
Mag = 4.00 K X
2 µm
Auriga-39-22
EHT = 10.00 kV
Signal A = CZ BSD

Figure 4.10

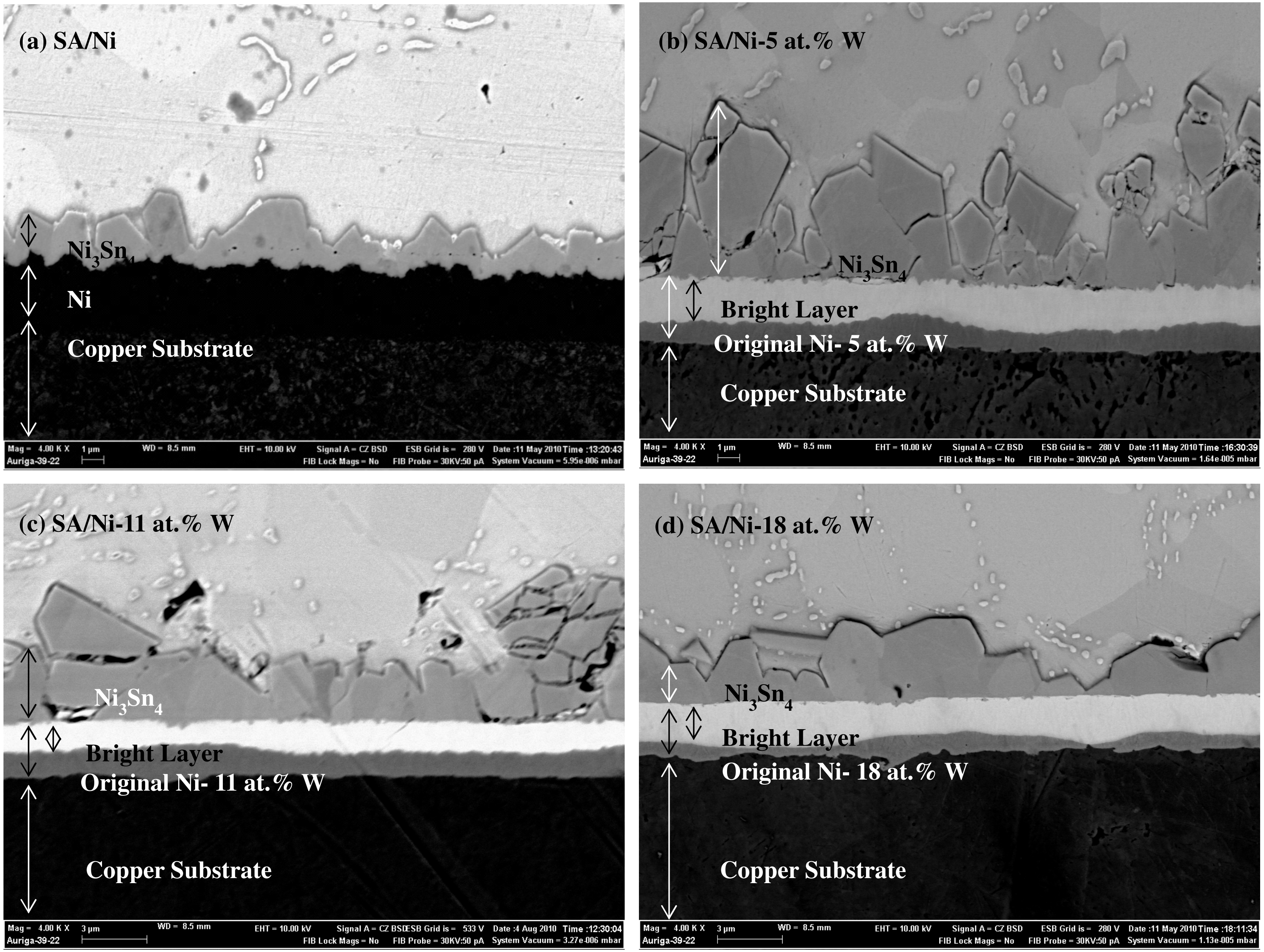
(a) SA/Ni
Ni_3Sn_4
Ni
Copper Substrate
Mag = 4.00 K X 1 μm WD = 8.5 mm EHT = 10.00 kV Signal A = CZ BSD ESB Grid is = 280 V Date :11 May 2010 Time :13:20:43
Auriga-39-22 FIB Lock Mags = No FIB Probe = 30KV:50 pA System Vacuum = 5.95e-006 mbar
(b) SA/Ni-5 at.% W
Ni_3Sn_4
Bright Layer
Original Ni- 5 at.% W
Copper Substrate
Mag = 4.00 K X 1 μm WD = 8.5 mm EHT = 10.00 kV Signal A = CZ BSD ESB Grid is = 280 V Date :11 May 2010 Time :16:30:39
Auriga-39-22 FIB Lock Mags = No FIB Probe = 30KV:50 pA System Vacuum = 1.64e-005 mbar
(c) SA/Ni-11 at.% W
Ni_3Sn_4
Bright Layer
Original Ni- 11 at.% W
Copper Substrate
Mag = 4.00 K X 3 μm WD = 8.5 mm EHT = 10.00 kV Signal A = CZ BSD ESB Grid is = 533 V Date :4 Aug 2010 Time :12:30:04
Auriga-39-22 FIB Lock Mags = No FIB Probe = 30KV:50 pA System Vacuum = 3.27e-006 mbar
(d) SA/Ni-18 at.% W
Ni_3Sn_4
Bright Layer
Original Ni- 18 at.% W
Copper Substrate
Mag = 4.00 K X 3 μm WD = 8.5 mm EHT = 10.00 kV Signal A = CZ BSD ESB Grid is = 280 V Date :11 May 2010 Time :18:11:34
Auriga-39-22 FIB Lock Mags = No FIB Probe = 30KV:50 pA System Vacuum = 1.13e-005 mbar

Figure 4.14

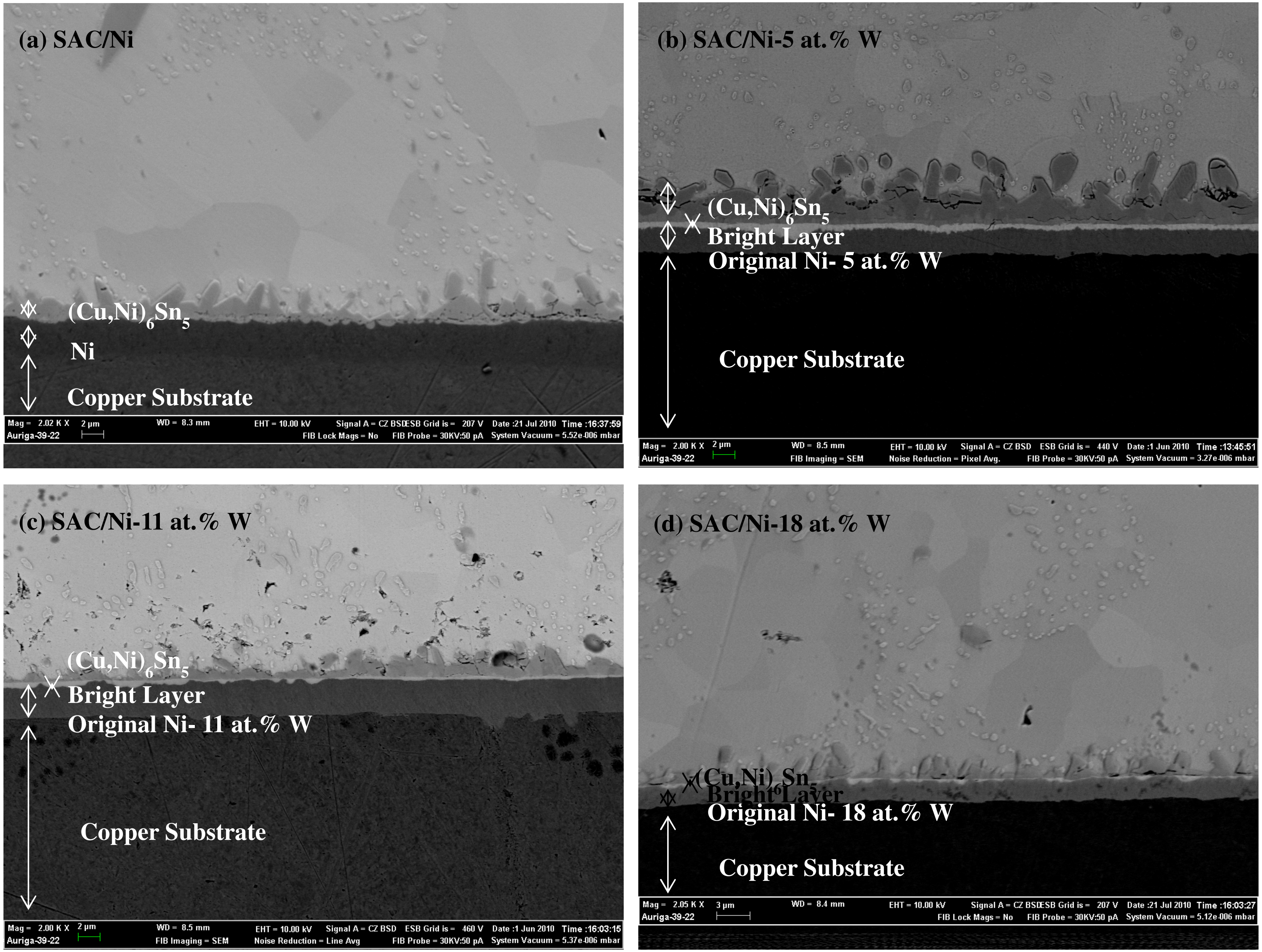
(a) SAC/Ni
(Cu,Ni)$_6$Sn$_5$
Ni
Copper Substrate
Mag = 2.02 K X
2 µm
WD = 8.3 mm
EHT = 10.00 kV
Signal A = CZ BSD
ESB Grid is = 207 V
Date :21 Jul 2010
Time :16:37:59
Auriga-39-22
FIB Lock Mags = No
FIB Probe = 30KV:50 pA
System Vacuum = 5.52e-006 mbar
(b) SAC/Ni-5 at.% W
(Cu,Ni)$_6$Sn$_5$
Bright Layer
Original Ni- 5 at.% W
Copper Substrate
Mag = 2.00 K X
2 µm
WD = 8.5 mm
EHT = 10.00 kV
Signal A = CZ BSD
ESB Grid is = 440 V
Date :1 Jun 2010
Time :13:45:51
Auriga-39-22
FIB Imaging = SEM
Noise Reduction = Pixel Avg.
FIB Probe = 30KV:50 pA
System Vacuum = 3.27e-006 mbar
(c) SAC/Ni-11 at.% W
(Cu,Ni)$_6$Sn$_5$
Bright Layer
Original Ni- 11 at.% W
Copper Substrate
Mag = 2.00 K X
2 µm
WD = 8.5 mm
EHT = 10.00 kV
Signal A = CZ BSD
ESB Grid is = 460 V
Date :1 Jun 2010
Time :16:03:15
Auriga-39-22
FIB Imaging = SEM
Noise Reduction = Line Avg
FIB Probe = 30KV:50 pA
System Vacuum = 5.37e-006 mbar
(d) SAC/Ni-18 at.% W
(Cu,Ni)$_6$Sn$_5$
Bright Layer
Original Ni- 18 at.% W
Copper Substrate
Mag = 2.05 K X
3 µm
WD = 8.4 mm
EHT = 10.00 kV
Signal A = CZ BSD
ESB Grid is = 207 V
Date :21 Jul 2010
Time :16:03:27
Auriga-39-22
FIB Lock Mags = No
FIB Probe = 30KV:50 pA
System Vacuum = 5.12e-006 mbar

Figure 4.15

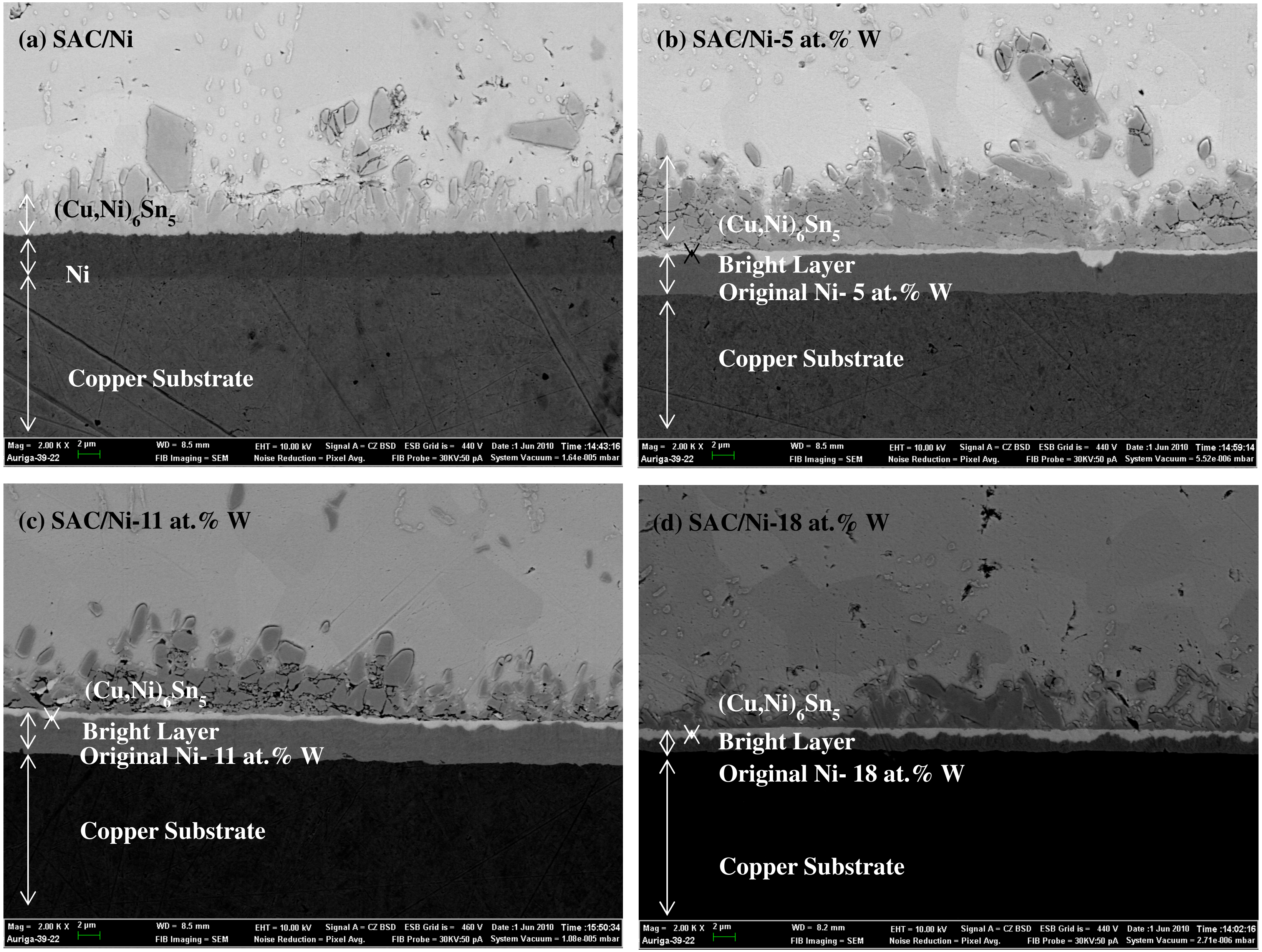
(a) SAC/Ni
(Cu,Ni)6Sn5
Ni
Copper Substrate
(b) SAC/Ni-5 at.% W
(Cu,Ni)6Sn5
Bright Layer
Original Ni- 5 at.% W
Copper Substrate
(c) SAC/Ni-11 at.% W
(Cu,Ni)6Sn5
Bright Layer
Original Ni- 11 at.% W
Copper Substrate
(d) SAC/Ni-18 at.% W
(Cu,Ni)6Sn5
Bright Layer
Original Ni- 18 at.% W
Copper Substrate
Mag = 2.00 K X
2 μm
Auriga-39-22
EHT = 10.00 kV
Signal A = CZ BSD
FIB Imaging = SEM
Noise Reduction = Pixel Avg.
FIB Probe = 30KV:50 pA
Date :1 Jun 2010